

A Thesis Submitted for the Degree of PhD at the University of Warwick

Permanent WRAP URL:

<http://wrap.warwick.ac.uk/171366>

Copyright and reuse:

This thesis is made available online and is protected by original copyright.

Please scroll down to view the document itself.

Please refer to the repository record for this item for information to help you to cite it.

Our policy information is available from the repository home page.

For more information, please contact the WRAP Team at: wrap@warwick.ac.uk



High Sensitivity Fiber-coupled Magnetometry Using
an Ensemble of Nitrogen-Vacancy Centers in
Diamond

by

Rajesh L. Patel

Thesis

Submitted to the University of Warwick

for the degree of

Doctor of Philosophy

Department of Physics

January 2022

Contents

List of Tables	v
List of Figures	vi
Acknowledgments	xiv
Declarations	xvi
Abstract	xvii
Abbreviations	xviii
Chapter 1 Introduction	1
1.1 Diamond	1
1.1.1 Diamond Structure	1
1.1.2 Diamond Uses	2
1.2 Thesis Structure	3
1.3 Co-Worker Contribution	4
Chapter 2 Magnetometry	6
2.1 Magnetometry in Diamond	6
2.2 Magnetic Field Sensitivity	8
2.3 Magnetometers	8
2.3.1 SQUID magnetometer	8
2.3.2 Hall magnetometer	9
2.3.3 Fluxgate magnetometer	10
2.3.4 SERF magnetometer	11
2.4 The Nitrogen Vacancy Center in Diamond	11
2.5 Spin Hamiltonian	16
2.5.1 Electronic Zeeman	17

2.5.2	Zero-field splitting	18
2.5.3	Nuclear Zeeman	19
2.5.4	Hyperfine Interaction	19
2.5.5	Nuclear Quadrupole Interaction	21
2.5.6	Nitrogen-Vacancy Ground State	22
2.6	Magnetometry Methods	22
2.6.1	Continuous Wave Magnetometry	23
2.6.2	Ramsey Magnetometry	27
2.6.3	Hahn Echo Magnetometry	30
Chapter 3 Diamond Synthesis and Characterization		31
3.1	Synthesis of Nitrogen-Vacancy Center Diamonds	31
3.1.1	High-Pressure High-Temperature	32
3.1.2	Chemical Vapor Deposition	35
3.1.3	Irradiation and Annealing	38
3.2	Diamond Characterization	39
3.2.1	Photon Absorption	40
3.2.2	Fourier-transform infrared absorption spectroscopy	42
3.2.3	Ultraviolet–visible absorption spectroscopy	43
3.2.4	Electron Paramagnetic Resonance spectroscopy	44
Chapter 4 Subnanotesla Magnetometry with a Fiber-Coupled Dia-		
mond Magnetometer		47
4.1	A Fiber-coupled Diamond Magnetometer	47
4.1.1	Zero-Crossing Slope	49
4.2	Diamond Material Properties	49
4.2.1	Electron Paramagnetic Resonance Measurements	50
4.2.2	Absorption Measurements	50
4.3	Magnetometer Design	51
4.3.1	Sensitivity Optimization	53
4.3.2	Microwave and Electronics	54
4.3.3	Microwave Delivery System	55
4.3.4	Microwave Antenna Choice	55
4.3.5	Optically Detected Magnetic Resonance Spectra	58
4.3.6	Zero-crossing Slope vs. Modulation frequency	60
4.3.7	Test Field Calibration	61
4.3.8	Sensor Head	62
4.3.9	Laser Noise	63

4.3.10	(111) Orientation vs. (100) Orientation	64
4.3.11	Shot-noise limit scaling as a function of PL	65
4.4	Future Goals	67
Chapter 5 Imaging Damage in Steel Using a Diamond Magnetometer		69
5.1	Introduction	69
5.1.1	Visual Inspection	70
5.1.2	Magnetic Flux Leakage	70
5.1.3	Ultrasonic Inspection	70
5.1.4	Eddy Current Testing	71
5.2	Magnetic Flux Distortion	71
5.2.1	Dynamic Range	72
5.3	Alternating Field Current Method	73
5.4	Experimental Details	73
5.5	Diamond Properties	75
5.6	ODMR Spectrum Under Different Conditions	76
5.7	Scan Data Profile	76
5.7.1	Magnetic Field Sensitivity	79
5.7.2	Inhomogeneous Field Sensitivity	82
5.7.3	Lift-off Vs. Height	82
5.8	Magnetic Mapping	83
5.8.1	COMSOL simulations	85
5.8.2	Damage Under Insulation	86
5.9	Alternating Current	88
5.10	Conclusion and Future Goals	91
Chapter 6 Development of a Magnetic Gradiometer Towards Per-		
forming Magnetocardiography		93
6.1	Gradiometer	94
6.1.1	Red-Red Subtraction	95
6.1.2	Microwave System	96
6.2	Diamond Material Properties	97
6.3	Signal Processing	98
6.3.1	Signal Averaging	98
6.3.2	Wavelet Denoising	99
6.3.3	Allan Variance	107
6.3.4	Power Saturation	107
6.4	Results of Red-Red subtraction	108

6.5 Future Work	110
Chapter 7 Conclusions	113

List of Tables

3.1	The classification of diamond according to the defect type and concentration.	40
4.1	The sensitivity values obtained from the wire vs loop antenna comparison study. The microwave power values are listed as dBm but this is the value prior to amplification; the microwave output is amplified by 43 dB and this is the microwave power delivered to the antenna. All specified sensitivity values are in units of $\text{nT}\sqrt{\text{Hz}}$ and are the mean of 160 FFTs, the errors quoted are the standard deviation of the 160 FFTs. The abbreviations LHS and RHS are left-hand side and right-hand side respectively. For the last row of the table the microwave power was set -20 dBm (value prior to amplification) while the laser power was reduced to 500 mW, this measurement was only taken for the loop antenna.	58
5.1	The concentration of defects in the diamond sample used for steel scanning are listed.	75
6.1	The concentration of defect in the diamond samples used in the gradiometer.	98
6.2	The root-mean square error (RMSE) of various standard deviations when applying random noise to a clean ECG signal and denoising it are shown. The decomposition level listed here is the ideal level that gives the best RMSE value.	104
6.3	The magnitude of the 50 Hz signal that is applied is listed along with the best decomposition level to achieve the lowest root-mean square error when comparing the denoised signal to the original ECG signal. The magnitude of 50 Hz is given as a value relative to the voltage. .	106

List of Figures

2.1	a) Energy level diagram of the negatively charged nitrogen vacancy (NV) center defect. The hyperfine interaction for ^{14}N is shown; here $\gamma = 28 \text{ GHz/T}$ is the gyromagnetic ratio of the NV center. The differing thicknesses of the relaxation from the $^3\text{E } m_s = 0$ and $m_s = \pm 1$ states to the $^3\text{A}_2 m_s = 0$ and $m_s = \pm 1$ states respectively illustrates the difference in fluorescence intensity between these two decay paths. b) The structure of the NV center in diamond. The bonds connecting to the vacancy are illustrated differently to highlight that there are electrons (dangling bonds) that contribute to the NV center and a total of six electrons are present.	12
2.2	Simulated optically detected magnetic resonance of an NV ensemble with a magnetic field of 3 mT strength unaligned to any particular NV center orientation. For this simulated spectrum the bias field projection angles are 29° , 132° , 109° , 83° for NV 4, NV 3, NV 2 and NV 1 respectively. A total of 24 resonances are observed when an ensemble of defects are excited due to the four NV center resonances and the hyperfine interaction. The chosen parameters used were to highlight the hyperfine interaction of the ^{14}N with the unpaired electron system. The corresponding NV center resonance pairs are labeled for clarity.	14

2.3	a) For the sake of simplicity a single resonance is considered i.e. the hyperfine interaction is neglected to illustrate the linewidth, $\Delta\nu$ and the contrast, C_{CW} . This was simulated using a Lorentzian profile with $C_{CW} = 1\%$ and $\Delta\nu = 0.5$ MHz and a magnetic field strength of 3 mT at an angle of 29° relative to the NV center causing a resonance to occur at f_{res} . b) The principle of magnetic field detection is demonstrated. In this instance a magnetic field shift of 3 μ T is applied to the NV center. If monitoring the resonance with a fixed applied frequency, i.e. f_{res} , the effect of a changing magnetic field induces a Zeeman-shift and thus the emitted fluorescence given by the NV center changes and thus the magnetic field can be detected.	24
2.4	The principles of lock-in amplification (LIA) using frequency modulation of the NV center ODMR resonance is described using a simulated resonance. a) The original carrier frequency, f_c is modulated with a reference frequency of frequency amplitude/depth, f_{dev} and a modulation frequency f_m . b) The demodulated output of the original ODMR resonance scaled by a factor of 1000 for clarify. This profile is the derivative of the original NV center ODMR resonance but has a vastly superior signal-to-noise ratio due to the rejection of noise at frequencies away from f_m	26
2.5	The Ramsey sequence is shown in the Bloch sphere with the corresponding pulse sequence for both the laser and the microwaves. a) The spin is initialized to the $ 0\rangle$ through a 532 nm laser pulse. b) a $\pi/2$ microwave pulse is applied to create a superposition between the $ 0\rangle$ and $ 1\rangle$ states. c) No lasers or microwaves act on the system and it is allowed to evolve freely with a free precession time, τ . As the system is freely evolving the $ 1\rangle$ states acquires a phase relative to the $ 0\rangle$ state when interacting with an external magnetic field. d) A $\pi/2$ microwave pulse is applied to project the population difference between the $ 0\rangle$ and $ 1\rangle$ states onto the $ 0\rangle$ and $ 1\rangle$ basis. e) Pulsed laser excitation is then performed to readout the spin state and thus determine the magnetic field.	28
2.6	The Hahn echo sequence is shown in the Bloch sphere and the corresponding pulse sequence for both the laser and the microwaves is shown. The processes a), b), e) and f) are unchanged from Ramsey sequence magnetometry. However, in this scheme a π -pulse is introduced during the free precession time, τ	30

3.1	The phase diagram of carbon, the regions of growth of CVD, HPHT (catalytic and non-catalytic) and shockwave synthesis regions. The Berman-Simon line, the diamond/graphite equilibrium line is shown. The CVD synthesis region has been enlarged for clarity.	32
3.2	A schematic of the HPHT belt press showing diamond growth. The temperature difference between the carbon source and diamond seed is ΔT , where T_1 is greater than T_2 . The true morphology of the diamond is neglected for simplicity.	34
3.3	Schematic of a chemical vapor deposition microwave reactor.	36
3.4	A simplified Bachmann diagram for CVD growth. Some compounds are listed to illustrate the principle of the diagram.	37
3.5	A modified Michelson-Morley set-up used for Fourier-transform infrared absorption spectroscopy measurements.	43
3.6	The components of the EPR spectrometer.	45
4.1	(a) The UV-Vis data which determined the neutral and negatively charged concentrations of NV center. (b) FTIR data which was used to determine concentrations of neutral and positively charged substitutional nitrogen defects.	51
4.2	A schematic of the fiber-coupled diamond magnetometer. The dimensions of the sensor head are shown but other components are not drawn to scale. The terms ND and LP are respectively the abbreviations for neutral density and long pass. The hyperfine excitation was provided by the function generator. The bias magnetic field was used for alignment of the NV center resonance to a particular crystallographic orientation.	52
4.3	For the following sensitivity measurements the bias field was aligned along (100), and the sensitivity taken for both NV center resonances; the left-hand side (LHS) resonance frequency is 2846.4 MHz while for the right-hand side (RHS) the resonance frequency was 2883.55 MHz. The mean sensitivity is the mean between the frequency range 10-200 Hz. (a) The loop LHS resonance, (b) the loop RHS resonance, (c) the wire LHS resonance and (d) the wire RHS resonance.	56

4.4	(a) An ODMR spectrum of the NVC as a function of varying microwave frequency. (b) The zero-crossing slope and the contrast-to-linewidth ratio as a function of applied microwave power after amplification and neglecting cable losses. All measurements were taken using a frequency modulation amplitude of 300 kHz and a modulation frequency of 3.0307 kHz.	59
4.5	The zero-crossing slope as a function of the modulation frequency.	60
4.6	Diamond magnetometry sensitivity spectrum: the mean sensitivity is $310 \text{ pT}/\sqrt{\text{Hz}}$ from 10-150 Hz. The noise floor is shown when no longer on a resonant frequency (magnetically insensitive) and with no applied laser or microwaves (electronic noise). The on resonance, off resonance and electronic noise are the mean of 160 1s FFT's. Inset is a figure that demonstrates the magnetometer responsivity for a given applied test field. This calibration was used to determine the sensitivity.	61
4.7	Temperature variation of the aluminum antenna as a function of time for 60 minutes.	63
4.8	A picture of the sensor head (black horizontal cylinder in the top right). On the left is a NdFeB bias magnet in a rotatable aluminum enclosure. A ruler is included to show the scale size.	64
4.9	(a) The zero crossing-slope (ZCS) is plotted as a function of the square root of the NV center photoluminescence (PL), F. (b), (c) and (d) are respectively the sensitivity, the photon-shot-noise limit and the sensitivity-to-shot-noise ratio all are plotted as a function of the square-root of the PL.	65
4.10	A power saturation curve plotting the applied laser power against the photodiode output from the balanced detector.	66

5.1	(a) A schematic of the experimental configuration, the neutral density (ND) filter, microwave (MW) and radio frequency (RF) sources, lock-in amplifier (LIA), and the two photodiodes (PDs) of the balanced detector are included. Magnet 1 is embedded into the aluminum (light grey rectangle) on which the microwave antenna is printed. (b) A schematic of the microwave antenna and the magnet configuration used to induce the Zeeman splitting (the blue and red colors are used to illustrate the differing magnetic poles). (c) and (d) are the 316 stainless steel plates (dimensions of 150 mm by 150 mm with a 6 mm thickness) used for these experiments: only a small area where the damage were introduced onto the plates are shown for clarity; the schematic dimensions are not to scale.	74
5.2	ODMR spectra under different conditions. (a) is taken with and without a 316 stainless steel sample. (c) are ODMR spectra with a lift-off from the stainless steel from a lift-off distance of 0 mm to 4 mm. (e) is for various positions along the length of the gradient-depth steel sample. (b), (d) and (f) correspond to the dashed regions in (a), (c) and (e) respectively, these are of the outermost right hand side NV center resonance.	77
5.3	(a) and (d) are the 2D scans for the gradient-depth and gradient-width samples. (b) and (e) are the percentage changes that come out from the LIA output voltage for the black lines which are parallel to the y -axis, these correspond to the profiles for (a) and (d) respectively. The profiles in (c) and (f) are the LIA voltage output percentage changes, these correspond to the six lines which are parallel to the x -axis in (a) and (d); four of the six lines are taken along the damage area (lines 2-5), two are taken along areas where there is no damage (lines 1 and 6).	78

5.4	(a) The ODMR spectrum from the lock-in amplifier (LIA) output. The hyperfine splitting cannot be resolved as the magnetic field is highly inhomogeneous. (b) The dependence of the sensitivity on the input microwave power (black square) and the modulation amplitude (red circle), the abbreviations MW and MA are microwave and modulation amplitude respectively. (c) The changes to the LIA output voltage while monitoring a fixed microwave frequency when the lift-off distance between the sensor head and a damage-free 316 stainless steel sample is changed is shown. These measurements were taken under two different sensitivity conditions. The lowest sensitivity achieved for the microwave power of 0.8 W and a modulation amplitude of 300 kHz was chosen for the black circle, while microwave power of 10 W and a modulation amplitude of 4.5 MHz was chosen for the higher sensitivity situation. The lift-off from the aluminum to the steel is zero for $\Delta\text{Height} = 0$ mm.	80
5.5	(a) ODMR spectrum using the Supermagnete W-01-N and Q-25-25-13-N magnets. (b) ODMR spectrum using only the Supermagnete Q-25-25-13-N. (c) Spectral density corresponding to the configurations in (a) and (b).	81
5.6	The 2D-scan results for the gradient-depth (sample 1) and gradient-width (sample 2) samples are shown in (a) and (d) respectively. The scan dimensions for (a) and (d) were 45 mm \times 20 mm. To quantify the damage, Lorentzian fits were applied to the cross sectional profile of (a) and (d). The amplitudes of the changes to the LIA voltage are shown in (b) and (e) respectively. The full width at half maximum (FWHM) of the cross section of both damage profiles imaged by the diamond magnetometer, (c) and (f), are shown for sample 1 and sample 2 respectively. COMSOL simulations were performed with the results shown in (b), (c), (e) and (f) for comparison.	84
5.7	The COMSOL simulation of the experimental set-up: for simplicity the air space and mesh network have been ignored. The sample shown here is the gradient-depth sample. The detector in this case refers to the diamond.	86
5.8	The simulation results of the 2D scans of the two 316 steel samples. The results of the scan for sample 1 (the gradient-depth) and sample 2 (the gradient-width) are (a) and (b) respectively.	87

5.9	Two dimensional scans of the gradient-depth (sample 1) and gradient-width (sample 2) samples when covered with nonmagnetic materials. The scan dimensions were 45×20 mm. The dashed lines in the maps encapsulate the structural damage, (a) and (c) are from sample 1 while (b) and (d) are from sample 2. For (a) and (b) the stainless steel is covered with 1.5 mm of brass while for (c) and (d) the steel is covered with 2 mm of fiberglass.	87
5.10	The placement of the two coils around a steel sample is shown. . . .	88
5.11	(a) The 2D scan results for (a) blank sample, (b) the gradient-depth and (c) the gradient-width samples. For all scans the step size was 0.1 mm in the x-axis while it was 1 mm in the y-axis. For (a) and (c) the scan parameters were 17.1 mm in the x-axis while it was 26 mm in the y-axis while for (b) the scan parameters were 15.1 mm in the x-axis while it was 32 mm in the y-axis. The damage slots are illustrated by the dashed boxes.	89
5.12	The full width at half-maximum (FWHM) of the (a) gradient-depth and (b) gradient-width samples.	90
6.1	The experimental setup of the gradiometer when taking an approach of subtracting a magnetically sensitive nitrogen vacancy photoluminescence signal from another.	95
6.2	(a) A 10.4 second ECG trace is shown; although data was taken for 100 s for clarity only a portion is shown and used for averaging. There are a total of 17 cardiac traces present with the blue square marker indicating the peak of the QRS complex. The orange cross is the negative time (-220 ms from the QRS complex peak) while the green cross is the positive time (350 ms from the QRS complex peak). The sample rate was 5000 samples/s. (b) The ECG trace shown here is the average of 17 cardiac traces.	99
6.3	A 3 level decomposition of data. This process is the method of taking a discrete wavelet transform.	100
6.4	The data shown here is a synthetic ECG signal and one with random noise added with a mean of zero and a standard deviation of 45. . . .	102
6.5	The approximation and detail coefficients of the noisy data are shown, due to the use of db2 as the choice of filter there are 8 levels of decomposition.	103
6.6	The original ECG signal is shown along with the denoised signal. . .	104

6.7	The data shown here is the original ECG signal and data to where 50 Hz noise has been artificially added to the signal; the magnitude of the 50 Hz is 400.	105
6.8	The approximation and detail coefficients of the data that has had 50 Hz added to the signal is shown. In this case the coif2 wavelet was used to decompose the noisy signal leading to a total of six decomposition levels.	105
6.9	The original ECG signal with no noise is shown along with the denoised signal after the 50 Hz noise was removed (the magnitude of 50 Hz noise was 400).	107
6.10	A power saturation curve of the gradiometer.	108
6.11	Data relating to the gradiometer sensitivity. (a) Voltage trace of the two sensor heads and the result of subtracting the two from one another. (b) The spectral density and sensitivity of the SiC sensor head. (c) The spectral density and sensitivity of the aluminum sensor head. (d) The spectral density and sensitivity when employing gradiometer subtraction, both sensor heads are magnetically sensitive. The bias magnetic was unaligned to any particular orientation for the results obtained.	109
6.12	The Allan deviation for the gradiometer when either the SiC or aluminum sensor head is magnetically sensitive whilst the other is not and the other case is when subtraction mode is used whilst both magnetometer sensor heads are magnetically sensitive.	111

Acknowledgments

As is the nature of research in the modern age the work carried out in this thesis is the result of the hard work and support of many individuals who have put in a great deal of time and effort. I would firstly like to acknowledge Dr Gavin W. Morley for funding and supervision. The advice and direction provided in our discussions have been very valuable and it would not have been possible to obtain the results in this thesis without him. I am thankful to have worked with many capable and talented individuals. I am grateful to Dr. Ben G. Breeze, Dr. Ben L. Green and Dr. Matthew W. Dale for beginning the magnetometer project and particularly thankful to Dr. Breeze for his aid in the characterization of the many diamond samples I have used. I am particularly thankful for the many interesting discussions I have had with Dr. Breeze, Dr. Green and Prof. Mark E. Newton; they have been of immense help. I am particularly grateful to Dr Guy A. Stimpson and Dr. Angelo C. Frangeskou for considerably furthering the magnetometry project and for teaching me a great deal of the experimental aspects related to optics and instrumentation control (and for their patience in doing so!). I am grateful also to Dr. Leiqing (Ray) Q. Zhou who for a great deal of this project has worked alongside me and has gone above and beyond in terms of the work he has put in. A great deal many hours far beyond what was needed was placed into this work by him and I do not believe a great deal of it could have been achieved without his aid.

I am grateful for the several friendships, in addition to the friendship of the colleges mentioned previously that I have made through the undertaking of this PhD. I am thankful for the many conversations I have had with Gloria Zhao, Yashni Lekhai, Luke Mills, Enrik Nako and Luke L. Johnson. I would also like to extend

thanks to Luke for the many diamond samples he has cleaned for me and the many discussions we have had about many topics beyond science. I am thankful for the many friendships I have made whilst at the University of Warwick and particularly indebted to my housemates for the close friendships they have provided during my time at the University of Warwick. Most of all I am eternally indebted to my family who have provided a great deal of support and in particular my parents and siblings who have always supported me and offered me aid in all aspects of my life. I dedicate this thesis and the culmination of all its work to my family.

Declarations

I, Rajesh L. Patel, confirm that the work submitted in this thesis is my own expect where stated otherwise. The work was carried out entirely at the University of Warwick under the supervision of Dr. Gavin Morley between the period of October 2018 to December 2021. The research included in this thesis has not been submitted either in part or wholly to any other academic institution. Some of the research included has been published.

- R. L. Patel, L. Q. Zhou, A. C. Frangeskou, G. A. Stimpson, B. G. Breeze, A. Nikitin, M. W. Dale, E. C. Nichols, W. Thornley, B. L. Green, M. E. Newton, A. M. Edmonds, M. L. Markham, D. J. Twitchen and G. W. Morley, *Sub-nanotesla magnetometry with a fibre-coupled diamond sensor*, Physical Review Applied 14, 044058, (2020).
- L. Q. Zhou, R. L. Patel, A. C. Frangeskou, A. Nikitin, B. L. Green, B. G. Breeze, S. Onoda, J. Isoya and G. W. Morley, *Imaging damage in steel using a diamond magnetometer*, Physical Review Applied, 15, 024015 (2021).

Abstract

The utilization of solid-state defects for application in quantum and quantum-assisted technologies has grown in recent years with focus on the nitrogen-vacancy center in diamond for the detection of magnetic fields with superior spatial resolution than any other magnetic field sensor technology. In this work a fiber-coupled magnetometer that is completely portable and can reach sub-nanotesla sensitivities was developed and characterized.

For industrial application, a method was developed to detect damage in steel; this method was to measure the magnetic flux distortion of magnetic flux inserted into the ferromagnetic material under inspection allowing damage profiles to be mapped out. The other method which was investigated was the alternating field current method which was used to investigate damage in conductive materials. In both cases the fiber-coupled magnetometer was able to image damage in steel and differentiate the depth and width of the damage profiles.

For medical applications, work was undertaken towards the development of a gradiometer to be able to perform unshielded magnetocardiography (MCG) measurements. Signal processing techniques were also investigated to be able to help improve the signal-to-noise of any MCG signals. For convenience an electrocardiography signal, whose morphology is similar to an MCG signal was used.

Abbreviations

Definitions

B Magnetic field

CW Continuous wave

CWT Continuous wavelet transform

CVD Chemical vapor deposition

D Zero field splitting

DWT Discrete wavelet transform

ECG Electrocardiography

EPR Electron paramagnetic resonance

FFT Fast Fourier-Transform

FTIR Fourier transform infrared

g_e Free electron g-value

g_n Nuclear g-value

HPHT High pressure high temperature

I Nuclear spin

ISC Intersystem crossing

K_H Hall coefficient

L Orbital angular momentum

LIA Lock-in amplifier

MCG Magnetocardiography

MEG Magnetoencephalography

NDT Non-destructive testing

NV Nitrogen vacancy

ODMR Optically detected magnetic resonance

ppm parts per million

RF Radio frequency

RMSE Root mean-square error

S Electronic spin

SNR Signal-to-noise

SQUID Superconducting quantum interference device

T_2 Homogeneous spin dephasing time

T_2^* Inhomogeneous spin dephasing time

UV-Vis Ultraviolet-visible

V_H Hall voltage

ZCS Zero-crossing slope

ZPL Zero-phonon line

α Absorption coefficient

θ Angle between Hall component and magnetic field

h Planck's constant

\hbar Reduced Planck's constant

μ Magnetic moment

μ_0 Magnetic permeability of free space

μ_B Bohr magneton

μ_n Nuclear magneton

τ Free precession time

λ_{SO} Russel-Saunders spin-orbit coupling term

Chapter 1

Introduction

Historically, diamond has been greatly prized as a display of wealth and power for the rich and powerful: many monarchies have used diamonds in this way. The name diamond is derived from the ancient Greek word “adámas” meaning unalterable, unconquerable, invincible. Although there are in fact several methods that can destroy diamond, the name is apt for a material that is among the hardest known to man.

First thought to have been mined in India over 3000 years ago [1], the gem became of great value due to its incredible properties. This was furthered with the development of cutting and polishing techniques which allowed for the fabrication of ornaments that could be worn. The scarcity of diamond coupled with its properties have historically led to it being used exclusively as ornaments. More recently however, over the last century or so, the uses of diamond have grown far beyond being used as mere trinkets and have found use in a range of applications with extensive scientific research devoted to exploitation of its properties and a range of industrial applications found. Currently, scientific investigation is being undertaken to develop the application of diamond for quantum technologies.

1.1 Diamond

1.1.1 Diamond Structure

Diamond is an allotrope of carbon with a $1s_2 2s_2 2p_2$ ground state orbital configuration. Some of the other common allotropes of carbon are graphite and graphene. In diamond the carbon orbital are sp^3 hybridised and thus a single carbon will form bonds with four nearest neighbours leading to a tetrahedral structure. The structure of diamond is best thought of as two interlaced face-centered-cubic cell arrays with

one lattice displaced relative to the other by a quarter of the unit cell constant, of length $a_0 = 0.357$ nm. The distance between the carbon-carbon atoms is 0.154 nm. The unit cell is comprised of 8 carbon atoms with two points of basis at (0,0,0) and $(\frac{1}{4}, \frac{1}{4}, \frac{1}{4})$. The tetrahedral arrangement and the resulting covalent bonding makes diamond an incredibly strong material. This also gives the diamond lattice configuration the highest atomic density among any known material with a density of $1.76 \times 10^{23} \text{ cm}^{-3}$, the atomic density is determined by $\frac{8}{a_0^3}$. Using this density as a basis the addition of defects is measured on a scale relative to this density and for most defects in the diamond lattice their concentrations are given in the parts per million (ppm), a concentration of 1 ppm translates to a concentration of $1.76 \times 10^{17} \text{ cm}^{-3}$.

1.1.2 Diamond Uses

The remarkable properties of diamond have spurred a range of technologies using its extreme hardness [2], chemical inertness [3; 4; 5; 6; 7; 8], high thermal conductivity [9; 10; 11], low coefficient of thermal expansion [11; 12; 13], large optical window, strong covalent bonding [14] and exceptionally high breakdown voltages [15]. The strong covalent bonding makes the material among the strongest known to man. While the high breakdown voltage is useful in computing in preventing an avalanche of electrons from occurring when a high enough voltage is applied, diamond could be used for certain transistor types. Due to these properties diamond-based technologies offer or can offer superior performances when compared to non-diamond based devices. For example these applications have been extend to electrochemical analysis in extreme environments [16], radiation-hard detectors for the Large Hadron Collider [17], high quality optical windows [18; 19] and thermal heat spreaders [20].

More recently the demonstration of optically detected magnetic resonance (ODMR) of single nitrogen-vacancy center in diamond [21] has led to intense interest in the utilization of color centers in diamond as the foundation of quantum and quantum-assisted technologies which could form the basis of quantum cryptography, quantum networks and quantum computing. Due to the wide band gap of diamond it is possible for many differing color centers to be optically active within the diamond lattice making diamond an attractive material for the development of stable quantum devices.

Numerous color centers, numbering in the hundreds, have been identified in diamond, however only a handful of these have displayed stable photon emission and thus can be useful in applications relating to quantum assisted sensing or forming the foundation of quantum networks [22]. If the photon emission isn't stable it may be difficult to utilize with regards to manipulating and reading the

spin state. Of these color centers the most prominent are the nitrogen-vacancy center [23] and the negatively charged silicon-vacancy (SiV^-) [24; 25], investigations into the neutral group IV vacancy complexes are currently ongoing. Recently, investigations into using neutral group IV vacancy complexes such as the neutral silicon-vacancy (SiV^0) [26; 27; 28; 29] have suggested that these defects could be useful for quantum-related applications. Investigations are ongoing to identify newer color centers that could have properties that are superior to those which are currently known of. Though many groups are investigating the usage of the nitrogen-vacancy center in diamond as the foundation for quantum computers its application in the sensing of magnetic fields has been fairly well established. Indeed a key application of the nitrogen-vacancy center defect in diamond is in the detection of magnetic fields with unrivaled spatial resolution. The focus of this work is the utilization of an ensemble of nitrogen-vacancy center defects in diamond for use as a magnetic field sensor with a focus on the development of a system that has a high sensitivity, a mobile sensor head, is portable and can be used for a variety of applications with a particular focus on industrial and medical application.

1.2 Thesis Structure

Chapter 2 introduces the usage of defects in diamond for magnetometry with a review of the physics of the NV center including involving a discussion of the spin Hamiltonian. The most common magnetometry methods that are possible with diamond are described.

Chapter 3 reviews the synthesis and growth of NV centers in diamond and some of the common techniques used to characterize the properties of defects in diamond.

Chapter 4 involves the development and characterization of the fiber-coupled diamond magnetometer that has been built and the steps taken to optimize the sensitivity. At the time of publication the device developed had the highest sensitivity of any fiber-coupled diamond magnetometer. The system was completely portable with the ability to move it to a different location, such as the UK Quantum Technology showcase, whilst still being able to maintain subnanotesla sensitivity.

Chapter 5 discusses the development of techniques that can characterize damage in materials for the purpose of non-destructive testing (NDT). One of the two methods used were the magnetic flux distortion. This method made use of a dual arrangement of magnets with one of the two magnets being a small 1 mm cube magnet that was both near the diamond and near to the magnetic material under inspec-

tion. This method allowed for the quantification of differences in depth and width of damage in stainless steel; this can be extended to any ferromagnetic material. The other method was to use an alternating field current method which applies to any conductive material. This uses low frequency currents to induce eddy currents within a conductive material which will in turn induce magnetic fields that can be detected by a diamond magnetometer.

Chapter 6 discusses the development of a magnetic gradiometer for the purpose of performing unshielded measurements to detect cardiac magnetic fields. There are also discussions about various signal processing methods that would aid in achieving this objective.

Chapter 7 is a conclusion summarizing the key achievements of each chapter and suggestions for future experiments.

1.3 Co-Worker Contribution

The work presented in this thesis was the result of collaboration between multiple individuals with all work performed under the supervision of Dr. Morley.

For the fiber-coupled diamond magnetometer developed and characterized in chapter 4. The magnetometer was initially developed by Dr. Breeze, Dr. Dale and Dr. Green. Dr. Stimpson and Dr. Frangeskou then took over with the fiber-coupled concept primarily being developed by Dr. Frangeskou and Dr. Morley. Further development was then undertaken by me and Dr. Zhou. Data relating to diamond characterization was undertaken by Dr. Breeze. Will Thornley and Eleanor Nichols worked on the magnetometer as summer students. The diamond sample was synthesized by Dr. Edmond, Dr. Markham and Dr. Twitchen. All data obtained from the magnetometer was taken by either me and/or Dr. Zhou with all data analysis being performed by me. The microwave antenna and heat cooling solutions for the laser were developed by Dr. Nikitin. All authors contributed to the writing of the paper. Prof. Newton provided useful insights during discussions. The project was supervised by Dr. Morley.

The magnetic flux distortion concept from chapter 5 was developed primarily by me and Dr. Zhou. COMSOL simulations were performed Dr. Zhou. All data relating to magnetic flux distortion and all associated analysis was performed by me and/or Dr. Zhou. The alternating current experiments were conceived by me and Dr. Zhou, with all experimental data collection and the associated analysis being performed by me. Characterization of the diamond and all data analysis relating to this was performed by Dr. Breeze and me. The diamond was irradiated by Prof. Isoya

and S. Onoda. The diamond was annealed by Dr. Green. The magnetometer designed was conceived by Dr. Frangeskou while the microwave antenna was designed by Dr. Nikitin. All authors contributed to the writing of the paper.

The gradiometer mentioned in chapter 6 was developed by primarily by me with some input from Dr. Zhou. All data and data analysis was undertaken by me along with all signal processing data. The SiC antennae were designed by Dr. Nikitin. Dr. Morley supervised the project.

Chapter 2

Magnetometry

2.1 Magnetometry in Diamond

The detection of magnetic fields has always been relevant in a diverse range of fields ranging from geological to biomedical applications [30; 31; 32; 33; 34], providing valuable information which helps to understand the structure of unknown materials and can be applied in a wide range of devices ranging from spacecraft to medical devices. Apart from the compass needle, the most popular devices for measuring magnetic fields have been superconducting quantum interference devices (SQUIDs), Hall-effect magnetometers, flux-gates, magnetoresistive magnetometers and optical magnetometers based on atomic vapor cells [30; 33; 35; 36]. The sensitivities of some of these magnetometers have reached levels on the order of $\sim \text{fT}/\sqrt{\text{Hz}}$ or better [32; 34; 37; 38; 39]. At such sensitivities it is possible to detect the magnetic fields produced from the heart and brain for the detection of abnormalities. These techniques are called magnetocardiography (MCG) and magnetoencephalography (MEG) respectively.

Over the last decade interest in a magnetometer based on solid state defects has grown considerably due to the significant advantages such defects offer, and in particular, interest in the nitrogen vacancy (NV) center defect in diamond. The defect exists in three possible charge states: a positive charge state (NV^+) [40; 41; 42], a neutral charge state (NV^0), a spin-1/2 defect [43; 44; 45] or in the negative charge state (NV^-), a spin-1 defect [40; 41; 42; 43; 44; 45]. Currently only the NV^- center is capable of performing magnetometry [46] and it is the most studied defect in diamond for quantum applications [23; 47; 48; 49; 50; 51]. This is due to the presence of optically detected magnetic resonance [21], high photostability [52] and long spin coherence times [53], which can be extended through isotopic purification

which depletes the ^{13}C spin environment [54] or through dynamic decoupling techniques or both [55; 56; 57; 58; 59]. These properties of the NV^- center occur even under ambient conditions at room temperature. In addition, the NV^- center is also able to offer a high dynamic range (the dynamic range shall be defined as the range over which the magnetometer can detect magnetic fields) for magnetometry measurements [60]. The NV^- center charge state is more likely to exist in diamonds when a nearby spin donor is present in the lattice, which in most instances is single substitutional nitrogen, which donates an electron [23; 43]. Operation of the NV^- center has also been extended to temperatures above 600 K and coupled with the inherent properties of diamond can allow diamond based magnetometers to be used under a range of conditions where other magnetometers cannot operate [61]. The NV^- center charge state shall from hereon, unless stated otherwise, be referred to as the NV center.

Though ODMR of the NV center had been demonstrated in 1997 by Gruber *et al.* [21] research into using the NV center was initially carried out only by a few groups. Further interest in the NV center had developed when a proposal of utilizing a single spin for application in magnetometry was put forth by Chernobrod and Berman in 2005 [62] for use in atomic force microscopy. In addition later proposals suggested that the NV center was a suitable candidate for room temperature high resolution magnetometry [63; 64]. Research into NV centers increased considerably after the experimental verification of the NV center as a room-temperature single spin magnetometer by two independent groups, based at Harvard University and Stuttgart University which demonstrated nanoscale resolution magnetometry [65; 66]. It was also demonstrated that an ensemble of defects could allow the detection of weaker magnetic fields, this was due to statistical averaging over a larger number of spins, but this degraded the spatial resolution [67; 68].

Since the demonstration of high resolution magnetometry, the NV center has seen application in a variety of fields, using both single centers or an ensemble of defects. This includes the sensing of magnetic fields with nanoscale resolution for biological application [6; 69; 70; 71], and due to their low toxicity, nanodiamonds have been used as bio-compatible fluorescent markers and for targeted drug delivery [3; 4; 5; 6; 7; 8; 72; 73; 74; 75]. Other applications include high resolution magnetic mapping of geological samples [76], high frequency resolution nuclear magnetic resonance spectroscopy [77; 78; 79; 80], the detection of action potentials from a single neuron [81] and eddy current scanning of conductive materials [82]. Further to magnetometry applications the NV center has been used for quantum science such as the first loophole-free violation of a Bell inequality [83]. Additionally, there have

been proposals and progress [50] toward NV quantum computing. These promising applications have led to a considerable number of patents being filed and several companies exist attempting to commercialize technologies based on the NV center.

2.2 Magnetic Field Sensitivity

The sensitivity of a magnetometer is defined as the minimum magnetic field that can be detected with a SNR-ratio of 1, i.e. the minimum detectable magnetic field is the same as the noise floor. The noise floor can be improved by averaging for a longer time, so it is stated now that the sensitivity is defined as per square-root Hertz for a measurement bandwidth measured in Hertz. This is due to the fact that noise floor of a magnetometer, i.e. the minimum detectable field can be improved by averaging for a longer period of time. This normalizes all sensitivity measurements to the minimum magnetic field that can be measured in a single second allowing for a fair comparison between different magnetometer technologies.

2.3 Magnetometers

The focus of this thesis is the utilization of the NV center in diamond as a magnetometer but as mentioned in section 2.1 there are other magnetometers that are employed. This section will briefly describe some of the other magnetometers that are used.

2.3.1 SQUID magnetometer

The SQUID magnetometer's operating principle is based upon the Josephson effect and the fact that flux can be quantized in a superconducting ring [30]. The Josephson effect describes the tunneling of electrons between two superconducting materials which are placed in close proximity to one another that are separated by a thin layer of insulating material. To reach a state of superconductivity, where there is no electrical resistance to the flow of electrons, the materials are cooled typically using liquid helium [34]. A SQUID consists of a superconducting loop which is interrupted by one or two Josephson junctions in parallel. The SQUID sensor is extremely sensitive to any magnetic flux that penetrates the area of the loop: a voltage is induced across the device when this happens [84].

An input current is passed through the loop and in the absence of any magnetic field the current is equally split and passes through the two Josephson junctions. Upon the application of an external magnetic field to the loop a current is generated,

this current generates a magnetic field which cancels out the external applied magnetic flux, this process results in the creation of a Josephson phase which is exactly proportional to the applied external magnetic flux. The induced current will be in the same direction as one of the two loop branches whilst it will be in the opposite direction for the other: the current in one branch is increased by half of the current that is generated by the external magnetic field whilst it is reduced in the other half. If the induced current exceeds a particular threshold (the critical current of the Josephson junction) a voltage is produced across the junction.

If the applied external flux exceeds half the value of the magnetic flux quantum, 2.07×10^{-15} Wb, the flux of the SQUID will increase by the value of the magnetic flux quantum. This will cause the direction of the current to reverse to oppose the change that caused it. From this every integer increase of the flux by an amount equal to the magnetic flux quantum will cause the repeated and periodic reversals of the current's direction. Over the course of a single cycle of magnetic flux quantum, at half the value of the quantum flux the voltage change will be maximum and if the magnetic flux applied is equal to the magnetic flux quantum the voltage will return to zero [85].

To ensure a non-hysteretic current-voltage a shunt resistor is placed in parallel with each Josephson junction. The SQUID device is biased with a constant current that is larger than the sum of the two Josephson critical currents. Due to this the output voltage is correlated to the magnetic flux and has a period that is equal to the value of the flux quantum. From this it is possible to determine the magnetic field.

Historically, SQUID magnetometers have been used to study the magnetic properties of various materials and due to reaching sensitivities on the order $\text{fT}/\sqrt{\text{Hz}}$, they have been used for MCG and MEG. These magnetometers have good temporal resolution and can detect frequencies in the kHz range [86; 87]. However, despite these achievements the need to cryogenically cool these magnetometers makes them far too expensive for widescale deployment.

2.3.2 Hall magnetometer

The Hall sensor makes use of the Hall effect to sense magnetic fields. A current is applied to a thin metal strip. When a magnetic field is perpendicular to the direction of the current the charge carriers are deflected due to the induced Lorentz force; this produces a potential difference between the two sides of the strip which is proportional to the strength of the magnetic field. The Hall voltage, V_H can be expressed by the following equation

$$V_H = K_H J B \cos(\alpha), \quad (2.1)$$

where the K_H is the Hall coefficient, J is the current, B is the magnetic induction intensity and α is the normal of the angle between the Hall component and the induced magnetic field. The signal produced is typically very weak and thus has to be amplified. The manufacturing process of producing Hall probe magnetometers is very well established and thus Hall probe sensors are generally employed in various fields which require the detection of the magnetic field. There are limitations in their applications as they cannot be employed in cases where the magnetic field is high. Hall probe sensors do also suffer from thermal drift over time [88]. It is possible for Hall probe magnetometers to reach sensitivity on the order of $\text{nT}/\sqrt{\text{Hz}}$.

2.3.3 Fluxgate magnetometer

The fluxgate magnetometer is typically made out of a ring core which is itself made of a highly magnetically permeable alloy. Two wires are wrapped around the ring core, these coil windings are referred to as the the drive winding and the sense winding. In the case of the driving winding an alternating current is passed through the coil, this current periodically causes the ferromagnetic material that forms the core to become saturated. The ferromagnetic core is then modulated by a local magnetic field and this is sensed by the sense winding wire. The ring core is designed in such a way that it detects magnetic fields that are along the direction of an external magnetic field. As the current is passed through the drive winding, half of the core will generate a field that is in the same direction as that of the external magnetic field while the other half of the core will generate a field that is in the opposite direction to this [30; 89].

When there is no external magnetic field the two fields of each half core will exactly cancel and thus there is no change in the flux measured by the sense winding. When there is an external field, the half core whose magnetic field is in the opposite direction of said external magnetic field will change its period of saturation, the half core will come out of saturation sooner when compared to the other core. As there is now a difference in the magnetic fields due to this period change, the fields no longer cancel one another and there will be a magnetic flux that is detected by the sense winding coil. This in turn induces a voltage that is proportional to the magnetic field.

In general fluxgates can reach a sensitivity of the order nanotesla and are small and compact and inexpensive and so fluxgates are used in various fields. Some

of the more recent fluxgates have also reached sensitivities on the order of a picotesla. Fluxgates have been used for satellites and probes in space and have been used to detect variations in the magnetic field of the Earth [89].

2.3.4 SERF magnetometer

The spin-exchange relaxation-free (SERF) magnetometer is a type of magnetometer that was developed at Princeton University around two decades ago. The basic construct is to use a glass cell that is filled with an alkali atom in vapor form at a high density. A narrow linewidth laser is used to optically pump the atoms so that all atoms are spin polarized to near unity. Any magnetic field that is perpendicular to the pump beam will rotate the spins by an angle that is proportional to the strength of the magnetic field. This polarization state is typically measured by using a linearly polarized laser that is transmitted perpendicular to the laser beam used for optical pumping. The polarization of this probe beam is rotated due to circular birefringence in which the component of spin polarization along the direction of the probe beam causes the refractive index to be different for the clockwise and anti-clockwise circularly polarized light [39; 37]. A polarimeter is used to detect the amount of polarization which is proportional to the magnetic signal. These magnetometers have reached high sensitivities on the order $\text{fT}/\sqrt{\text{Hz}}$ and thus are comparable to the sensitivities that state-of-the-art SQUID magnetometers can reach. Spin-off companies based on atomic magnetometers have been established, for example the Cerca Magnetics company which employs the QuSpin magnetometer, these sensors are sensitive enough for MEG [90].

2.4 The Nitrogen Vacancy Center in Diamond

The NV center is a point defect in diamond that is formed from a substitutional nitrogen atom adjacent to a lattice vacancy, see figure 2.1b); this gives rise to localized electronic states whose energy levels are well within the diamond bandgap. The nitrogen atom has five valence electrons with three forming a covalent bond with carbon atoms, two electrons therefore are not bonded and are a lone pair. The vacancy has three electrons however two exist in a quasi-covalent bond. In this state the NV center has a single unpaired electron and is a spin-1/2 system. If the system can capture an electron from an external source then it will become a spin-1 system with two unpaired electrons. The wide bandgap of diamond is technically convenient for optical access to color centers in diamond. The diamond lattice structure arrangement leads to a local trigonal symmetry and constrains the NV center to a $\langle 111 \rangle$ crystal-

lographic orientation: the NV center exists in four $[111]$ orientations [46; 91], which are $[111]$, $[1\bar{1}\bar{1}]$, $[\bar{1}1\bar{1}]$ and $[\bar{1}\bar{1}1]$, for clarity it is stated that there technically eight directions as the ± 1 directions for each orientation are equal. Unless preferential orientation is favored [92; 93; 94; 95; 96; 97; 98; 99] during growth the four orientations will have an equal abundance in an as-grown diamond sample. Due to this the utilization of an ensemble of defects allows vector magnetometry to be performed. As the NV center orientations are fixed within the diamond each NV center will feel a different magnetic field projection allowing vector reconstruction of the Cartesian components of an external magnetic field [64; 68; 100; 101; 102; 103; 104]. This offers an advantage over other magnetometers which are typically scalar in nature; for these magnetometers to obtain vector information three magnetometers are often used in a Cartesian configuration while for a diamond magnetometer only a single diamond is required to accomplish vector magnetometry, this has been demonstrated experimentally [103]. For clarity, further details on how magnetometry is performed using the NV center is mentioned explicitly in section 2.6.1. The sensing of a magnetic field involves applying a bias field to induce Zeeman-splitting of the NV center

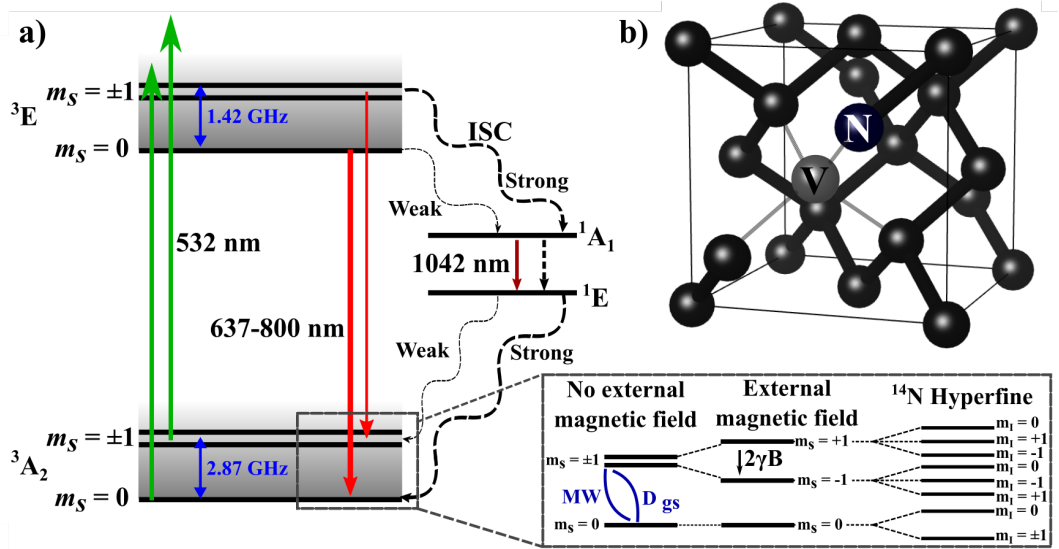


Figure 2.1: a) Energy level diagram of the negatively charged nitrogen vacancy (NV) center defect. The hyperfine interaction for ${}^{14}\text{N}$ is shown; here $\gamma = 28 \text{ GHz/T}$ is the gyromagnetic ratio of the NV center. The differing thicknesses of the relaxation from the 3E $m_s = 0$ and $m_s = \pm 1$ states to the 3A_2 $m_s = 0$ and $m_s = \pm 1$ states respectively illustrates the difference in fluorescence intensity between these two decay paths. b) The structure of the NV center in diamond. The bonds connecting to the vacancy are illustrated differently to highlight that there are electrons (dangling bonds) that contribute to the NV center and a total of six electrons are present.

resonances. A fixed microwave frequency is applied to the steepest part of the resonance profile (which is typically either Gaussian or Lorentzian in shape). At these resonances there is a drop in NV center fluorescence emission. If monitoring a fixed position on the resonance when there is a change in the magnetic field the resonant frequency will shift due to the Zeeman effect and this causes a change in the NV center fluorescence. Through this the magnetic field that induces the shift can be determined.

A key property of the NV center is the ground state triplet, which shall be discussed in more detail in section 2.5. The ability to initialize and read out the spin state entirely through optical means is the principle used in optically detected magnetic resonance. The application of resonant microwaves yielding spin dependent fluorescence allows spin-state readout; it is this property that we refer to as ODMR. This is possible due to the intersystem crossing (ISC) that the NV center possesses [105]. Excitation is typically achieved by non-resonant illumination using a 532 nm laser. Other wavelengths can be employed as the NV center has a broad absorption spectrum however 532 nm is used as it is close to the peak of the optimum wavelength of absorption [106] and 532 nm is a common laser wavelength for most commercial lasers.

In relation to the NV center energy level structure, (see figure 2.1a), in the absence of any applied magnetic field the NV center ODMR resonances are degenerate and are determined by the zero-field splitting of the ground state triplet which is ~ 2.87 GHz at room temperature [23; 21; 107].

Upon application of a magnetic field of sufficient strength Zeeman splitting of the $m_s = \pm 1$ energy levels is introduced and depending upon the projection of the external magnetic field upon the NV center symmetry axis, B_{NV} , a perturbation of the energy level from its zero field value is introduced. This shift is given by

$$h\Delta f = 2g_{NV}\mu_B B_{NV}, \quad (2.2)$$

where h is Planck's constant, Δf is the frequency separation between the ground $m_s = \pm 1$ states, $g_{NV} \sim 2.0028$ is the NV centre Landé g-factor [23] and μ_B is the Bohr magneton. Furthermore, a hyperfine interaction exists between the electron spin $S = 1$ and the ^{14}N atom of the NV center, which possesses a nuclear spin of $I = 1$. Three resonances are produced which are each split by a frequency of ~ 2.158 MHz [23; 81]. It should be noted that there are two isotopes of nitrogen ^{14}N and ^{15}N , which respectively possesses a nuclear spin of $I = 1$ and $I = 1/2$. The presence of ^{15}N will therefore lead to two resonances, however, the significant abundance of ^{14}N over the other isotope means the contribution of

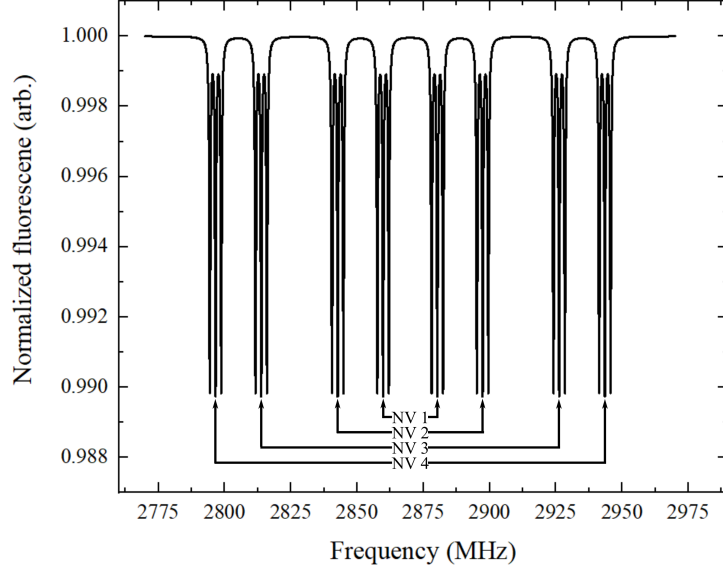


Figure 2.2: Simulated optically detected magnetic resonance of an NV ensemble with a magnetic field of 3 mT strength unaligned to any particular NV center orientation. For this simulated spectrum the bias field projection angles are 29° , 132° , 109° , 83° for NV 4, NV 3, NV 2 and NV 1 respectively. A total of 24 resonances are observed when an ensemble of defects are excited due to the four NV center resonances and the hyperfine interaction. The chosen parameters used were to highlight the hyperfine interaction of the ^{14}N with the unpaired electron system. The corresponding NV center resonance pairs are labeled for clarity.

^{15}N to the ODMR resonance signal is negligible unless the sample is isotopically enriched to favor ^{15}N [77; 108; 109]. Details regarding the spin properties of the NV center shall be discussed more extensively in section 2.5. An example ODMR spectrum of an ensemble of NV center defects is shown in figure 2.2. As was mentioned magnetometry is performed when monitoring a fixed microwave frequency. For this reason vector information can only be extracted if multiple NV center resonances are monitored, which requires multiple microwave frequency sources. In a typical magnetometry set-up only a single microwave frequency source is used to monitor a single resonance and thus if the bias magnetic field is unaligned as is the case in figure 2.2 then these resonances will not contribute to the magnetometry signal i.e. only a quarter of the NV centers will be used for sensing.

Transitions between the $^3\text{A}_2$ ground and ^3E excited state triplets are spin conserving and thus upon excitation with a 532 nm laser the spin state is conserved. It is noted that the naming convention for the energy states arise from group theory. Under no applied laser and under ambient conditions the spin population follows a

Boltzmann distribution. Excitation from the ground state 3A_2 $m_s = 0$ state will excite to the excited 3E $m_s = 0$ state and excitation from the ground $m_s = \pm 1$ state will lead to excitation to the excited $m_s = \pm 1$ state. As the transition rate through the intersystem crossing (ISC) is low from the 3E $m_s = 0$ state, upon excitation to this state from the 3A_2 $m_s = 0$ state, the system will decay back to the 3A_2 $m_s = 0$ state with characteristic emission of red fluorescence with a zero-phonon line (ZPL) of 637 nm. Photon absorption or emission by the NV center is governed by the Franck-Condon principle which states that when a molecule undergoes an electronic transition there is no significant change to the nuclear configuration of the system. The Franck-Condon principle itself arises from the Born-Oppenheimer approximation which allows the electronic and nuclear wavefunctions to be separated due to the significantly larger mass of a nucleus when compared to an electron and hence electronic transitions occur on much faster time scales and the nucleus will thereafter realign itself to the new electronic configuration and undergo a vibration [110]. The nuclear energy state will be shifted from its equilibrium state and a series of vibronic transitions will take place to take the nuclei back to its equilibrium state. Under this framework any optical transition between the NV center excited and ground state triplets will involve phonon-coupled higher vibrational levels which results in a large phonon sideband with photon emission extending out to 800 nm; emission into the NV center ZPL at 5 K is only $\sim 4\%$ and even less at room temperature. The phonon sideband originates from the interaction between the electronic and vibrational degrees of freedom. At lower temperatures the thermal energy is lower and thus the number of phonons which can be excited are reduced. When in the 3E $m_s = \pm 1$ state the probability of traveling through the ISC is significantly increased, $\sim 50\%$, and thus the system will either decay back to the 3E $m_s = \pm 1$ with the same fluorescence emission as the transition between the 3A_2 and 3E $m_s = 0$ states or the system will undergo non-radiative transitions, with competing radiation (1042 nm), which can be used for magnetometry [105; 111; 112; 113; 114; 115; 116], and non-radiative emission between the 1A_1 and 1E states. The system is then likely to initialize to the 3A_2 $m_s = 0$ state due to the higher transition probability, hence under continuous optical illumination the system will eventually spin polarize preferentially, typically $\sim 80\%$ into the $m_s = 0$ state has been demonstrated for an ensemble of NV center defects [117]. The reported degree of spin polarization in the literature for a single NV center has varied, with the differences arising due to the spin readout method employed, with values reported between $\sim 70\text{--}92\%$ [107; 118; 119]. Work is ongoing to improve this value to unity with different methods currently under exploration. It is typical that after a few cycles of the NV center system being pumped by a laser, the

NV center system is in the $m_s = 0$ ground state. Though transitions through optical means between the $m_s = 0$ and $m_s = \pm 1$ states are not used, application of resonant microwaves allows spin flipping and in this way the NV center spin system can be initialized and read out due to a decrease in the fluorescence when in the $m_s = \pm 1$ states [23; 107]. It is for this reason that if a single microwave source is used and in a scenario where the magnetic bias field is unaligned to any NV orientation only a quarter of the NV centers contribute to magnetometry; four microwave sources each targeting a different NV center resonance frequency would be needed. No population difference is induced for the NV center resonances at frequencies different to that of the applied microwaves.

For a single NV center and considering the decay lifetimes of the excited $m_s = 0$ and $m_s = \pm 1$ states which are respectively 12.7 ns and 7.8 ns the theoretical photon emission difference is $\sim 35\%$ [120]. However, under standard measurement conditions the fluorescence difference between spin states never exceeds 30% and thus a maximum spin contrast of 30% is obtained between the $m_s = 0$ and $m_s = \pm 1$ states.

2.5 Spin Hamiltonian

To truly understand the properties of the NV center, an unpaired electron system, is it necessary to consider the spin Hamiltonian, which governs all electronic and nuclear interactions. This will provide insight into several aspects of the NV center that were not discussed, or only briefly mentioned, in previous sections. Historically, this treatment of the spin system has been applied to interactions in electron paramagnetic resonance (EPR) measurements whose techniques and methods form the basis for most of the protocols used in ODMR. Indeed historically many of the defects discovered in diamond such as the NV center were first identified using EPR in conjunction with other characterization techniques. Details about the Hamiltonian and its application to EPR for defects is discussed in; all details regarding this section are found in the following references [121; 122; 123]. The generalized form of the spin Hamiltonian is as follows

$$\mathcal{H} = \underbrace{\mu_B \underline{\mathbf{B}}^T \cdot \underline{\mathbf{g}} \cdot \hat{\mathbf{S}}}_{\text{electron Zeeman}} + \underbrace{\hat{\mathbf{S}}^T \cdot \underline{\mathbf{D}} \cdot \hat{\mathbf{S}}}_{\text{zero-field}} + \sum_i^n \left\{ \underbrace{-\mu_N g_{N_i} \underline{\mathbf{B}}^T \cdot \hat{\mathbf{I}}_i}_{\text{nuclear Zeeman}} + \underbrace{\hat{\mathbf{S}}^T \cdot \underline{\mathbf{A}}_i \cdot \hat{\mathbf{I}}_i}_{\text{hyperfine}} + \underbrace{\hat{\mathbf{I}}_i^T \cdot \underline{\mathbf{P}}_i \cdot \hat{\mathbf{I}}_i}_{\text{quadrupole}} \right\}, \quad (2.3)$$

where $\underline{\mathbf{B}}^T = (\mathbf{B}_x, \mathbf{B}_y, \mathbf{B}_z)$ are the components of an external magnetic field

(the superscript T refers to the transpose); $\hat{\underline{\mathbf{S}}}^T$ and $\hat{\underline{\mathbf{I}}}^T$ are the electron and nuclear spin operators, whose components are $\hat{\underline{\mathbf{S}}}^T = (\mathbf{S}_x, \mathbf{S}_y, \mathbf{S}_z)$, the dimensionless electronic spin-1 operators, the relevant spin matrices are

$$S_x = \frac{\hbar}{\sqrt{2}} \begin{pmatrix} 0 & 1 & 0 \\ 1 & 0 & 1 \\ 0 & 1 & 0 \end{pmatrix}, S_y = \frac{\hbar}{\sqrt{2}i} \begin{pmatrix} 0 & 1 & 0 \\ -1 & 0 & 1 \\ 0 & -1 & 0 \end{pmatrix}, S_z = \frac{\hbar}{\sqrt{2}} \begin{pmatrix} 1 & 0 & 0 \\ 0 & 0 & 0 \\ 0 & 0 & -1 \end{pmatrix}.$$

The dimensionless nuclear spin operator is $\hat{\underline{\mathbf{I}}}^T = (\mathbf{I}_x, \mathbf{I}_y, \mathbf{I}_z)$; $\underline{\underline{\mathbf{A}}}_i$ is the hyperfine coupling tensor; μ_N is the nuclear magneton and g_N is the g-factor of the nucleus under consideration, which is summed over all nuclei i . There are terms beyond the five mentioned in equation 2.3 but these higher order terms can be neglected for the purpose of understanding the properties of the NV center. A brief explanation of each term in the Hamiltonian shall be given in the following sections and then the application to the NV center in diamond shall be discussed. All treatment shall be performed in a Cartesian basis with the z -axis co-aligned to the symmetry of the defect in question i.e. for the NV center this is along the axis that connects the nitrogen atom to the vacancy.

2.5.1 Electronic Zeeman

The electronic Zeeman term describes electron spins under the influence of an external magnetic field, with the energy of the system being given by $E = -\underline{\underline{\boldsymbol{\mu}}} \cdot \underline{\underline{\mathbf{B}}}$. A magnetic moment $\underline{\underline{\boldsymbol{\mu}}}$ is described by

$$\underline{\underline{\boldsymbol{\mu}}} = -\mu_B(\hat{\underline{\mathbf{L}}} + g_e\hat{\underline{\mathbf{S}}}), \quad (2.4)$$

where $\hat{\underline{\mathbf{L}}}$ is the component that relates to the orbital angular momentum while $\hat{\underline{\mathbf{S}}}$ relates to the intrinsic angular momentum (spin) and g_e is the electron g-factor. Furthermore, spin-orbit coupling will also play a role in providing an interaction that can be described by λ_{SO} , which is the strength of spin-orbit coupling; this term is also known as the Russel-Saunders spin-orbit coupling term. The Hamiltonian thus becomes

$$\mathcal{H}_S = \mu_B \underline{\underline{\mathbf{B}}} \cdot (\hat{\underline{\mathbf{L}}} + g_e\hat{\underline{\mathbf{S}}}) + \lambda_{SO} \hat{\underline{\mathbf{L}}} \cdot \hat{\underline{\mathbf{S}}}, \quad (2.5)$$

from this the spin Hamiltonian is then typically rewritten as

$$\mathcal{H}_S = \mu_B \underline{\mathbf{B}}^T \cdot \underline{\underline{\mathbf{g}}} \cdot \hat{\mathbf{S}}, \quad (2.6)$$

where $\underline{\underline{\mathbf{g}}}$ accounts for any perturbations to g_e due to either the orbital angular momentum or the spin-orbit coupling, $\underline{\underline{\mathbf{g}}}$ is then expressed as

$$\underline{\underline{\mathbf{g}}} = g_e \underline{\mathbf{I}}_3 + 2\lambda_{SO} \underline{\underline{\mathbf{A}}}, \quad (2.7)$$

where $\underline{\mathbf{I}}_3$ is the 3-by-3 identity matrix while $\underline{\underline{\mathbf{A}}}$ is the spin-orbit coupling matrix.

2.5.2 Zero-field splitting

The zero-field term describes electron-electron interactions, which even in the absence of an external magnetic field lifts the degeneracy of the spin system, and is thus only applied to systems which have two or more unpaired electrons i.e. $S > 1/2$. The zero-field Hamiltonian component is due to the electron spin-spin dipole interaction and for spins $\underline{\mathbf{S}}_1$ and $\underline{\mathbf{S}}_2$ is given by

$$\mathcal{H}_{SSD} = -\left(\frac{\mu_0}{4\pi}\right) g_1 g_2 \mu_B^2 \left[\frac{3(\underline{\mathbf{S}}_1 \cdot \underline{\mathbf{r}})(\underline{\mathbf{S}}_2 \cdot \underline{\mathbf{r}})}{r^5} - \frac{\underline{\mathbf{S}}_1 \cdot \underline{\mathbf{S}}_2}{r^3} \right], \quad (2.8)$$

where g_1 and g_2 are the g-factors for $\underline{\mathbf{S}}_1$ and $\underline{\mathbf{S}}_2$ respectively (it is generally assumed that $g_1 = g_2 = g$ as the spins are in the same environment), $\underline{\mathbf{r}} = \underline{\mathbf{r}}_2 - \underline{\mathbf{r}}_1$ is the unit vector in the direction of the line that joins the two spins, $r = |\underline{\mathbf{r}}|$, the distance between the two electron spins. As the spatial and spin terms can be separated from one another the zero-field Hamiltonian can be rewritten as

$$\mathcal{H}_{ZFS} = \underline{\mathbf{S}}^T \cdot \underline{\underline{\mathbf{D}}} \cdot \hat{\mathbf{S}}, \quad (2.9)$$

where $\underline{\underline{\mathbf{D}}}$ is the zero-field splitting tensor. By convention $\underline{\underline{\mathbf{D}}}$ is chosen to be traceless i.e. $\text{tr}(\underline{\underline{\mathbf{D}}}) = 0$, this term can be diagonalized and thus this component is typically expressed in terms of two parameters $D = 3D_z/2$ and $E = (D_y - D_x)/2$, which are the axial and rhombicity (transverse) components of the dipole-dipole interaction respectively. Using D, E and the fact that $S(S+1) = S_x^2 + S_y^2 + S_z^2$, the zero field Hamiltonian can then be expressed as

$$\mathcal{H}_{\mathcal{ZFS}} = D[S_z^2 - \frac{1}{3}S(S+1)] + E(S_x^2 - S_y^2), \quad (2.10a)$$

$$D = (\frac{\mu_0}{4\pi})(\frac{3}{4})g^2\mu_B^2\langle\frac{r^2 - 3z^2}{r^5}\rangle, \quad (2.10b)$$

$$E = (\frac{\mu_0}{4\pi})(\frac{3}{4})g^2\mu_B^2\langle\frac{y^2 - x^2}{r^5}\rangle, \quad (2.10c)$$

where $\langle \dots \rangle$ are expectation values which can be interpreted as the mean value obtained from a large number of measurements. It can be seen from equation 2.10 that the zero field value of a spin-1 system is highly dependent on the distance between the two spins and hence the local environment. This dependence merits further discussion and the implications for magnetic field sensing shall be expanded upon when discussing the Hamiltonian of the NV center ground state.

2.5.3 Nuclear Zeeman

Analogously to the electron spin, in a magnetic field a nuclear spin will experience an interaction, with the relevant terms in this instance being g_N and μ_N

$$\mathcal{H}_{\mathcal{NZ}} = \sum_i^n -\mu_N g_{N_i} \mathbf{B}^T \cdot \hat{\mathbf{I}}_i, \quad (2.11)$$

by virtue of the larger mass of a nucleus over that of an electron, this interaction is significantly smaller, approximately by a factor of 1000, than the electron Zeeman term. Furthermore, the allowed selection rules for EPR transitions are $|\Delta m_s| = \pm 1$ and $|\Delta m_I| = 0$ and thus for the most part this interaction can be neglected. This nuclear Zeeman term of the Hamiltonian has relevance in “forbidden” transitions which involve a double spin-flip. The electron and nuclear spins simultaneously flip with the selection rules $|\Delta m_s| = \pm 1$ and $|\Delta m_I| = \pm 1$. All four possibilities can occur.

2.5.4 Hyperfine Interaction

The hyperfine interaction, which was touched on briefly in section 2.4, is the effect of the interaction between a nuclear spin and a nearby electron spin and is given by

$$\mathcal{H}_{\mathcal{HI}} = \sum_i^n \hat{\mathbf{S}}^T \cdot \underline{\underline{\mathbf{A}}}_i \cdot \hat{\mathbf{I}}_i. \quad (2.12)$$

This component of the Hamiltonian can be treated in two cases which are

the isotropic and anisotropic interaction

$$\mathbf{A} = A_0 \mathbf{I}_3 + \mathbf{T}; \quad (2.13)$$

the terms A_0 and \mathbf{T} relate to the isotropic and anisotropic cases. The isotropic interaction arises if there is a finite electron spin density at the nucleus; this requires that s-orbitals contribute to the molecular orbital. Under this case the Hamiltonian simplifies to

$$\mathcal{H}_{ISO} = A_0 \hat{\mathbf{S}}^T \cdot \hat{\mathbf{I}}, \quad (2.14)$$

where the isotropic hyperfine coupling constant, A_0 , is given by

$$A_0 = \frac{2}{3} \frac{\mu_0}{h} g_e g_N \mu_B \mu_N |\phi(0)|^2, \quad (2.15)$$

where μ_0 is the permeability of free space and $|\phi(0)|^2$ is the electron wavefunction density at the nucleus.

The anisotropic term arises from dipole-dipole interactions between the magnetic moments of the electron and nucleus and the Hamiltonian for this is given by

$$\mathcal{H}_{DD} = \frac{1}{4\pi} \frac{\mu_0}{h} g_e g_N \mu_B \mu_N \left[\frac{\mathbf{S} \cdot \mathbf{I}}{r^3} - \frac{3(\mathbf{S} \cdot \mathbf{r})(\mathbf{I} \cdot \mathbf{r})}{r^5} \right]. \quad (2.16)$$

This can be expanded and integrated over the electron spatial distribution yielding the anisotropic term

$$\mathcal{H}_{ANI} = \hat{\mathbf{S}}^T \cdot \underline{\underline{\mathbf{T}}} \cdot \hat{\mathbf{I}}, \quad (2.17)$$

where \mathbf{T} is a second rank tensor. Taking the isotropic and anisotropic components for an axially symmetric hyperfine interaction it is possible to reduce \mathbf{T} to a diagonal tensor and from this express \mathbf{A} in terms of components that are parallel and perpendicular to the principle axis

$$\mathbf{A} = \begin{pmatrix} A_{\perp} & 0 & 0 \\ 0 & A_{\perp} & 0 \\ 0 & 0 & A_{\parallel} \end{pmatrix},$$

where A_{\parallel} and A_{\perp} are the axial and transverse hyperfine constant where $A_0 = \frac{1}{3}(A_{\parallel} + 2A_{\perp})$ and $T = \frac{1}{3}(A_{\parallel} - A_{\perp})$.

2.5.5 Nuclear Quadrupole Interaction

The nuclear quadrupole term relates to the interactions between the electric field gradient (generated by the nearby electrons and nuclei) and any non-spherical charge distribution of the nucleus. This interaction is only relevant for nuclei with $I > 1/2$ as only these have a quadrupole moment, a non-spherical charge distribution. The Hamiltonian in this instance is

$$\mathcal{H}_{\mathcal{NQ}} = \sum_i^n \hat{\mathbf{I}}_i^T \cdot \underline{\underline{\mathbf{P}}}_i \cdot \hat{\mathbf{I}}_i, \quad (2.18)$$

where $\underline{\underline{\mathbf{P}}}$ is the nuclear quadrupole tensor; this is typically made traceless such that $\text{tr}(\underline{\underline{\mathbf{P}}}) = 0$ and thus like the zero field splitting Hamiltonian this allows the nuclear quadrupole Hamiltonian to be rewritten as

$$\mathcal{H}_{\mathcal{NQ}} = P_{\parallel} \left(I_z^2 - \frac{1}{3}I(I+1) + \frac{1}{3}\eta P_{\parallel}(I_x^2 - I_y^2) \right), \quad (2.19)$$

where $P_{\parallel} = 3P_z/2$ and $\eta = (P_x - P_y)/P_z$. The asymmetry parameter, η is constrained such that $0 \leq \eta \leq 1$, a value of $\eta = 0$ describes perfect axial symmetry while any non-zero value represents a deformation from this about the principle axis; a value of $\eta = 1$ is the case of complete rhombicity [124; 125]. The pre-factor P_{\parallel} is given by

$$P_{\parallel} = \frac{3eQ}{4I(2I-1)} \frac{\partial^2 V}{\partial z^2}, \quad (2.20)$$

where Q is the quadrupole moment which encapsulates the deviation from a spherical charge distribution. The larger the magnitude of Q the greater the distortion from sphericity ($Q = 0$ is a perfect spherical distribution). $Q > 0$ indicates a prolate charge distribution while $Q < 0$ is representative of an oblate charge distribution. V is the electrostatic potential at the nucleus and $\frac{\partial^2 V}{\partial z^2}$ is the electric field gradient [124; 125]. For completeness it is stated that the prefactor can alternatively be expressed as

$$P_{\parallel} = \frac{3e^2 q Q}{4I(2I-1)}, \quad (2.21)$$

with the equivalence being $eq = \frac{\partial^2 V}{\partial z^2}$; the terms e and q are the elementary charge, 1.6×10^{-19} C and the nuclear electric quadrupole moment respectively. This equivalence allows the quadrupolar coupling constant to be defined, $\frac{e^2 q Q}{\hbar}$ (whose units are typically given in MHz). This is useful as it is a measure of the strength of the electric field gradient for nuclei with the same I .

2.5.6 Nitrogen-Vacancy Ground State

Combining all of the Hamiltonian terms described in previous sections, and considering the trigonal C_{3v} symmetry of the NV center (axial symmetry) the Hamiltonian is [23; 91]

$$\begin{aligned} \mathcal{H}_{GS} = & DS_Z^2 + E(S_x^2 + S_y^2) + g_e\mu_B\mathbf{B} \cdot \mathbf{S} + PI_z^2 - g_I\mu_N\mathbf{B} \cdot \mathbf{S} \\ & + A_{\parallel}S_ZI_Z + A_{\perp}(S_xI_x + S_yI_y). \end{aligned} \quad (2.22)$$

The parameter E is zero for the NV center due to the trigonal symmetry however the presence of strain changes the local symmetry and can give E a non-zero value¹ which will lead to a mixing of the $m_s = \pm 1$ states, creating new eigenstates with different energies. This component can be neglected through the application of a bias magnetic field large enough that $B_{NV} \gg \frac{\hbar E}{g\mu_B}$. Even in particularly high strain diamond samples E only reaches a few MHz (the condition $D \gg E$ is always satisfied). Under typical conditions, application of a magnetic field of strength 1 mT is more than sufficient to make the effects of strain negligible. The ^{14}N quadrupolar splitting parameter is $P = -5$ MHz and has been experimentally determined [23]. For the ^{14}N nucleus of the NV center the values are $A_{\parallel} = -2.158$ MHz and $A_{\perp} = -2.7$ MHz. For the ^{15}N nucleus the values are $A_{\parallel} = -3.01$ MHz and $A_{\perp} = -3.01$ MHz [126].

It was established in section 2.5.2 that the term D for a spin system arises from spin-spin coupling interactions and $D \sim 2.87$ GHz. Changes in the the local temperature environment of the NV center will induce a lattice expansion leading to a change in the value of D . The changes to the zero-field splitting due to temperature are approximately -74 kHz/K. Due to this temperature dependence the NV center has been employed as a highly sensitive thermometer [127; 128]. This temperature dependence represents a problem for NV center magnetometry as a 1 mK temperature fluctuation causes a 74 Hz change in D and this appears as a magnetic field change of 3 nT [129; 130]. Solutions to overcome this have been developed and shall be discussed in section 2.6.

2.6 Magnetometry Methods

Magnetometers based on using the property of spin are fundamentally limited by the noise associated with quantum spin projection and for a magnetometer employing

¹It is possible to treat strain as equivalent to the application of electric field to the NV center and thus the contribution of E is more correctly a sum of the electric and strain components.

an ensemble of defects N , the best sensitivity, η_{sp} that can result is given by the spin-projection-noise limit,

$$\eta_{sp} \sim \frac{\hbar}{g_{NV}\mu_B} \frac{1}{\Delta m_s} \frac{1}{\sqrt{N\tau}}, \quad (2.23)$$

where \hbar is the reduced Planck's constant, Δm_s is the spin multiplicity and τ is free precession time per measurement. The smaller the value of the sensitivity the better for detecting weaker magnetic fields i.e. the sensitivity is the smallest change in magnetic field that a magnetometer can detect. For the purposes of high sensitivity magnetometry an ensemble of defects is required [46; 81]. As a magnetometer can detect weaker fields through by measuring for a longer period of time it is common to give the sensitivity of a magnetometer in units of T/ $\sqrt{\text{Hz}}$, this normalizes the sensitivity to the minimum magnetic field that can be detected in one second. There are several different magnetometry methods that have been demonstrated. Though atomic vapor cells are governed by this and have to date achieved higher sensitivities (that are comparable to SQUIDS), the NV center is projected to be able to offer similar sensitivities with a higher spatial resolution due to the higher density of spins achievable for solid-state defects compared to that which is possible for defects that exist in gaseous form [64; 67].

2.6.1 Continuous Wave Magnetometry

The continuous wave sensing scheme relies on simultaneous application of microwaves and laser illumination to an NV center (or an ensemble of NV centers). Zeeman-splitting is induced by application of an external magnetic field which creates resonances at specific frequencies. As the positions of an NV center resonance are characterized by its Zeeman-splitting, any perturbations caused by a magnetic field will shift the ODMR resonances leading to a change in the fluorescence emitted by the defects (see figure 2.3b). Hence, monitoring a resonance at fixed frequency and measuring any changes to its fluorescence profile allows the magnitude of an external magnetic field to be identified. The frequency shift due to the magnetic field can be detected provided it is within the bandwidth range of the sensor. In this scheme, and indeed all schemes that use the emitted fluorescence, the sensitivity is fundamentally limited by the photon-shot-noise limit which for a scheme where the readout occurs during the free precession time is given by

$$\eta_{CW} = P_f \frac{h}{g_{NV}\mu_B} \frac{\Delta\nu}{C_{CW}\sqrt{F}}, \quad (2.24)$$

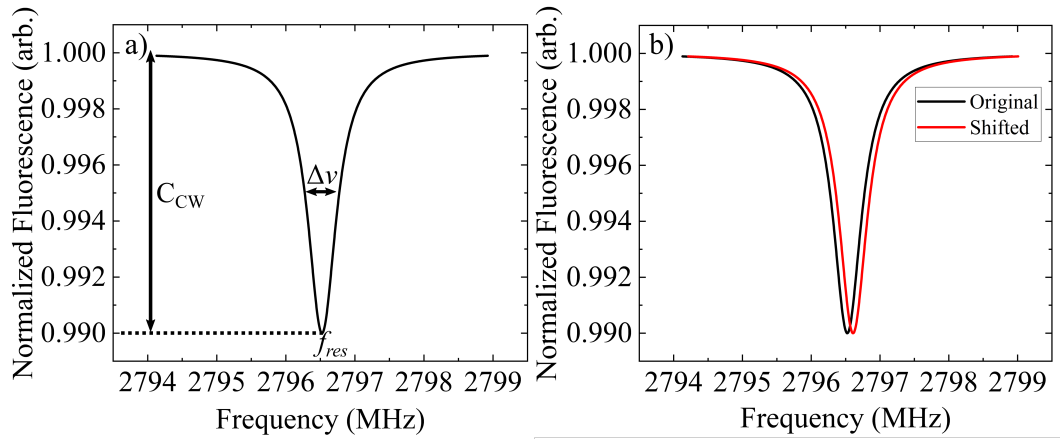


Figure 2.3: a) For the sake of simplicity a single resonance is considered i.e. the hyperfine interaction is neglected to illustrate the linewidth, $\Delta\nu$ and the contrast, C_{CW} . This was simulated using a Lorentzian profile with $C_{CW} = 1\%$ and $\Delta\nu = 0.5$ MHz and a magnetic field strength of 3 mT at an angle of 29° relative to the NV center causing a resonance to occur at f_{res} . b) The principle of magnetic field detection is demonstrated. In this instance a magnetic field shift of $3\mu\text{T}$ is applied to the NV center. If monitoring the resonance with a fixed applied frequency, i.e. f_{res} , the effect of a changing magnetic field induces a Zeeman-shift and thus the emitted fluorescence given by the NV center changes and thus the magnetic field can be detected.

where the P_f pre-factor takes the form of $\frac{4}{3\sqrt{3}}$ for a Lorentzian line profile or $\sqrt{\frac{e}{8\ln(2)}}$ for a Gaussian line profile. Under most circumstances the profile is well approximated by a Lorentzian and so the Gaussian contribution can be neglected [131], $\Delta\nu$ is the inhomogeneously broadened linewidth, equivalent to the full width at half maximum of the ODMR resonance, C_{CW} is the measurement contrast and is characteristic of the drop in fluorescence (it is the amount by which the fluorescence has decreased when on resonance compared to when not on resonance) and F is photon emission rate [81; 132] (see figure 2.3a).

For high sensitivity magnetometry using continuous wave (CW) schemes it is thus imperative to maximize the light collection from the NV center defects in diamond, and to have as low a $\Delta\nu/C_{CW}$ ratio as possible [133]. Achieving such high sensitivities is not necessarily a trivial task as several factors play a role in limiting the sensitivity. From the perspective of collecting photons from the diamond the biggest obstacle is the high refractive index of diamond, $n_d \sim 2.42$ which for a typical diamond-air interface (neglecting any optical losses) limits the collection efficiency to $\sim 4\%$ [46; 134] when collecting fluorescence from a single diamond surface. A variety of methods have been investigated to overcome this for both single centers [135; 136; 137; 138; 139] and ensembles [81; 134; 140; 141; 142; 143; 144; 145]. It should be stated that it is much easier to extract light from a single center as it is possible to shape the diamond surface around a defect that is placed near the surface to a geometry that can allow more light to escape. For an ensemble of defects the volume of emission can be on the scale of millimeters and thus it is harder to extract light from the diamond. Another key factor is achieving as low a $\Delta\nu/C_{CW}$ as possible; this is technically easy for a single center provided an inherently low concentration of defects is used. As a single center is a point defect a high microwave homogeneity isn't necessary however for an ensemble of defects a high homogeneity of the microwave driving fields [146; 147; 148] and the bias magnetic field is required as large inhomogeneities lead to each spin within the active sensing volume having differing resonance frequencies leading to artificial broadening of the linewidth [149; 150]. For an ensemble of defects, with no preferential orientation, C_{CW} is limited. For a single NV center $C_{CW} \sim 30\%$ is achievable [23; 61]; it is possible to focus on that defect alone and reject other sources of light. However, when interrogation an ensemble of NV centers and having a bias field that is not aligned to any particular orientation, see figure 2.2, there are 8 different resonant frequencies with four different orientations. Hence, when a magnetic bias field is applied only a quarter of the NV center spins will contribute to the magnetometry signal at a given resonant frequency, if a single microwave frequency source is used only a quarter of

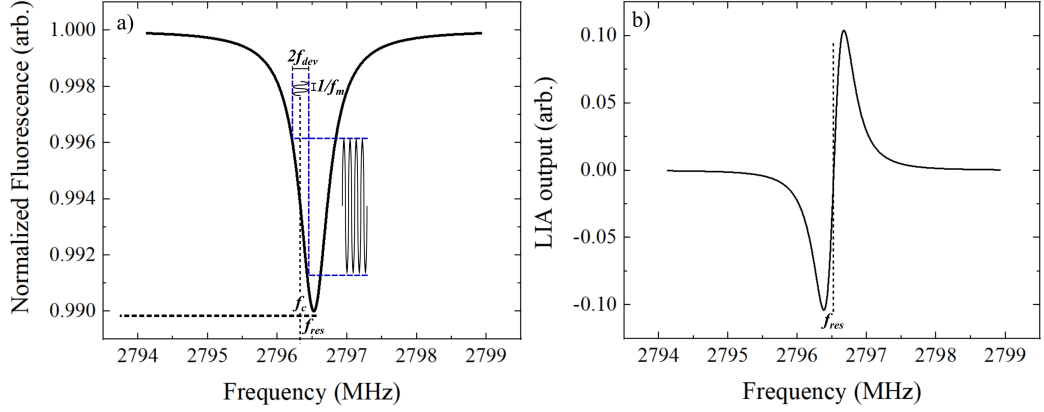


Figure 2.4: The principles of lock-in amplification (LIA) using frequency modulation of the NV center ODMR resonance is described using a simulated resonance. a) The original carrier frequency, f_c is modulated with a reference frequency of frequency amplitude/depth, f_{dev} and a modulation frequency f_m . b) The demodulated output of the original ODMR resonance scaled by a factor of 1000 for clarify. This profile is the derivative of the original NV center ODMR resonance but has a vastly superior signal-to-noise ratio due to the rejection of noise at frequencies away from f_m .

the NV centers will contribute with the other three orientations providing a background fluorescence at that frequency, reducing the contrast by a factor of four. In addition, background fluorescence from other defects, primarily NV^0 , also degrades the spin contrast, which is typically in the range of $C_{CW} \sim 0.1\text{-}3\%$ [133; 149]. It is possible to achieve higher spin contrasts by aligning the external magnetic field such that the resonances of different NV center orientations overlap [81; 151], this will enhance the spin contrast but the non-optimal magnetic field projection will reduce the sensitivity depending on the angle.

To achieve high sensitivities and detect minor changes to the frequency component of the resonance a lock-in amplifier (LIA) is typically used with a periodic change introduced either to the laser output or the carrier microwaves, which are either frequency or amplitude modulated. Typically the microwaves are frequency modulated as this offers the best performance in maximizing the sensitivity [81; 140; 152]. This scheme is demonstrated in figure 2.4. The ease of implementation of CW magnetometry has meant that to date almost all work related to the sensing of DC fields that make use of an ensemble of NV centers has been performed using this technique with the achieved sensitivities reaching $15 \text{ pT}/\sqrt{\text{Hz}}$ [81]. High sensitivities have also been achieved for vector implementations of NV center ensembles, sensitivities of $\sim 50 \text{ pT}/\sqrt{\text{Hz}}$ for each Cartesian coordinate are attainable [103]. The use of ferrite flux concentrators allowed a sensitivity of $0.9 \text{ pT}/\sqrt{\text{Hz}}$

to be achieved though the spatial resolution of sensing was degraded due to the magnetic flux being concentrated from a larger area [151].

2.6.2 Ramsey Magnetometry

Though significant progress has been made using CW methods, inherent issues exist which prevent truly high sensitivity magnetometry that is comparable to SQUID magnetometry. Due to the sensing occurring during the readout time the microwave radiation and optical readout are competing and thus an effect called power-broadening is introduced with the overall effect being a broadening of the linewidth [132; 149]. When there is an increase in the applied microwave power there is an increase in the linewidth, a higher microwave power leads to a greater measurement contrast but the NV center resonance linewidth $\Delta\nu$ also increases. As per equation 2.24 any increase to the linewidth decreases the sensitivity. If the microwaves are applied during the magnetic field sensing period it is not possible to avoid the effects of power broadening. To minimize the linewidth it is ideal to limit the application of the laser and microwaves to periods outside of when the NV center will interact with an external magnetic field i.e. the sensing period. Through not applying the laser and microwave during sensing it is possible to remove the effects of power broadening entirely.

For this reason alternative methods are currently under exploration with particular investigations into schemes which separate the microwave and laser excitation to overcome the limitations of CW magnetometry, such schemes are referred to as pulsed magnetometry because they do not involve continuous excitation of the ensemble. There are different pulsed schemes with the focus of this section being the Ramsey sequence. Under pulsed excitation schemes such as a Ramsey sequence the microwaves and laser pulses are separated from the instance where the spin system interacts with an magnetic field, see figure 2.5 and thus power broadening is removed [81; 133; 132]. Furthermore, due to the competition of microwave radiation and optical excitation there is a limit on the achievable sensing contrast, due to linewidth broadening and a limit of the optical power that can be supplied, as at sufficiently high optical intensities it is not possible to achieve a population difference and thus magnetometry is not possible [81; 133; 132]. It should be noted that significant homogeneity in the microwave and optical excitation is required otherwise degradation of the sensitivity will occur; these requirements are less stringent for continuous wave magnetometry. The shot-noise limit of a Ramsey type scheme is given by

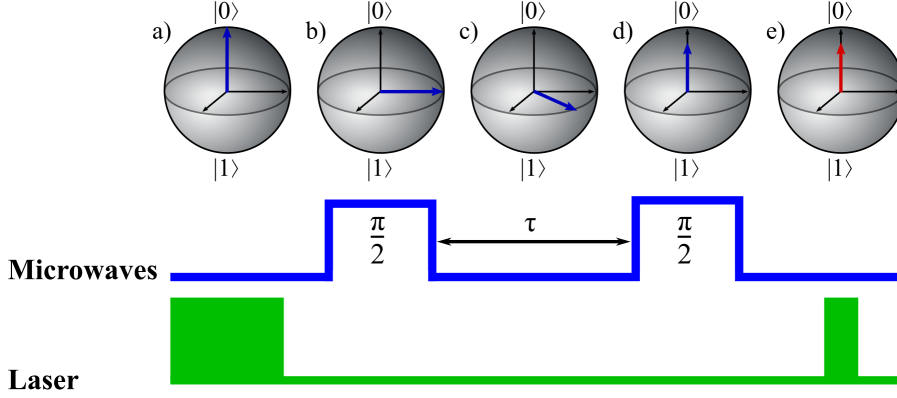


Figure 2.5: The Ramsey sequence is shown in the Bloch sphere with the corresponding pulse sequence for both the laser and the microwaves. a) The spin is initialized to the $|0\rangle$ through a 532 nm laser pulse. b) a $\pi/2$ microwave pulse is applied to create a superposition between the $|0\rangle$ and $|1\rangle$ states. c) No lasers or microwaves act on the system and it is allowed to evolve freely with a free precession time, τ . As the system is freely evolving the $|1\rangle$ states acquires a phase relative to the $|0\rangle$ state when interacting with an external magnetic field. d) A $\pi/2$ microwave pulse is applied to project the population difference between the $|0\rangle$ and $|1\rangle$ states onto the $|0\rangle$ and $|1\rangle$ basis. e) Pulsed laser excitation is then performed to readout the spin state and thus determine the magnetic field.

$$\eta_{\text{Ramsey}} = \frac{\hbar}{g_{\text{NV}}\mu_B} \frac{1}{\Delta m_s} \frac{1}{C_R e^{-(\tau/T_2^*)^p} \sqrt{\mathcal{N}}} \frac{\sqrt{t_I + \tau + t_R}}{\tau}, \quad (2.25)$$

where C_R is the contrast for a Ramsey measurement, T_2^* is the inhomogeneous spin dephasing time, p is the factor to account for whether the lineshape is Lorentzian ($p=1$) or Gaussian ($p=2$), $\mathcal{N} = N t_R$ is the average number of photons during the optical readout window, t_I is the initialization time and t_R is the readout time. The sensitivity is optimized for $\tau = T_2^*$ [133], when T_2^* is $< t_I + t_R$. The T_2^* is the time scale over which the spins dephase inhomogeneously due to variations in the local spin environment, with the most significant contributions relating to the ^{13}C [54] environment and the nitrogen spin bath. If a sufficiently high nitrogen concentration is used nitrogen tends to dominate the spin interaction relaxation [153; 154; 155].

Further benefits of a Ramsey type sequence is the ability to decouple other factors which affect the NV center, namely temperature and strain, as sensing schemes which allow interrogation of transitions between the $m_s = -1$ and $m_s = +1$ can be performed. The precession between the $m_s = \pm 1$ states is twice as fast and only couples to temperature to the second order [156; 157]. Furthermore, spin bath driving techniques can also be applied to reduce the effects of nearby paramagnetic

defects, which degrade T_2^* , such as other nitrogen related defects which contribute considerably to spin dephasing [150; 158]. Spin bath driving techniques are also compatible with continuous wave magnetometry.

To truly implement the improvements a Ramsey magnetometry type scheme offers, one would need to operate in an optically saturated regime to maximize the fluorescence received from an ensemble of NV center defects. However, the absorption cross-section of the NV center, $\sigma_{NV} = 3.1 \times 10^{-17} \text{ cm}^2$, is typically an order of magnitude lower than the value for other defects such as quantum dots [6; 112; 149; 159; 160] and thus high optical excitation intensities are needed, which is beyond the power output capabilities of most 532 nm commercial lasers if a large sensing volume is interrogated. The behavior of power saturation is governed by the following

$$F = F_\infty \frac{P_{Las}}{P_{Las} + P_{sat}}, \quad (2.26)$$

where F_∞ is the saturation fluorescence, P_{Las} is the applied laser power and P_{sat} is the power needed for saturation, i.e. how much power is needed to get half of the total maximum fluorescence [106]. In addition, at high optical excitation intensities there is an increased probability of photo-ionization leading to charge state conversion of NV^- to NV^0 [106; 81] which would significantly degrade the spin contrast. It should be noted that the literature is conflicting on the value of the absorption cross-section for the NV center, though most estimates (theoretical and experimental) place its value as being on the order of 10^{-17} cm^2 [159; 160; 161]. Another limiting factor would be the Gaussian TEM_{00} mode inherent to all good quality commercial laser beam outputs. The differing optical excitation of each NV center defect in the spin ensemble would require long initialization times to ensure efficient spin polarization into the $m_s = 0$ state which would degrade the sensitivity. A solution to this would perhaps be to modify the beam profile into a super-Gaussian profile achieving a more uniform intensity across the excitation volume [162; 163], this could be achieved by either a pair of aspheric lenses or a tophat beam shaper. Another necessity is the use of a microwave resonator to achieve high-homogeneity microwave radiation to drive all NV centers with similar dynamics [148; 147; 149; 164]. It is reasonable to foresee an enhancement of at least an order of magnitude through the use of pulsed techniques compared to CW magnetometry for a given excitation volume [81; 132; 133]. As such it is expected that all future high sensitivity magnetometry methods will employ pulsed methods for the sensing of DC magnetic fields.

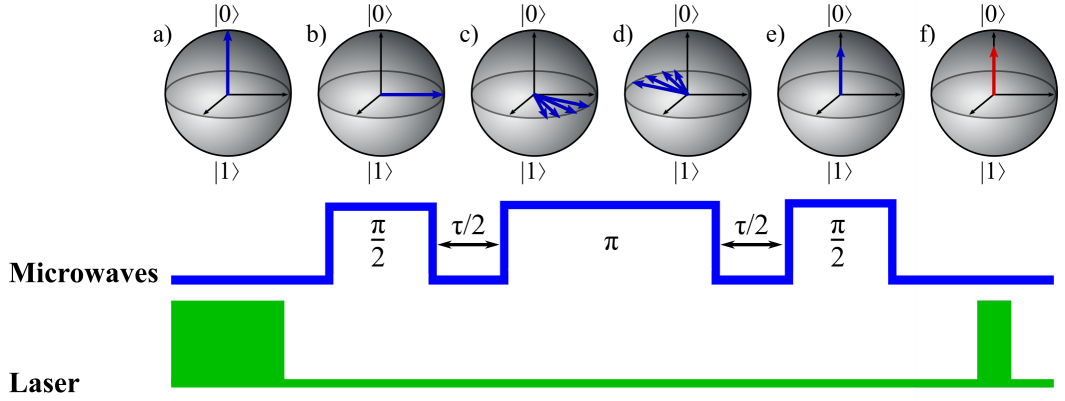


Figure 2.6: The Hahn echo sequence is shown in the Bloch sphere and the corresponding pulse sequence for both the laser and the microwaves is shown. The processes a), b), e) and f) are unchanged from Ramsey sequence magnetometry. However, in this scheme a π -pulse is introduced during the free precession time, τ .

2.6.3 Hahn Echo Magnetometry

The two techniques mentioned previously can sense magnetic fields from DC to a maximum of ~ 100 kHz and are fundamentally limited by T_2^* [133]. However, if an additional π -pulse, see figure 2.6, is applied during the free precession time the effects of the inhomogeneous spin environment can be reduced and the limit is now the homogeneous spin dephasing time, T_2 , which is typically at least an order of magnitude longer than T_2^* [54; 150; 154]. As a spin system evolves during its free precession time, the differences in local magnetic field environments leads to spin precession at different rates. The effect of the π -pulse inverts the phase such that each spin is allowed to unwind the same amount of phase. This process overall allows elimination of spin inhomogeneities whose fluctuations occur on a timescale that is longer than that of τ , this has the disadvantage of making it so that it is not possible to detect magnetic fields that oscillate with periods longer than T_2 . Magnetic fields oscillating at lower frequencies are partially averaged away so this scheme can only detect AC magnetic fields around one frequency. The sensitivity of ensemble NV center magnetometers that operate under this scheme have reached $0.9 \text{ pT}/\sqrt{\text{Hz}}$ [165] and it is feasible to expect that sensitivities through this method would be superior to those obtained through Ramsey magnetometry. For completeness it is stated that there are other sensing schemes but these are not mentioned as they are not relevant to this work.

Chapter 3

Diamond Synthesis and Characterization

3.1 Synthesis of Nitrogen-Vacancy Center Diamonds

To tailor the properties of a diamond for a given application it is necessary to have significant control over its growth and thus diamonds have to be synthetically grown. The significant improvements made over the last few decades now routinely allows for the growth of single-crystal high-purity diamond samples that are around $5 \times 5 \times 1$ mm; samples larger than this can be grown. It is possible to tailor the processes of growth and produce diamonds with the desired properties on demand with further work still ongoing to improve the quality of diamonds produced [166; 167]. The incorporation of defects, such as nitrogen, in diamond is primarily achieved in one of two ways, either through chemical vapor deposition (CVD) or high-pressure high-temperature (HPHT) synthesis. These techniques, particularly CVD, are common for the growth of many materials not just diamond. The fabrication of vacancy complexes, such as the NV center, in large quantities then involves some form of particle bombardment to induce vacancies. The irradiated diamond sample is then annealed to induce vacancy migration.

A great deal of research has been conducted into understanding the properties of the carbon phase diagram, see figure 3.1, with significant theoretical studies and corresponding experimental investigations of the thermodynamic and chemical processes, a review of this is beyond the scope of this thesis and thus any interested party is directed to references [168; 169; 170; 171; 172] for a more thorough understanding. Particular attention is drawn to the reviews undertaken by Yuri N. Palyanov *et al.* [173] and K. Nassau [174], both of which are good summaries of the

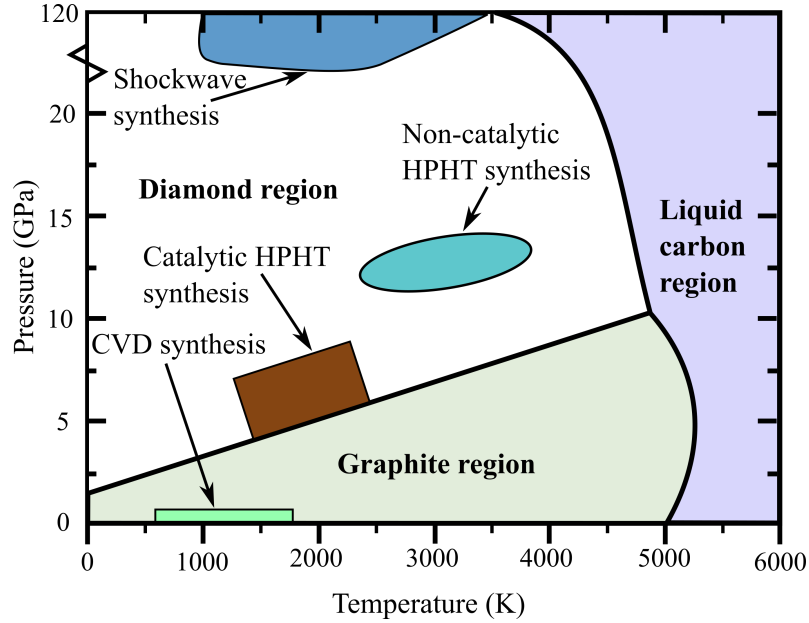


Figure 3.1: The phase diagram of carbon, the regions of growth of CVD, HPHT (catalytic and non-catalytic) and shockwave synthesis regions. The Berman-Simon line, the diamond/graphite equilibrium line is shown. The CVD synthesis region has been enlarged for clarity.

literature on diamond growth. It can be seen from figure 3.1 that at room temperature and atmospheric pressures, graphite is the stable allotrope of carbon while diamond is metastable. One would naturally surmise that growing diamond would simply require growth in the diamond stable region, however, even under conditions where diamond is the more stable form there is a very narrow window of growth, and indeed growth can even be accomplished in conditions more favorable to the stability of sp^2 hybridization, the graphite stable region. To produce diamond it is not sufficient to consider the thermodynamics of the reaction alone, one must also overcome the kinetic barrier to ensure the preferential formation of diamond rather than graphite [174; 168; 169; 170; 171; 175; 176]. The difficulty in accomplishing this task has led to many failed attempts at synthetic diamond growth and great debate on whether it was even possible to synthetically grow diamonds.

3.1.1 High-Pressure High-Temperature

The first successful instance of diamond growth was carried out in Sweden by Allmänna Svenska Elektriska Aktiebolaget [1; 177]. However, this successful growth of a synthetic diamond was not reported at the time and only came to light decades

later. It is for this reason that credit is given to the group that was actually second in growing a synthetic diamond. The techniques and methods of the second group form the basis of all modern HPHT diamond growth. The methods used by this group mimics the process through which natural diamonds are formed within the Earth, an area which is subject to high pressures and high temperatures.

The second instance of successful commercial diamond growth occurred at General Electric (GE) [178; 174], previous work had already found that conversion of graphite to diamond was insufficient to achieve diamond growth, even under growth conditions that were favorable to diamond [179] as the sp^2 bonding inherent to graphite needed extraordinarily high temperatures and pressures to induce breakdown into carbon [180]. The success achieved at GE, which was the first instance of a process for growing diamond that could be replicated independently, was due to the addition of molten transition metal solvent-catalyst; either nickel, cobalt or iron, or an alloy thereof, which helped dissolve graphite into carbon and simultaneously aided in the crystallization of diamond from the molten solution which lowered the pressure and temperature requirements [175; 181]. The other key factor that helped overcome previous problems was the design of a newer “belt” press that improved upon the previous anvil designs utilized by P. W. Bridgeman, allowing high pressures and high temperatures for extended periods of time [182; 174], with temperatures in excess of 2000 °C and pressures beyond 10 GPa achievable. Further work from the same group helped establish more details about the conditions where diamonds could form [181].

In the time since the early demonstrations of diamond growth many other methods of growth under the HPHT formalism have been considered with methods pertaining to catalyst-free diamond growth being found [183; 184] and the exploration of other catalysts [185; 186; 187]. As these require higher temperatures and pressures when compared to using nickel, cobalt and iron alloy complexes or need further investigation, or both, all commercial HPHT growth for industrial applications follows the growth principles established by Bundy *et al.* which can routinely occur at pressures of ~5-6 GPa and temperatures between the ranges of ~1200-1600 °C [168; 169; 170; 171; 173; 175; 178; 181], see figure 3.1. Information pertaining to the production of this figure was sourced from references [171; 188]. Growth through HPHT uses a press in which a diamond seed is placed at the bottom of the press. This region is then heated until the transition metal becomes solvent, this then dissolves the graphite (or another equivalent carbon source) into its constituent carbon form and through a temperature gradient, the dissolved carbon is transported through the molten solvent to the growth seed

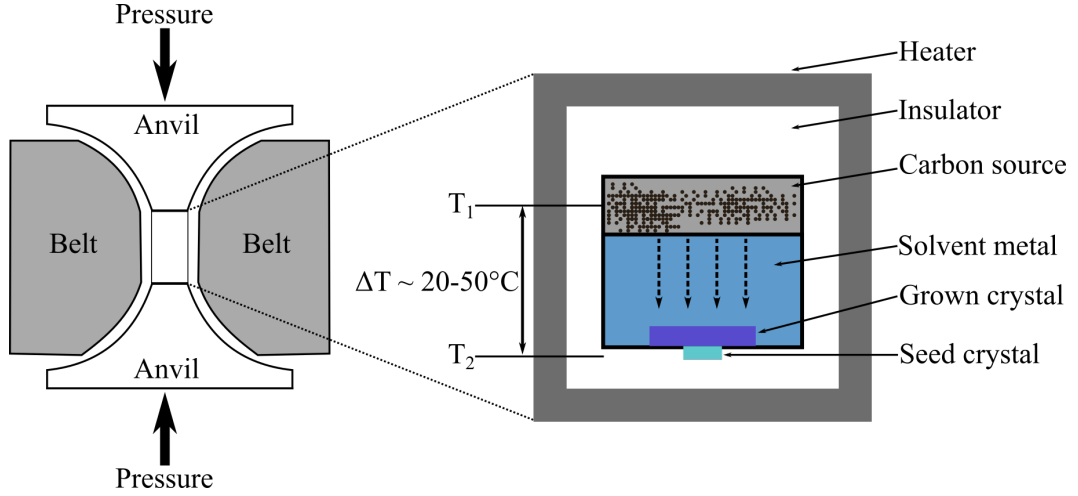


Figure 3.2: A schematic of the HPHT belt press showing diamond growth. The temperature difference between the carbon source and diamond seed is ΔT , where T_1 is greater than T_2 . The true morphology of the diamond is neglected for simplicity.

and precipitation causes the growth of diamond upon the seed. The diamond seed is held at a lower temperature to ensure diffusion of carbon toward the seed, see figure 3.2 [168; 169; 170; 171; 173; 175; 178; 181; 185; 189]. The exact method of generating the high pressures and high temperatures is dependent on the type of press used with the main press designs being the belt press (based on the original designs by Tracy Hall of GE), the cubic press or the BARS press [173].

The quality of the diamond produced through HPHT methods depends heavily upon the quality of the initial diamond seed and the purity of the initial carbon source used [190; 191]. Historically the diamonds produced through HPHT have incorporated many defects or have been polycrystalline [173; 185; 189] due to the poor quality of the raw materials used. As these growth processes are typically carried out under standard atmospheric compositions, there is typically significant nitrogen incorporation and under standard growth conditions it is not atypical to reach concentrations of approximately a few hundred ppm, with reported concentrations reaching as high as ~ 2000 ppm depending on the type of solvent-catalyst used [173; 192; 193]. At such high concentrations there is a significant single substitutional nitrogen, N_s^0 incorporation and the formation of many nitrogen related defects beyond N_s^0 . Details regarding these nitrogen related defects can be found in a review by M. Ashfold *et al.* [194]. Such high concentrations are unwanted here due to the resultant spin bath that is a noise source for high-sensitivity diamond based magnetometry.

For single center magnetometry ideal nitrogen concentrations would be as low

as possible, typically on the order of one part per billion (ppb). For ensemble NV center magnetometry it is believed that the ideal nitrogen concentration, prior to NV conversion is on the order of 1-10 ppm [154]; a compromise between maximizing NV center fluorescence and T_2^* . It is certainly possible to reduce the nitrogen uptake with two methods favored to achieve this. The first involves adding a “nitrogen getter”, typically Ti, Al, Co or Zr or some combination thereof, to the transition metal solvent-catalyst which preferentially interacts with nitrogen forming stable or transient nitrides. This confines most of the nitrogen to the melt but can lead to the inclusion of the “nitrogen getter” in the final diamond product which can be undesirable [173; 190; 195; 196]. The other method involves selective control of the composition of the atmosphere allowing for more selective incorporation of defects.

Typically the morphology of diamonds produced through HPHT is cubic-octahedral. Part of the reason for this is due to the different growth rates of the differing crystallographic planes, certain growth sectors are more favorable for growing. Different growth sectors also take up impurities at differing rates and thus it is typical for different growth sectors to have different concentrations. For magnetometry the varying concentrations and different orientations are problematic if a large area is excited within the diamond.

In addition, controlling the incorporation of defects and producing high quality single crystal diamonds during HPHT growth still remains a challenge and thus more selective growth techniques are required for quantum-related work. The diamonds produced through HPHT are thus typically employed as diamond cutting tools, drill heads or small grains for use as abrasives.

Nowadays, it is quite possible to fabricate low strain large HPHT single crystal diamonds with inherently low nitrogen concentrations with minimal inclusion of other unwanted defects [190; 191; 196; 197; 198] and it is routinely possible to now use a high quality diamond seed. Indeed HPHT diamonds with reasonable nitrogen concentrations have been employed for use in ensemble NV center magnetometry allowing for high sensitivities with very narrow NV center resonance linewidths [199].

A more selective method of growth is provided through CVD synthesis, it is the diamonds produced through CVD that are used in the majority of the publications concerning diamond magnetometry.

3.1.2 Chemical Vapor Deposition

CVD growth, in contrast to HPHT methods, is undertaken in the metastable growth region of diamond and takes place at lower temperatures, typically 700-1000°C, and pressures lower than atmospheric, typically 1-30 kPa. Though many different reactor

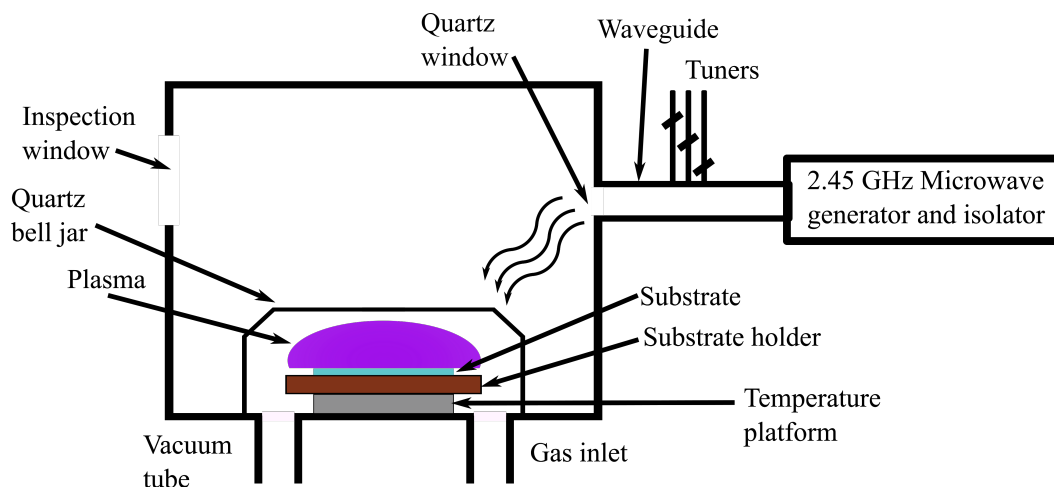


Figure 3.3: Schematic of a chemical vapor deposition microwave reactor.

types exist, the vast majority of CVD diamond growth takes place using either hot filament or microwave plasma reactors [167; 173; 176; 200]. In the case of a hot filament reactor tungsten is typically used for the filament and this could be a source of impurities that can be deposited onto the diamond during growth. Microwave plasma reactors, see figure 3.3, are favored by most groups and companies due to the superior control over growth they offer, which extends to long operation times and a purer growth environment.

In a CVD reactor diamonds are synthesized in hydrogen rich H_2/CH_4 mixtures, typically $< 5\%$ CH_4 , under non-equilibrium conditions, see figure 3.4 [201]. The H_2 dissociates into atomic hydrogen in a high temperature plasma medium which preferentially etches weak non-diamond sp^2 bonded material whilst also kinetically stabilizing the sp^3 diamond phase through the addition of CH_3 radicals [200]. This build up of the diamond can be thought of as a layer-by-layer build up which offers significant control over the inclusion of defects, with it being possible to achieve layers of different thicknesses and even delta-doped layers [202]. This layer-by-layer growth however does make the diamonds significantly more expensive than HPHT grown diamond and achieving thick samples does need constant growth conditions to be maintained over long periods of time. It is possible to increase the growth rates to minimize the time taken for growth: increases to the microwave power, modification of the gas composition, changes to the gas density (pressure) and substrate temperatures all modify the growth rate. However, higher growth rates tend to facilitate poor quality diamond growth [167; 173; 203; 204].

The addition of O_2 in small quantities ($< 2\%$) is favored under some growth

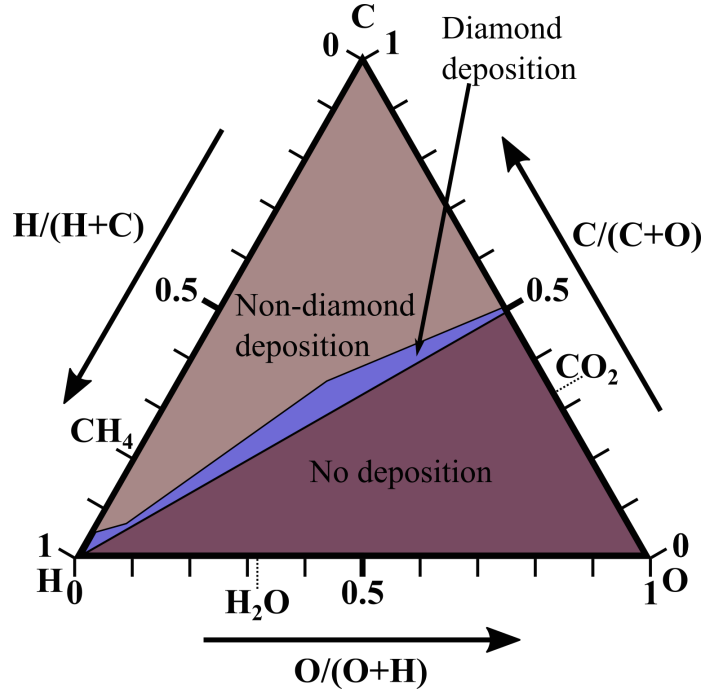


Figure 3.4: A simplified Bachmann diagram for CVD growth. Some compounds are listed to illustrate the principle of the diagram.

conditions as it limits the incorporation of unwanted defects and increases the etching rate of sp^2 carbon; details regarding ideal concentrations are reflected in figure 3.4. This has allowed for the production of defects in diamond with superior optical properties [205; 206]. Other gas mixtures can be added at various stages of growth to favor the incorporation of specific defects as and when required within the diamond.

As with HPHT growth the quality of the diamond grown depends heavily on the quality of raw materials. Single crystal high purity diamond growth is achieved through homoepitaxial growth with the employment of natural, HPHT or CVD-grown diamond seeds. In contrast, heteroepitaxial growth, performed using non-diamond material as the starting material leads to poorer quality polycrystalline diamond primarily due to the lattice mismatch between diamond (0.3567 nm) and the choice of substrate. It is possible to achieve single crystal growth heteroepitaxially using an iridium substrate, of lattice constant 0.3840 nm or c-BN, whose lattice constant is even closer to that of diamond (a 1.4% mismatch) [207; 208; 209; 210]. However, in the case of iridium the substrate is very expensive while for c-BN, it is not possible to fabricate large crystals limiting the size of diamonds to ~ 1 mm. As such currently, this only leaves iridium as the substrate of choice for heteroepitaxial growth of large single crystals. The cost can be minimized by iridium deposition on

another substrate [211]. All other substrates which have a close lattice parameter have tended to yield poor quality diamond. As such the use of diamond seeds as the starting material is preferred [173; 176; 212]. To enhance growth rates for polycrystalline diamonds, the substrate surface is scratched with a diamond powder to increase the diamond nuclear density by several orders of magnitude with finer diamond particles leading to higher quality samples [212].

Further to the need of high quality diamonds, if the diamond seeds used for growth contain dislocations these will propagate throughout the entire diamond during growth and induce strain into the diamond. For NV center magnetometry it is desirable to have inherently low strain samples to use. To minimize the propagation of strain, samples of very high quality are selected are typically polished or etched to minimize surface roughness.

The incorporation of nitrogen in CVD grown diamonds is achieved by addition of nitrogen to the plasma, this has the advantage of enhancing diamond layer growth rates though the diamond morphology is also changed [213]. Faster growth rates through CVD synthesis are achievable by increasing the microwave power and the pressure which leads to higher deposition rates. However the increase in microwave power would lead to increases in the manufacturing cost. The most efficient increase in the growth rate is achieved when the microwave power density increases and the methane density in the gas phase reaches a concentration of 4-5%.

The growth techniques of CVD currently are advanced enough that it is possible to have some control of the morphology of the diamond produced. A 100 crystallographic plane is commonly used as the base for the diamond seed.

3.1.3 Irradiation and Annealing

Beyond the techniques that shall be described in this section, there are other techniques which include laser writing defects through using ultrafast laser pulses to induce and/or migrate vacancies [214; 215], using a transmission electron microscope to induce vacancy creation [216] and controlled ion implantation to position defects near to the surface [217]. Though these methods often produce a large number of defects they tend produce defects in a localized area within the diamond. For this reason these methods are not commonly used for generating an ensemble of NV centers throughout diamond and are preferred when attempting to generate a single NV center at a particular site within the diamond. The focus of this section shall be techniques which allow defects to be generated throughout the entire diamond sample. Irradiation of diamond samples, as mentioned previously, involves some form of particle bombardment, with electrons, neutrons, protons, or ions used this will

displace carbon atoms from the diamond lattice creating vacancies and interstitials. To minimize damage to the carbon lattice and allow for deeper penetration into the diamond sample the majority of NV center production involves electron bombardment and as such shall be the only method discussed. Previous studies performed by Koike *et al.* [218] measured the displacement energy needed to produce vacancies (>180 keV) in a type IIa diamond; this was done for the three principle axes in diamond which required different electron energies to induce displacement. The optimum electron dose and energy still requires further investigation. Higher electron doses and energy lead to a higher NV center formation but also lead to greater lattice damage and the presence of other unwanted defects which can degrade the sensitivity [219]. The next step is to induce vacancy diffusion to encourage migration toward an N_s^0 defect. This requires that diamonds be annealed at a minimum temperature of 600°C ; any nearby N_s^0 acts as a trap and can capture the vacancy [220; 221]. It is quite likely that other vacancy-related defects could form once the vacancies are mobile. These would be detrimental both as a noise source and as they reduce the number of NV centers that are produced. In addition, certain defects could preferentially capture an electron leading to an NV^- becoming NV^0 . This is the case with divacancies which act as a deeper acceptor than NV^- and will pin the Fermi level. Divacancies are quite likely to form in samples that have been irradiated and annealed [222]. To maximize the formation of high quality NV centers multistage anneal schemes have been investigated and are employed, among the schemes that have been found a common scheme is the process developed by Chu *et al.* [223] this method is used to help anneal out unwanted defects whilst trying to maximize the formation of the NV center.

Under ideal conditions the irradiation and annealing processes would result in a 50% conversion of $[N_s^0] \rightarrow [NV^-]$, with minimal formation of other defects; the 50% arises from the need to have an $[N_s^0]$ be a donor so that the NV centers will exist in the $[NV^-]$ charge state. The optimization of the irradiation and annealing procedures are an area of active investigation with possible techniques including simultaneous irradiation and annealing [224].

3.2 Diamond Characterization

Diamond as a material can play host to a large number of defects and this causes significant changes to the material properties. For example, the incorporation of boron changes diamond from an insulator to a p-type conductor [225; 226]. For this reason it is common to classify diamonds based on the concentration and the types of defects

Diamond Classification Type
Type I: measurable nitrogen content
Type Ia: nitrogen aggregates
Type IaA: nitrogen aggregates into pairs
Type IaB: nitrogen aggregates into clusters
Type Ib: single substitutional nitrogen
Type II: no measurable nitrogen content
Type IIa: no nitrogen or boron impurities
Type IIb: boron impurities

Table 3.1: The classification of diamond according to the defect type and concentration.

present in the crystal lattice. Historically the foundation of characterization was performed through investigation of the absorption spectra of diamond [227; 228]. As the sophistication of characterization improved and the types of defects incorporated into natural and synthetic diamonds were determined, the characterization system evolved to be based upon the detectable level of nitrogen, see table 3.1, as measured through Fourier-transform infrared absorption (FTIR) spectroscopy [229; 230]. Nitrogen is chosen as nitrogen-related defects are the most common defects present in the diamond lattice [194; 230]. The vast majority of natural diamonds, approximately 98%, are characterized as type Ia with nitrogen concentrations as high as ~ 3000 ppm [231]. This leads to a yellow color if the nitrogen agglomerates into clusters (type IaB) while nitrogen pair defects (type IaA) - appear colorless. HPHT-grown diamonds are almost exclusively characterized as type Ib with the color being deep yellow or brownish color at high N_0^s (>100 ppm) concentrations. It is very rare to find natural diamonds that are type Ib. Due to the growth processes used in CVD growth, which does not need a nitrogen source, the vast majority of diamonds grown through this method are purer compared to natural diamonds and are thus classed as type IIa. It is also very rare to find natural diamonds with minimal defects. All information regarding diamond characterization, and the production of table 3.1 were found in references [229; 230]. Among the key methods for characterization of defects and their concentrations are ultraviolet-visible (UV-Vis) spectroscopy, FTIR spectroscopy and EPR. These techniques are the focus of the next sections. Other techniques can be used to aid in the characterization.

3.2.1 Photon Absorption

The usage of electromagnetic waves to investigate a material is possible as the waves themselves will be modified when interacting with the material; the inclusion of de-

fects will also lead to changes to the electromagnetic waves with each defect typically causing different changes. UV-vis and FTIR both rely on the transmission of photons through a sample and measuring the properties of the transmitted beam. Both methods are quick to implement, efficient in their performance and yield information about the physical properties and chemical composition of defects in diamond [232]. Optical transitions in any material are due to changes to the electron environment. An electron will be sent to an excited state with changes in its energy corresponding to the difference between the energy levels involved in the transitions. Probing the ground and excited states uses photon energies typically in the range of $\sim 1\text{-}5$ eV and thus in the UV-vis range [233]. In addition while in an excited state an electron can decay through non-radiative transitions producing phonons in the lattice. This is expressed through equation 3.1,

$$\hbar\omega = (E_2 - E_1) + j\hbar\Omega_2, \quad (3.1)$$

where ω is the photon angular frequency, E_2 and E_1 are the lowest energy levels of the excited and ground state, j is an integer and Ω_2 is the phonon angular frequency [234]. Vibronic transitions are probed through FTIR and typically require photons whose energies are less than 1 eV [233]. The absorption of any electromagnetic wave through a medium is governed by the Beer-Lambert law

$$I_T = I_0 e^{-\alpha t}, \quad (3.2)$$

where I_T is the transmitted intensity of light after passing through the sample, I_0 is the light intensity before entering the sample, α is the absorption coefficient and t is the thickness of the sample under investigation [235]. The absorbance, $A(\alpha)$ of a sample can be defined as

$$A(\alpha) = \log_{10}\left(\frac{I_0}{I_T}\right). \quad (3.3)$$

Equation 3.2 is valid only when reflections of any electromagnetic wave within the diamond sample is ignored. However, for the vast majority of samples which have a refractive index that is typically larger than air, when electromagnetic waves are passed through a sample there will be etalon effects where photons are internally reflected multiple times. This is particularly true for very high refractive materials such as diamond where there will be significant etalon effects. In the case of diamond the material has a refractive index of 2.42 and thus 17% of all light will be reflected. The number of reflections are dependent on the geometry of the sample however most synthetic samples are grown to a rectangular geometry, for example a sample may

have dimensions such as $3.0 \times 3.0 \times 0.5 \text{ mm}^3$. For such geometries these reflections of light occur multiple times leading to multiple instances of internal reflection which will result in differing optical path lengths and introduce a phase shift to the photons. To account for these effects equation 3.2 is modified such that

$$I_T = \frac{I_0(1 - R)^2 e^{-\alpha t}}{1 + R^2 e^{-2\alpha t} - 2R e^{-\alpha t} \cos(2knt)}, \quad (3.4)$$

where R is the reflection coefficient at the material/air interface, k is the photon wavenumber in a vacuum and n is the refractive index. The $\cos(2knt)$ term in the denominator is representative of a beating effect that occurs in thin samples. This effect can be removed by tilting the sample so light is not normal at the point of incidence i.e. one can wedge the sample to reduce etalon effects. Furthermore, absorption of photons is highly dependent on the color centers present and their concentration which is characterized by the absorption cross-section of a defect; this is also affected by the reflectance and sample thickness which is taken into account by introducing modifications to eqn. 3.4

$$\mu = \frac{1}{t} \ln\left(\frac{I_0}{I_t}\right) + \ln(1 - R)^2. \quad (3.5)$$

3.2.2 Fourier-transform infrared absorption spectroscopy

The principles of FTIR are based upon the interaction between photons with the instantaneous dipole moment which arises from the zero point motion of the atom. Experimentally an FTIR spectrometer makes use of a modified Michelson-Morley set-up, see figure 3.5. A non-monochromatic IR source is collimated and passed through a 50/50 beam splitter; half the photons are directed to a stationary flat mirror while the other half are passed to a flat mirror that is designed to move relative to the beam splitter. The two beams reflect off of their respective mirrors and interact with each other at the beam splitter. As one mirror is constantly moving relative to the other the resulting interference signal produced by the interference between the two beams contains all IR frequencies which come from the source and allows simultaneous measurements of all frequencies. The interference beam is passed through the sample and any peaks in the resulting FTIR spectrum will be the result of dipole changes which arises due to the unique characteristics of the sample. In diamond the maximum frequency vibration that can propagate through diamond is 1332 cm^{-1} [236]. FTIR has proved particularly useful for the gemological industry in identified the differences between natural, synthetic, HPHT-treated and irradiated and annealed diamonds [237; 238].

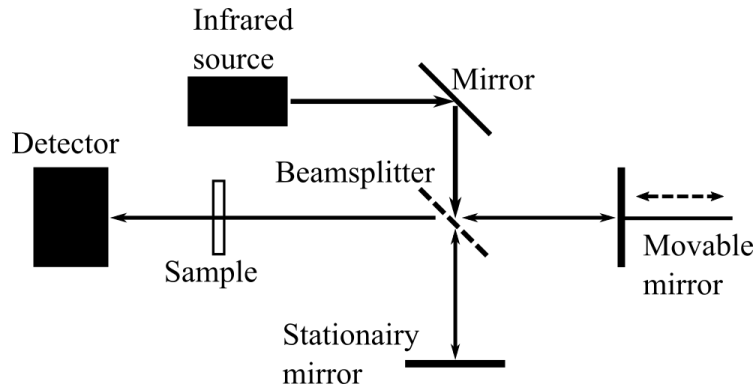


Figure 3.5: A modified Michelson-Morley set-up used for Fourier-transform infrared absorption spectroscopy measurements.

All FTIR measurements performed in this thesis used a PerkinElmer Spectrum GX FTIR spectrometer. All measurements were made in the mid-IR region which were between the range $300\text{--}7800\text{ cm}^{-1}$. The excitation source is a globar while a triglycine sulphate detector is employed. A beam condenser is used to focus the source down to a beam diameter that is approximately 1-2 mm spot. To minimize the absorption from carbon dioxide and water molecules that are typically present in the atmosphere the sample chamber is purged with dry N_2 gas. All FTIR spectra are analyzed by using software produced by the Warwick Diamond group called SpectrumManipulator. To determine defect concentrations all absorption data is normalized to a diamond that is defect free. Such a diamond produces an absorption coefficient of 12.3 cm^{-1} at 2000 cm^{-1} . This allows for the conversion of absorption to an absorption coefficient allowing for quantitative analysis.

3.2.3 Ultraviolet–visible absorption spectroscopy

In the case of UV-vis, the electronic structure of the material under inspection is probed. The electronic orbitals of atoms/ molecules and defects in solids have characteristic energies giving rise to a discrete set of energy levels. Measurements using UV-vis are typically in the wavelength range 200-800 nm, with $\sim 200\text{--}400\text{ nm}$ being the UV range and $\sim 400\text{--}800\text{ nm}$ being in the visible range and are measurements obtained of the absorbance against wavelength which allows for the identification of defects through the peaks that arise in the spectra. Most defects in diamond are optically active and hence this is a useful characterization technique.

All UV-Vis absorption spectra were recorded with a PerkinElmer Lambda 1050 spectrometer. Two optical sources are employed to allow for broad excitation a deuterium lamp for excitation in the UV range and a tungsten filament lamp

for the NIR-visible range. Two detectors are employed; a photomultiplier tube for visible-UV measurements and an InGaAs detector for NIR measurements. To remove any signals that could originate from the background, spectra are taken when no sample is present and then subtracted from the absorption data when samples are characterized.

3.2.4 Electron Paramagnetic Resonance spectroscopy

The theory of EPR has been discussed in section 2.3 and is used to investigate spin transitions of paramagnetic molecules. As the term paramagnetic suggests, it only allows for defects which possess an unpaired electron. Defect identification typically is done through using the Hamiltonian, see section 2.3. Unlike ODMR, which uses a fixed magnetic field and varies the microwave frequency to identify transitions, EPR relies on using a fixed microwave frequency and sweeping the magnetic field to identify transitions which correspond to the defect environments. Further information of the experimental techniques are found in the textbook by Eaton *et al.* [239] and Schweiger and Jeschke [121].

Experimental Procedure

For the purposes of the quantifying the differing defects and their respective concentrations in a given diamond continuous wave and rapid passage measurements were taken; pulsed EPR measurements were taken to determine spin relaxation times. Quantitative measurements to determine defect concentration in CW EPR were performed by taking EPR spectra until saturation was reached, i.e. where the response of the spin system is no longer linear with respect to the applied microwave power. The intensity response of the system under investigation is recorded as a function of the applied microwave power until the response is no longer linear. CW EPR is normally performed under what is termed the “slow passage” regime; in this case the experimental time is much longer than the spin relaxation time of the defects under inspection. The integrated signal intensity (those that were not saturated) of all analyzed samples were compared to a reference sample; the concentration of defects within this sample is very well established through a variety of methods and techniques. To take into account various changes in the environment which may cause slight changes to the intensity response of the reference sample a reference spectra is taken prior to characterizing an unknown sample.

All EPR measurements were performed in either the X-band or the Q-band. Typically the frequency ranges for the X- and the Q-band EPR are respectively 9-

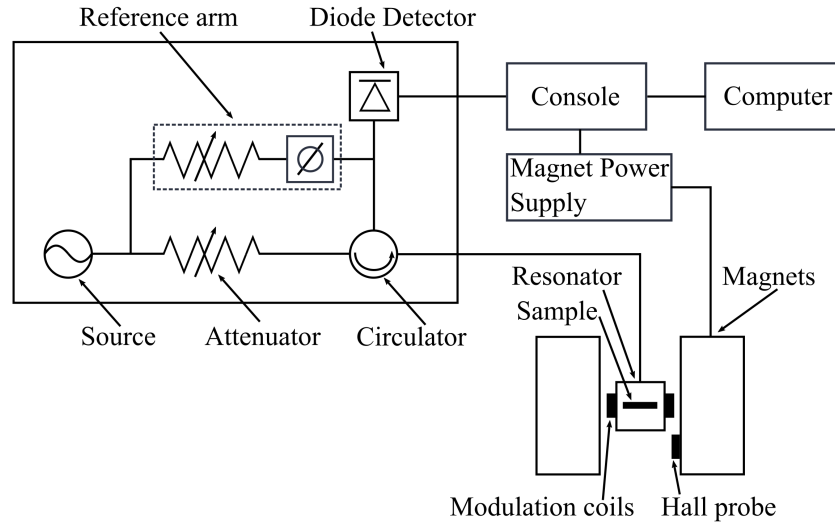


Figure 3.6: The components of the EPR spectrometer.

10 GHz and 33-35 GHz. The nominal frequencies for the experiments performed on the diamond samples used in this work were respectively 9.75 GHz and 34 GHz for the X- and the Q-bands.

In a typical EPR spectrometer for CW experiments, see figure 3.6, a sample is placed in a resonantly coupled microwave cavity. The cavity is placed between two large magnets which are capable of generating magnetic fields on the order of one Tesla. As diamond samples are typically not larger than $4 \times 4 \times 1 \text{ mm}^3$ the magnetic field produced over the sample under inspection is highly homogeneous and highly static. The microwave resonator is connected to a microwave bridge which is used for microwave generation; a biased detector is used to detect the reflected microwaves. A fixed microwave frequency is applied while the magnetic field is swept; once the magnetic field value corresponds to the field needed to excite a resonant transition in the spin system under investigation the microwaves will be absorbed by the spin system. An attenuator is used to adjust the delivered microwave power. This absorption will change the resonator impedance which will lower the quality factor causing some of the microwaves to be reflected; a microwave circulator is used to ensure that any reflected microwaves are detected by the biased detector rather than being sent back to the microwave source.

To enhance the signal-to-noise ratio, phase-sensitive detection is employed using a LIA with the modulation of the externally applied magnetic field. This signal is demodulated with the recorded signal having the same phase and frequency as the applied modulation; the result is a derivative of the original signal while all

other signals are rejected. To maximize noise rejection whilst minimizing signal distortion a frequency modulation of 100 kHz was used while the field modulation was always less than a tenth of the applied natural EPR linewidth. If the field modulation was larger than a tenth of the natural EPR linewidth applied this would distort the derivative EPR signal.

Chapter 4

Subnanotesla Magnetometry with a Fiber-Coupled Diamond Magnetometer

4.1 A Fiber-coupled Diamond Magnetometer

Magnetometers based on the NV center in diamond have steadily demonstrated a wide variety of applications. However, most of these magnetometers have been built on optical tables and thus have been confined to the lab. This is in contrast to other magnetometer systems such as fluxgate magnetometers which have already found commercial application in a range of fields. As most diamond-based magnetometers are confined to the lab they are limited in portability and hence in application. For diamond magnetometers to be used in areas such as medical diagnostics, systems that are portable and not confined to experimental labs will have to be built. To provide greater portability some of the more recent published works provide more compact systems with many of these making use of a fiber for excitation and fluorescence collection of NV centers. However, a drawback of these newer systems has been their limited sensitivities; the sensitivity of these portable devices have typically been at least an order of magnitude lower than the systems that are confined to an optical table. Many of the fiber-coupled diamond magnetometers have used either nanodiamonds or microdiamonds that are directly attached to the end of a fiber; the sensitivity of each of these magnetometers were in the range of 56000-180 nT/ $\sqrt{\text{Hz}}$ [240; 241; 242]. Another fiber-based diamond magnetometer utilized a two-wire microwave transmission line, this magnetometer was able to achieve a sensitivity of approximately 300 nT/ $\sqrt{\text{Hz}}$ [243]. A fiber-based system that was set-up

as a gradiometer was able to achieve a sensitivity of $35 \text{ nT}/\sqrt{\text{Hz}}$ with a projected shot-noise sensitivity that would allow for magnetocardiography (MCG) [244; 245]. It has also been demonstrated that portable magnetometer systems are achievable without the need to fiber-couple the system however the sensitivities for these systems are typically inferior to other NV center ensemble magnetometer systems, for example a compact light-emitting-diode (LED) design could detect a field as low as $1 \mu\text{T}$ for a 1 ms integration time with minimal power consumption [246].

All methods to determine the sensitivity of the magnetometer will involve monitoring the signal output of the LIA for one second at the point of the zero-crossing slope (the steepest part of the NV center resonance) and taking a fast Fourier-Transform (FFT); this yields the spectral noise density for a given magnetometer signal. The sensitivity of a magnetometer can be determined in several ways, each method involves some form calibration to determine the magnetometer response. The best sensitivities for diamond magnetometer systems which use a fiber at the time of publication of the paper this chapter is based on (2020) were able to achieve a sensitivity of $35 \text{ nT}/\sqrt{\text{Hz}}$, this was demonstrated by applying known test fields to determine the magnetometer response [244; 245]. Another magnetometer system was able to achieve a sensitivity of $1.5 \text{ nT}/\sqrt{\text{Hz}}$ [247]; the sensitivity here was determined by utilizing the signal-to-noise to linewidth which can be extracted from the derivative slope of an ODMR spectrum. Since then other fiber coupled systems have been able to achieve superior sensitivity values. The focus of this chapter is the discussion of a fiber-coupled magnetometer that at the time of publication represents the most sensitive fiber-coupled magnetometer [248] with a sensitivity of $(310 \pm 20) \text{ pT}/\sqrt{\text{Hz}}$ in the frequency range of 10-150 Hz when aligned along (111). The control instrumentation and all related optics are contained in a $0.44 \text{ m} \times 0.55 \text{ m} \times 0.6 \text{ m}$ box on wheels which has been successfully operated outside of the lab; the sensor head is connected to this box by way of an optical fiber and a microwave cable. This system was the first published work that was able to achieve a sub-nanotesla sensitivity for a fiber-coupled diamond magnetometer. It was possible to achieve this sensitivity through the use of low-strain ^{12}C diamond, an optical fiber, and a pair of aspheric lenses that were used for excitation and collection which allows for a small portable sensor head that can be brought to within 2 mm from the magnetic field source of interest. In addition, the other factors that allowed such a high sensitivity was the optimization of the microwave parameters, specifically the microwave power, frequency modulation amplitude and modulation frequency. The aluminum substrate of the microwave antenna was chosen due its good thermal conductivity. To minimize the linewidth a homogeneous bias magnetic

field was used and the components closest to the sensor head were chosen to be non-magnetic. A balanced detector was also used to reduce the amplitude noise from the laser and a LIA used to enhance the signal and reject noise. The balanced detector is a component that has two photodiodes, one of the photodiodes will receive the red fluorescence emitted by the NV centers, the other will receive a portion of the laser beam used for NV center excitation. By subtracting the portion of the laser beam from the NV fluorescence any amplitude fluctuations due to the laser can be removed.

After the publication of the paper this chapter was based on further enhancements to the system allowed a sensitivity of (120 ± 20) pT/ $\sqrt{\text{Hz}}$ in the frequency range of 10-200 Hz. This was achieved when the bias magnetic field was aligned along (100). More recent fiber-coupled magnetometers have been able to achieve a comparable sensitivity to that which was achieved in this work with a more compact magnetometer than that which was developed at Warwick demonstrating a sensitivity of 344 pT/ $\sqrt{\text{Hz}}$ [249]. Another more recent fiber-based magnetometer was able to achieve a sensitivity of 35 pT/ $\sqrt{\text{Hz}}$ with a bandwidth of 4.1 kHz this system used a Ramsey based approach rather than CW magnetometry [250].

4.1.1 Zero-Crossing Slope

For a CW magnetometry experiment the output of the LIA is directly correlated with changes to the fluorescence of the NV center ensemble and as there is a direct relation between the magnetic field response and the LIA output, the noise in the LIA output can yield the sensitivity of the magnetometer. This change can be determined by fitting to the linear region of the derivative signal of the NV center resonance and determining its gradient which provides a direct relation of the LIA's output (the change in voltage) to the change in the fluorescence output (frequency shift induced). Through this relation and the fact that the frequency shift induced in the NV center resonance is well known (the value of 28 Hz/nT is directly found from equation 2.2) a calibration constant can be determined that directly relates the voltage change output to the magnetic field change that induced said voltage change. This is one of the two methods used in this chapter to determine the magnetometer sensitivity.

4.2 Diamond Material Properties

The diamond employed to achieve a sub-nanotesla sensitivity was a 99.995% ^{12}C -enriched diamond plate with a (100) orientation whose dimensions were approxi-

mately $4 \times 4 \times 0.6 \text{ mm}^3$. As the diamond employed in this work was isotopically purified the NV center resonance linewidth is narrower as the ^{13}C which provides a source of decoherence is reduced [54]. This allows for a NV center magnetometer to reach a higher sensitivity, though at the expense of the dynamic range. The sample was grown through CVD and it is estimated that there is a conversion efficiency of 20% of nitrogen-to-NV; this sample was provided by Element Six. The diamond was electron irradiated and then annealed. The concentration of defects in this diamond sample were determined by using EPR, FTIR and UV-Vis, photoluminescence maps were also taken to assess sample homogeneity.

4.2.1 Electron Paramagnetic Resonance Measurements

EPR measurements were performed using a Bruker EMX spectrometer equipped with a 90 dB microwave bridge and a Bruker super high Q microwave cavity. The concentration of defects are found to be (2.8 ± 0.2) ppm of negatively charged NV center, (5.3 ± 0.5) ppm for neutral substitutional nitrogen and (1.5 ± 0.2) ppm of negatively charged hydrogen nitrogen vacancy (NVH). Pulsed EPR measurements were also taken using a Bruker E580 equipped with a MD5 resonator; from this it is established that T_2^* , T_2 and T_1 are 750 ns, $1.3 \mu\text{s}$ and $5100 \mu\text{s}$ respectively. The extracted linewidth using the pulsed EPR T_2^* time as a reference yields a linewidth of 0.42 MHz.

4.2.2 Absorption Measurements

FTIR and UV-Vis measurements, shown in figure 4.1, were performed with the concentration determined to be 4.6 ppm for negatively charged NV center and 0.8 ppm for neutral NV center and is found from using the intensities of the 637 nm and 575 nm zero-phonon line respectively. The concentrations from FTIR were established to be 5.6 ppm for neutral substitutional nitrogen (N_s^0) and 3 ppm for positively charged substitutional nitrogen (N_s^+). It is believed the discrepancy between the NV concentration found through UV-Vis and EPR are due to charge-transfer effects. The concentrations for FTIR and UV-Vis are determined by normalizing the obtained spectra and using known calibration constants to work out the concentration of a particular defect.

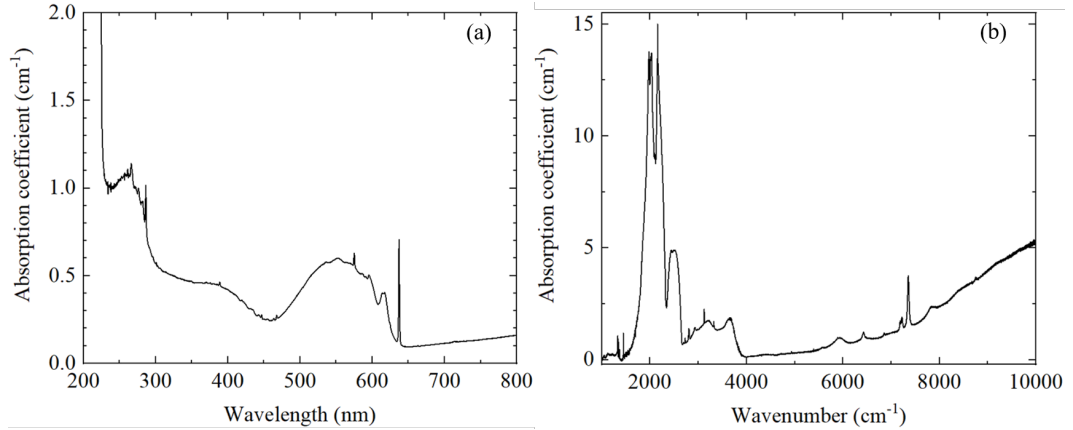


Figure 4.1: (a) The UV-Vis data which determined the neutral and negatively charged concentrations of NV center. (b) FTIR data which was used to determine concentrations of neutral and positively charged substitutional nitrogen defects.

4.3 Magnetometer Design

Excitation of the NV center defects are achieved through the use of a Laser Quantum Gem-532. This laser has a maximum power output of 2 W, but 1 W of laser power excitation was used for the results obtained in this chapter. This was to reduce the noise output of the laser which is believed to be caused by mode hopping of the laser due to the laser head reaching a temperature which is on the cusp between two frequency modes. The noise was spurious and intermittent but when present the sensitivity was degraded by at least an order of magnitude. At 1 W of power this spurious noise was severely reduced and this laser power was preferred. The experimental set-up is shown in figure 4.2. The magnetometry method employed here is CW magnetometry.

The output of the laser beam is directed to a 100:1 ratio beam sampler (Thorlabs BSF10-A) which is designed to pick off 1% of the laser power. The picked-off portion is supplied to the reference arm of a balanced detector (Thorlabs PDB450A). The remaining high-intensity portion of the laser beam is steered using a mirror through a dichroic filter (Thorlabs DMSP650) and then focused using an aspheric lens (Thorlabs C171TMD-A) into a custom-ordered 0.22 N.A. fiber with a core diameter of 400 μm (Thorlabs FG400AEA-Custom). The fiber end closest to the laser source is steel terminated while the end that attaches to the sensor head (closest to the diamond) is ceramic; this was done to minimize the number of magnetic sources near the diamond to prevent noise. The steel termination was chosen to ensure the fiber end closest to the fiber would not be damaged at high intensity

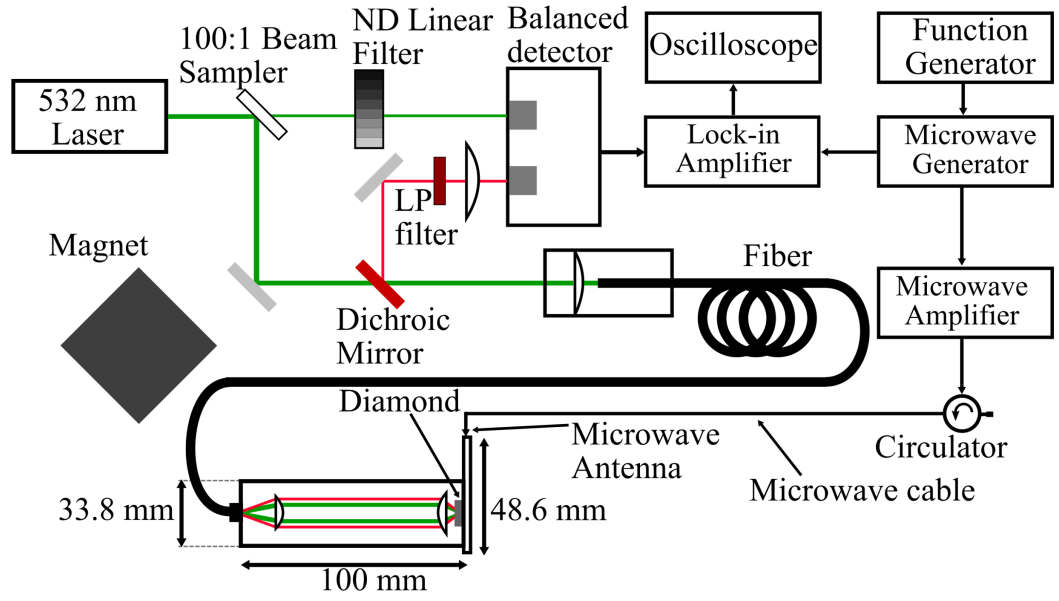


Figure 4.2: A schematic of the fiber-coupled diamond magnetometer. The dimensions of the sensor head are shown but other components are not drawn to scale. The terms ND and LP are respectively the abbreviations for neutral density and long pass. The hyperfine excitation was provided by the function generator. The bias magnetic field was used for alignment of the NV center resonance to a particular crystallographic orientation.

laser powers. The fiber output is collimated using an aspheric lens of 0.3 N.A. (Thorlabs C171TMD-A); the collimated beam is then focused using an aspheric lens of 0.68 N.A. (Thorlabs C330TMD-B); the first lens is housed in an SM1 lens tube (Thorlabs SM1L30) while the higher N.A. asphere is placed in an adjustable SM1 zoom house (Thorlabs SM1NR05) which is capable of mounting half-inch optics. The same lens arrangement is used to collect the fluorescence emitted by the NV center ensemble from the diamond. It is estimated that the sensing volume is $\sim 600 \text{ } \mu\text{m} \times 4650 \text{ } \mu\text{m}^2$; this is based on a measured beam waist of $\sim 38 \text{ } \mu\text{m}$ and the known thickness of the diamond. The red fluorescence is then separated using a 650 nm shortpass dichroic mirror (Thorlabs DMSP650), filtered using a 650 nm longpass filter (Thorlabs FELH650) and focused onto the signal photodiode of the balanced detector. The balanced detector is used to cancel out laser intensity fluctuations which would otherwise degrade the magnetometer sensitivity, published works have reported enhancements of up to a factor of 30 in the sensitivity [103] through being able to remove intensity fluctuations. Optimum noise cancellation was achieved when the incident intensity upon the reference photodiode is matched with the illumination intensity of the red fluorescence that is incident upon the signal photodiode for balanced detectors that use subtraction to reduce noise. The illumination levels are matched when on a magnetically sensitive resonance with an enhancement of a factor of 11 achievable in the sensitivity. The enhancement in the sensitivity is reduced to a factor of 3 when the intensity incident upon the signal and reference photodiodes are unmatched. The improvement in sensitivity is compared to when only the red fluorescence is used with no subtraction using the reference photodiode. It should be noted that large scale movements to the fiber causes changes to the coupling efficiency and can introduce modal noise, this manifests as variations in the number of photons collected on short timescales which in turn manifest as noise in the magnetic field measurements. These changes can be interpreted as a magnetic signal and have been shown to degrade the sensitivity.

4.3.1 Sensitivity Optimization

To optimize the sensitivity of the magnetometer a series of measurements were undertaken with modifications to the parameters relating to the microwaves delivered to the NV ensemble. For each varied parameter a corresponding ODMR spectrum was taken and the zero-crossing slope (ZCS) determined in each instance; the larger the value of the ZCS the greater the responsivity of the magnetometer and thus the more sensitive it is. Though a larger ZCS suggests a better sensitivity, provided the same experimental parameters are used, this is not absolute; under certain conditions

the sensitivity may be worse even with a larger ZCS value.

4.3.2 Microwave and Electronics

Microwave excitation is provided by an Agilent N5172B microwave source with its output supplied to a Mini-Circuits ZHL-16W-43-S+ microwave amplifier. An arbitrary function generator (RSPRO AFG21005) is used to supply a 2.158 MHz sinewave which is supplied to the I/Q inputs of the Agilent. The mixing of a 2.158 MHz sinewave allows for the simultaneous excitation of three frequencies, in this instance of the nitrogen-14 ($m_I = -1, 0, 1$) hyperfine resonances leading to an enhancement in the spin contrast of the NV center ensemble; instead of three resonances there will be five resonances instead this is termed hyperfine excitation. The amplified microwave output is passed through a 2-4 GHz coaxial circulator to reduce microwave back reflection. This is then supplied to a 2 mm diameter copper loop deposited onto a ~ 1.7 mm thick aluminum prototyping board (C.I.F AAT10). Aluminum was the choice of substrate as it has a higher thermal conductivity than materials such as FR4; FR4 is a fiberglass based epoxy resin that is commonly used for printed circuit boards. High thermal conductivity is needed so the diamond does not get too hot. Aluminum is much less efficient than FR4 at delivering microwaves. The diamond is placed at the center of the copper loop. The 1.7 mm thickness of the aluminum board is the ultimate limiting factor with regards to how close the diamond can be brought to a magnetic field source of interest. The microwaves are square-wave frequency modulated [251]. For the purpose of enhancing the sensitivity the carrier microwaves are modulated at a specific microwave frequency modulation and frequency modulation amplitude. The subtracted signal from the balanced detector is supplied to a Zurich MFLI DC - 500 kHz LIA with the reference frequency (information regarding the microwave frequency modulation and frequency amplitude parameters) supplied to the Agilent. The use of frequency modulating the microwaves allows the LIA to extract the magnetometry signal whilst rejecting the noise components that occur at all other frequencies that do not occur at the modulation frequency. To maximize the noise rejection and boost the extracted magnetometry signal it is important to find the optimum modulation frequency and frequency modulation amplitude; these measurements were performed. The NV center resonances were separated by a permanent rare earth magnet with the bias field aligned to a (111) crystallographic orientation; the frequency splitting is found to be $\Delta f \sim 114$ MHz yielding an applied bias magnetic field of ~ 2 mT.

4.3.3 Microwave Delivery System

As the sensor head configuration is miniaturized and light tight it is not possible to assess the beam waist of excitation or determine the performance of the multimode fiber and the aspheric pair lens combination from within the sensor head when the antenna is screwed on. Investigations were done to determine how bad the chromatic aberration is between the excitation (green 532 nm laser) and the collection (red NV center fluorescence, 637-850 nm). This investigation was achieved using a different set-up with only the fiber and the associated sensor head being used. The purpose of these investigations was to determine if any chromatic aberrations would affect the excitation on the NV ensemble or collection of NV fluorescence. The other purpose was to determine the excitation volume of the diamond and determine if improvements are needed to the microwave excitation system.

Two laser sources were used for this investigation: a 532 nm laser (Crysta-Laser CL532-100-S) and a 635 nm wavelength diode laser with a maximum power output of 1 mW. The two beams were combined through using a 2-by-1 fiber splitter (the fibers were 50 μ m multimode). This single fiber is then coupled, using a 2.5 mm bronze split mating sleeve (Thorlabs ADAF4) to the multimode fiber (Thorlabs FG400AEA-Custom) that we use for magnetometry. This fiber then maintains the same sensor head configuration with the pair of aspheric lenses that are housed in the zoom house. The antenna is removed and is instead replaced with a 10 \times 10 mm 220 grit ground glass diffuser of 1.6 mm thickness (Edmund Optics 62-615). This ground glass diffuser itself is mounted onto an externally threaded SM1 holder. The ground glass diffuser is used to minimize the power intensity to prevent damage to the pixels of the CMOS camera. A 6.35 mm diameter A-coated Steinheil achromatic triplet with a focal length of $f = 10$ mm (Thorlabs TRS064-010-A) is used to focus the output onto a color CMOS camera (Thorlabs CS165CU/M). From this it was found that the intensity profiles of the red and green were overlapping in the x and y directions but chromatic aberration is in z. The chromatic aberration would result in a reduction in either the amount of optical power used for excitation or the fluorescence collection from the diamond.

4.3.4 Microwave Antenna Choice

Investigations into the beam waist of excitation were also undertaken using the same setup as 4.3.3, this was to determine if a modification of the microwave antenna was needed to excite the NV center ensemble more efficiently. If the excitation volume is large, it is expected that using a microwave wire as the antenna would limit the

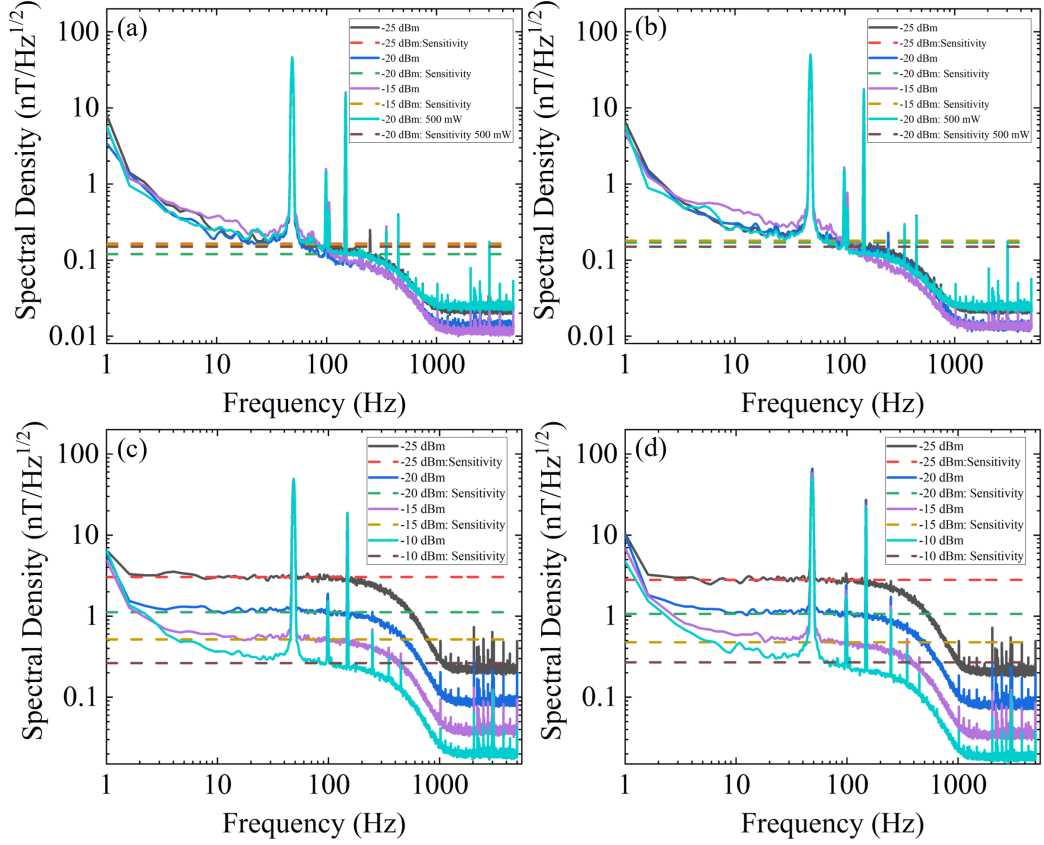


Figure 4.3: For the following sensitivity measurements the bias field was aligned along (100), and the sensitivity taken for both NV center resonances; the left-hand side (LHS) resonance frequency is 2846.4 MHz while for the right-hand side (RHS) the resonance frequency was 2883.55 MHz. The mean sensitivity is the mean between the frequency range 10-200 Hz. (a) The loop LHS resonance, (b) the loop RHS resonance, (c) the wire LHS resonance and (d) the wire RHS resonance.

sensitivity as the microwave field generated by the wire has a sharp fall off with the distance from the wire: the microwave field is highly inhomogeneous. To determine the beam waist the microwave antenna was removed and replaced with a CMOS camera to image the beam waist of excitation, using this set-up it was estimated that the beam waist was $38.7\text{ }\mu\text{m}$. With such a beam waist it is expected that the height of excitation would be $600\text{ }\mu\text{m}$ which is the thickness of the diamond.

A comparison was also made between two different microwave antennae, the first was a simple microwave wire. It is expected that the microwave wire provides a strong microwave field closest to the wire but with a sharp fall off with the distance from the wire [147; 146]. The other antenna was a loop of a diameter of 2 mm; the excitation beam was directed toward the center of the loop. The experimental configuration was the same for both microwave antennae with the same diamond being used. The only change was the microwave antenna. For all measurements the laser power was set to 1000 mW, the frequency sweep range was 2.78-2.94 GHz, with a step dwell time of 4 ms, the number of points were 8,001 giving a frequency spacing of 20 kHz between points while the frequency deviation and modulation were respectively set to 600 kHz and 3.0307 kHz respectively. The LIA low pass filter frequency was set to 300.8 Hz. The LIA output scaling was 28 when the wire antenna was used while it was reduced to 14 for the loop antenna. The magnetic bias field for all measurements were taken using a (100) bias field alignment.

As shown in figure 4.3 there is a reduction in the sensitivity when the microwave wire is used, with a difference of ~ 2.2 being achieved in the sensitivity when comparing the best sensitivity values for the wire and loop antenna, see table 4.1. The low frequency noise, i.e. the $1/f$ noise, is primarily attributed to magnetic noise originating from the environment whilst the 50 Hz and harmonics thereof are attributed to magnetic noise from the mains power source. For lower microwave powers the microwave wire provides a greater discrepancy in the obtained sensitivity; it is believed that this is due to the poor excitation of NV centers furthest from the wire. At higher microwave powers these NV centers now contribute to the magnetic resonance signal. For all given microwave powers the loop provides a higher sensitivity than the microwave wire. It is further believed that using a microwave loop with a larger radius may also improve the homogeneity and therefore further improve the sensitivity. It is for this reason that the microwave wire was abandoned in favor of using the microwave loop. Upon utilizing a microwave loop the sensitivity of the magnetometer was consistently sub-nanotesla. Further improvements may be gained through the use of a microwave resonator which can provide an even more homogeneous microwave field though this will limit the usable frequency range of

Wire vs. Loop Antenna						
dBm	LHS wire	LHS loop	Diff.	RHS wire	RHS loop	Diff.
-25	3.0 ± 0.5	0.16 ± 0.5	18.8	2.8 ± 0.1	0.18 ± 0.08	15.5
-20	1.12 ± 0.07	0.12 ± 0.02	9.3	1.07 ± 0.05	0.17 ± 0.09	6.3
-15	0.52 ± 0.03	0.16 ± 0.02	3.25	0.48 ± 0.04	0.18 ± 0.04	2.7
-10	0.26 ± 0.02	-	N/A	0.27 ± 0.03	-	N/A
-20	-	0.15 ± 0.02	N/A	-	0.15 ± 0.02	N/A

Table 4.1: The sensitivity values obtained from the wire vs loop antenna comparison study. The microwave power values are listed as dBm but this is the value prior to amplification; the microwave output is amplified by 43 dB and this is the microwave power delivered to the antenna. All specified sensitivity values are in units of $\text{nT}\sqrt{\text{Hz}}$ and are the mean of 160 FFTs, the errors quoted are the standard deviation of the 160 FFTs. The abbreviations LHS and RHS are left-hand side and right-hand side respectively. For the last row of the table the microwave power was set -20 dBm (value prior to amplification) while the laser power was reduced to 500 mW, this measurement was only taken for the loop antenna.

the magnetometer.

4.3.5 Optically Detected Magnetic Resonance Spectra

An ODMR spectrum of the NV center when aligned along (111) is shown in figure 4.4(a), hyperfine excitation is employed to enhance the contrast. As the bias field is aligned along only one of the four NV center orientations only a quarter contribute to the magnetometry measurements; the other NV center resonances are degenerate and thus occur at the same frequency. The microwaves are swept across the frequency range of 2.78 GHz to 2.94 GHz, with a step resolution of 20 kHz, a step dwell time of 4 ms and a LIA frequency bandwidth of 200 Hz using a 48 dB/octave filter slope; the LIA output scaling was set to $\times 500$. For all sensitivity measurements the NV center resonance occurring at a frequency of ~ 2.81 GHz was used.

It is inferred from equation 2.24 that the shot-noise limited sensitivity is improved by increasing the contrast/linewidth ($C_{CW}/\Delta\nu$) ratio. The contrast can be increased by increasing the delivered microwave power however there is a trade-off as an increasing microwave power will also cause the ODMR linewidth to increase. To maximize the magnetometer sensitivity and determine the relation of the LIA output to the microwave delivery parameters, specifically the microwave power, modulation frequency and frequency modulation amplitude a series of ODMR spectra were taken. The microwave intensity is not equal for the three frequencies used to excite the three hyperfine lines. This was confirmed when the microwave output after mixing was connected to a vector network analyzer (Agilent N9320B). The result of this means

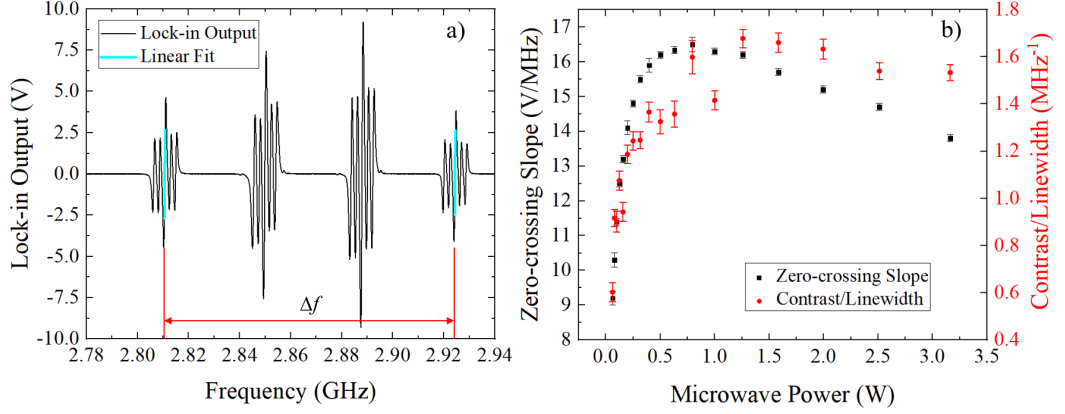


Figure 4.4: (a) An ODMR spectrum of the NVC as a function of varying microwave frequency. (b) The zero-crossing slope and the contrast-to-linewidth ratio as a function of applied microwave power after amplification and neglecting cable losses. All measurements were taken using a frequency modulation amplitude of 300 kHz and a modulation frequency of 3.0307 kHz.

that the linewidth of an ODMR resonance depends on which microwave excitation(s) created it. This is taken into account during the fitting procedure where each NV center resonance is fitted independently of each other.

The microwave power was varied from -25 dBm to -8 dBm (pre-amplification value before the 43 dB amplifier, corresponding to 0.06 W and 3.16 W respectively after amplification with losses due to the cables neglected); the variations in power were in 1 dBm increments. For a given microwave power, spectra prior to LIA amplification were taken to determine the contrast and the linewidth while an LIA spectrum was taken to determine the zero crossing slope (the gradient of the NV center ODMR spectrum); all spectra were taken when exciting all three nitrogen-14 hyperfine resonances. The value of the zero-crossing slope is highly correlated with that of the contrast-to-linewidth ratio. It is inferred that the highest sensitivity is achieved for a microwave power of 0.8 W; this is inferred from the maximum of the zero crossing slope. The effects of varying the frequency modulation and frequency modulation amplitude were also investigated at the microwave power of 0.8 W, the frequency modulation was varied between 1 to 80 kHz while the frequency modulation amplitude was varied from 100 to 600 kHz.

The microwave power, the frequency modulation and the frequency modulation amplitude were varied and the ZCS determined for each change. It was found that the maximum value of the ZCS occurred at a microwave power of ~ 0.8 W, see figure 4.4b). Figure 4.5(a) shows that the ZCS is maximized at a modulation

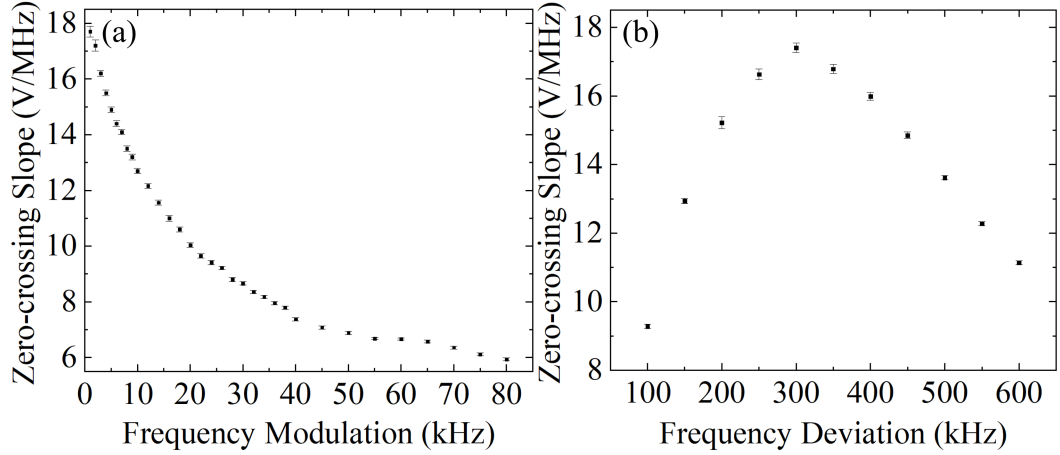


Figure 4.5: The zero-crossing slope as a function of the modulation frequency.

frequency of 1.0307 kHz while figure 4.5(b) the modulation frequency amplitude is maximized at 300 kHz. For lower frequencies the ZCS could be increased but the magnetometer sensitivity was worse due to failing to reject low-frequency noise with the LIA. This $1/f$ noise is worse at low frequencies.

4.3.6 Zero-crossing Slope vs. Modulation frequency

To determine the optimum modulation frequency to maximize the sensitivity, ODMR spectra as a function of the modulation frequency were taken, see figure 4.5. It is expected that using higher modulation frequencies will reduce the value of the zero-crossing slope as the NV center contrast will be reduced due to the finite repolarisation time [81; 251; 252]. Though the expected trend is followed (the value of the zero-crossing slope increases with lower modulation frequencies), the best sensitivity is achieved at a modulation frequency of 3.0307 kHz with a ZCS value of (16.2 ± 0.1) V/MHz; further optimization allowed the maximum value of the zero-crossing slope to become (17.9 ± 0.2) V/MHz for a modulation frequency of 3.0307 kHz, using this value of the ZCS the calibration constant is 5×10^{-4} V/nT when using the gyromagnetic ratio, 28 Hz/nT, of the NV center; the sensitivity is found to be 171 pT/ $\sqrt{\text{Hz}}$. It is believed that the superior sensitivity at a higher modulation frequency was due to the increased susceptibility to lower noise frequency components that are typically common as one approached low modulation frequencies nearer to DC.

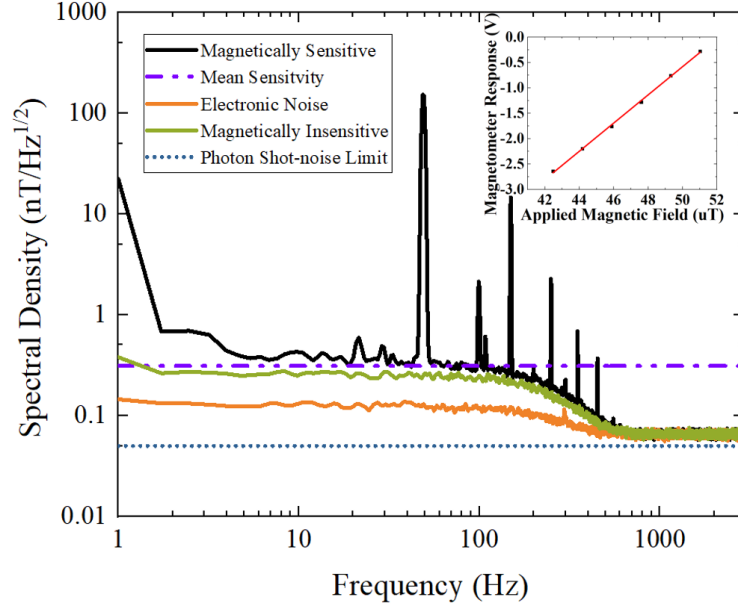


Figure 4.6: Diamond magnetometry sensitivity spectrum: the mean sensitivity is $310 \text{ pT}/\sqrt{\text{Hz}}$ from 10-150 Hz. The noise floor is shown when no longer on a resonant frequency (magnetically insensitive) and with no applied laser or microwaves (electronic noise). The on resonance, off resonance and electronic noise are the mean of 160 1s FFT's. Inset is a figure that demonstrates the magnetometer responsivity for a given applied test field. This calibration was used to determine the sensitivity.

4.3.7 Test Field Calibration

Another method to determine the sensitivity of a magnetometer is through the application of known test fields to determine the response (voltage change) of the magnetometer due to a changing magnetic field, the fields can be either AC or DC and examples of using both have been found in literature to characterize a diamond magnetometer. This was achieved by applying known test fields using a homemade Helmholtz coil; the current was supplied by a bench top power supply (Tenma 72-10480). This Helmholtz coil was placed around the sensor head with the diamond being placed directly at the center when used to determine the magnetometer response. The Helmholtz coil itself was calibrated using a Hirst Magnetics GM07 Hall probe which allowed the current and induced magnetic field relation to be determined. The test fields were applied along the (100) orientation and from this it was determined that the magnetometer responsivity/calibration constant was $2.77 \times 10^{-4} \text{ V/nT}$; this was calculated by applying a linear fit to the data inset in figure 4.6. It is determined that the sensitivity with this calibration is $(310 \pm 20) \text{ pT}/\sqrt{\text{Hz}}$ as shown in figure 4.6. The low frequency noise, i.e. the $1/f$

noise, disappears when the microwave frequency is off resonance (see magnetically insensitive line in figure 4.6 showing that the noise is magnetic in origin. The difference in values between the magnetically sensitive and insensitive spectral densities suggests that there are background magnetic fields that are a source of noise. All FFT traces shown in figure 4.6 are the result of the mean of 160 FFTs (the error given for the mean sensitivity is the standard deviation of 160 FFTs); all FFTs were performed using the inbuilt capabilities of the Picoscope 5000 oscilloscope. The noise present, the $1/f$ and the 50 Hz and its harmonics are confirmed to be magnetic in origin as it does not appear in the magnetically insensitive (off-resonance) FFT. The discrepancy in the obtained sensitivity between the two calibration methods is due to the non-optimal test field orientation. The test magnetic fields are applied along the (100) orientation and hence a reduction in the responsivity by a factor of $\cos(109.5/2) \sim 0.57$ is expected; we obtain a difference of 0.55 between the two values.

The photon-shot noise limit was calculated using equation 2.24 and found to be $50 \text{ pT}/\sqrt{\text{Hz}}$ using the values of 1.11 MHz for the linewidth, a contrast of 1.76% and a photon collection rate of 1.2×10^{15} photons/s. The contrast and linewidth were directly extracted by Lorentzian fits to the ODMR resonance features prior to lock-in amplification when exciting all three nitrogen-14 hyperfine resonances. The fluorescence was determined by measuring the incident power level prior to the balanced detector using a power meter (Thorlabs PM100D equipped with a power meter head Thorlabs S121C). It is believed that the majority of the noise that prevents the magnetometer from reaching the photon-shot-noise-limit is due to uncanceled laser and magnetic noise. It should be possible to reduce the factor away from shot noise through the implementation of a gradiometer which could cancel any common mode noise.

4.3.8 Sensor Head

Aluminum was chosen as the substrate of choice for the microwave delivery antenna due to its higher thermal conductivity when compared to a material like FR4. Superior sensitivity values were obtained when using the FR4 substrate however the thermal properties were significantly worse and at high enough laser powers there was significant risk of damage to the FR4 antenna boards; at high intensities the FR4 boards would burn and thus high intensity laser power could not be used. The higher thermal conductivity helps to remove heat from the diamond which helps mitigate thermal fluctuations of the diamond; changes to the diamond temperature will cause a shift in the position of the NV center resonance. The temperature of

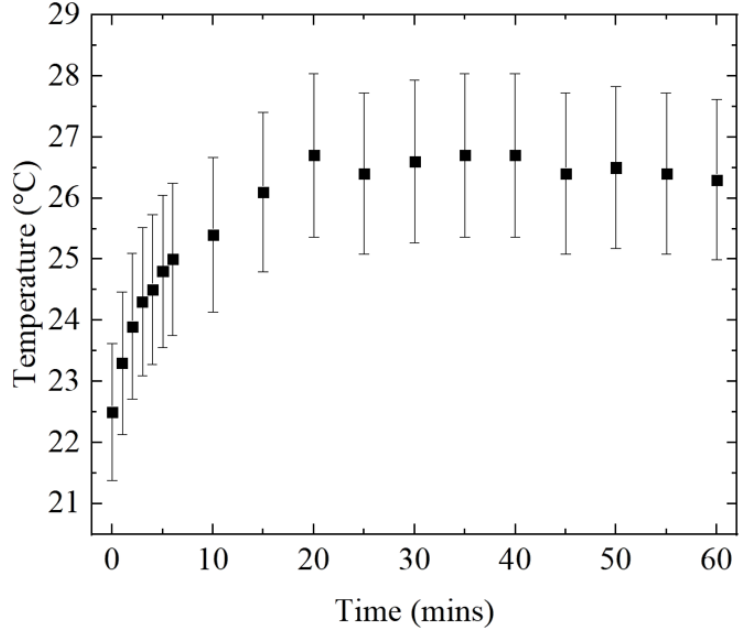


Figure 4.7: Temperature variation of the aluminum antenna as a function of time for 60 minutes.

the aluminum antenna was monitored for one hour after the laser power was set to 1 W, the results are shown in figure 4.7. All temperature recordings were made using a Fluke TiS PRO infrared camera with all errors in the temperature measurements taken as 5% of the temperature reading recorded by the thermal camera. An equilibrium temperature of ~ 26.5 °C was reached after 20 minutes making it safe to come into contact with living tissue. Ideally for cardiac sensing the procedure would be non-contact but a stronger signal will be obtained if the magnetometer is directly touching the chest as it will be closer to the heart. A picture of the sensor head with the magnetic bias field is shown in figure 4.8.

4.3.9 Laser Noise

To develop a magnetometer that was fully portable all optical components and associated electronics were placed in a rack mount set-up with a fiber and microwave cable allowing for a portable sensor head that was relatively detached from the control instrumentation. To maintain the laser temperature in its thermally stable operating region the laser head is placed on a large aluminum block which in turn is connected to heat fins to remove heat from the laser. However, due to the minimal space in the rack the size of the heat sink is limited. When operating the laser at full power (2 W of power) the laser head generates more heat than at 1 W.

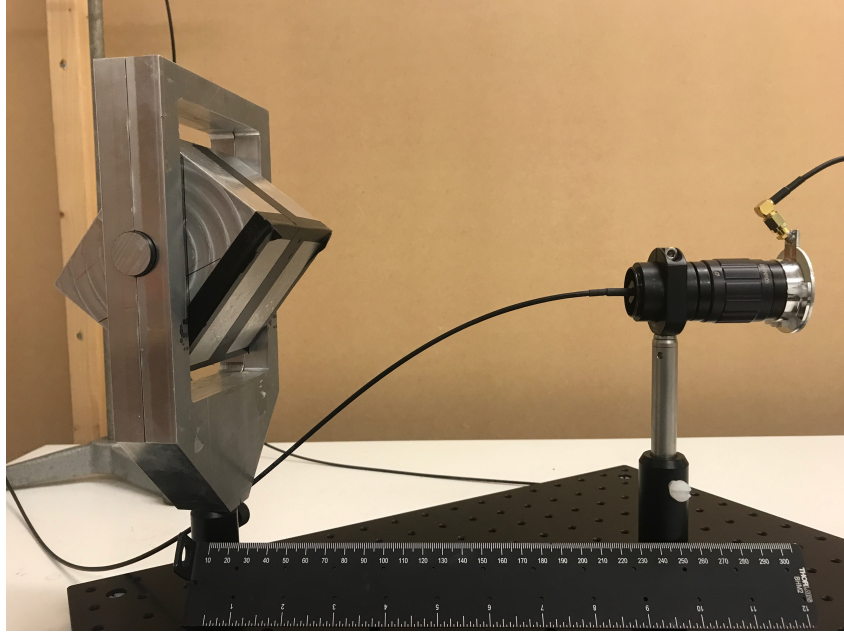


Figure 4.8: A picture of the sensor head (black horizontal cylinder in the top right). On the left is a NdFeB bias magnet in a rotatable aluminum enclosure. A ruler is included to show the scale size.

The noise on the magnetometry measurements was more significant at 2 W than at 1 W, which significantly degraded the sensitivity. As mentioned previously it was hypothesized that the laser head reached a temperature that was on the cusp of different modes and so the laser was oscillating between these different modes which introduced noise through mode hopping. The temperature can be stabilized through introducing other heat management solutions such as forced air cooling plates however passive solutions to heat management are preferred as it was found that fans introduced sporadic noise. To operate in a thermally stable regime we chose to use 1 W of laser power. An image of the sensor head is shown in figure 4.8.

4.3.10 (111) Orientation vs. (100) Orientation

As there are four orientations for the NV center when using an ensemble and we only use a quarter when aligned along (111) the other three orientations do not contribute to the magnetometry signal. By aligning to a (100) orientation the magnetic field projection along all four orientations is the same, this enhances the spin contrast by a factor of four. However, as the bias field is no longer preferentially aligned to any NV center axis the gyromagnetic ratio is reduced and thus each orientation's sensitivity is reduced by a factor of $\cos(109.5/2) \sim 0.57$; the expected enhancement

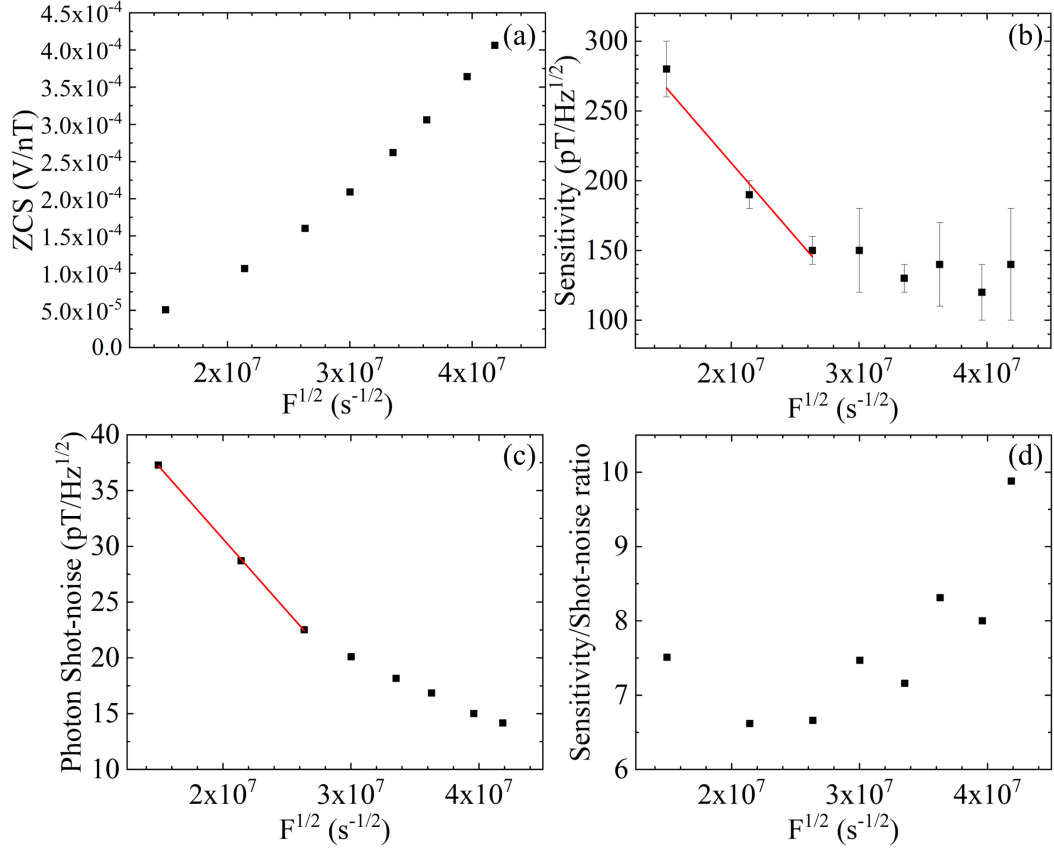


Figure 4.9: (a) The zero crossing-slope (ZCS) is plotted as a function of the square root of the NV center photoluminescence (PL), F . (b), (c) and (d) are respectively the sensitivity, the photon-shot-noise limit and the sensitivity-to-shot-noise ratio all are plotted as a function of the square-root of the PL.

to the sensitivity is thus expected to be $4 \cos(109.5/2) = 2\sqrt{4/3} \sim 2.3$.

4.3.11 Shot-noise limit scaling as a function of PL

To investigate the factors limiting the sensitivity of the magnetometer a mounted continuously variable neutral density filter (Thorlabs NDC-59C-2M-A) was used to decrease the incident NV center fluorescence on the signal photodiode. This was to investigate how the magnetometer sensitivity scales with the NV center photon flux rate; in all such measurements the incident photon flux rate on the reference arm (laser output) of the balanced detector was matched to the incident NV center fluorescence, it is expected that the calculated shot-noise would similarly scale in the same manner. All other experimental parameters such as the microwave power or modulation parameters were unchanged, the bias magnetic field was aligned along

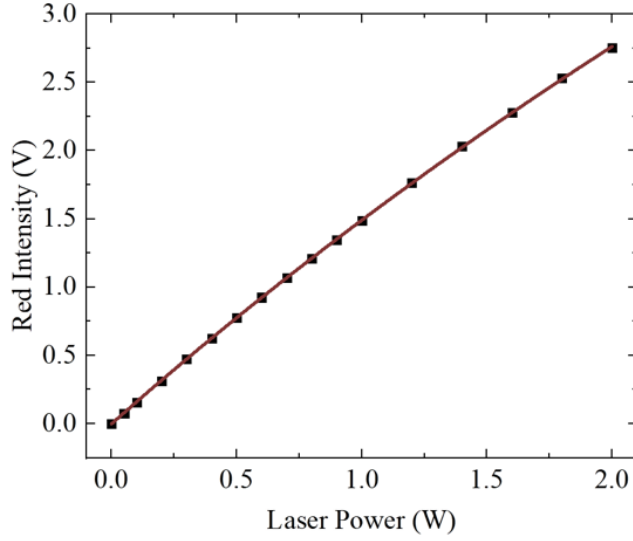


Figure 4.10: A power saturation curve plotting the applied laser power against the photodiode output from the balanced detector.

(100); the aluminum antenna was replaced with a SiC antenna (see chapter 6 for further details). It is expected, due to equation 2.24, that the magnetometer sensitivity would scale linearly with the square root of the NV center fluorescence. As a control the relationship between the supplied laser power and magnetometer sensitivity was also investigated. It is expected that the sensitivity will not scale linearly with the laser power as the rate of spin polarization will be varied. It was found that the expected relation of linear scaling was followed for both the sensitivity and the photon shot-noise limit at low NV fluorescence values, see figure 4.9(b) and (c). However at higher fluorescence values it was found that the expected trend was not followed and that the sensitivity appears to reach a limit at higher fluorescence values regardless of the increase in the incident fluorescence; the improvement in the sensitivity is minimal when compared to the increased fluorescence. It is also found that the increase in the value of the ZCS scales in a similar manner. This suggests that the sensitivity of the magnetometer itself is limited with a possible limitation to the sensitivity being due to either the background environmental noise or a limitation due to the equipment used. The best sensitivity value for the magnetometer was $(120 \pm 20) \text{ pT}/\sqrt{\text{Hz}}$ in the frequency range of 10-200 Hz. The ratio of the sensitivity to the photon-shot-noise limit was calculated for all sensitivities for a given PL level, as the PL level increases the ratio also increased.

To determine the regime and whether the NV centers are power saturated, a power saturation measurement was taken with the results shown in figure 4.10,

the data was fit according to equation 2.26 and it was determined that P_{sat} is (11.6 ± 0.3) W and F_{∞} is (18.8 ± 0.4) V. The regime of operation is far from saturation of the NV center defects. In a CW magnetometry scheme if the NV centers are in an optically saturated regime it would limit the magnetometer sensitivity and thus one would wish to be far from this regime to prevent the sensitivity from being limited.

4.4 Future Goals

The aim of the magnetometer system that was developed and characterized in this chapter was to produce a system that would be portable enough to be useful in a wide range of applications but still have a comparable sensitivity to diamond magnetometers that are fixed to optical tables. The main focus for this magnetometer was to perform unshielded MCG measurements. The high portability would also allow it be useful in a range of applications beyond that of a medical diagnostic tool. Depending on the distance of the sensor from the heart, the peak of a cardiac magnetic field signal can be as high as 100 pT while smaller features associated with the magnetic field signal given by the heart can be as low as 5 pT [253]. The frequency range typically of MCG signals are typically in the range of 0.1-100 Hz and are produced by electrical currents in the heart. The current sensitivity achieved by the magnetometer in this work when fully optimized is (120 ± 20) pT/ $\sqrt{\text{Hz}}$ in the frequency range of 10-200 Hz, with the main improvement over the published value of (310 ± 20) pT/ $\sqrt{\text{Hz}}$ in the frequency range of 10-150 Hz arising due to the (100) alignment and further optimization to the experimental parameters. However, this is still not sufficient to be able to detect cardiac magnetic fields.

Currently, it is believed that the greatest limitation of the magnetometer is the poor collection efficiency; the conversion of the green to red photons is calculated to be $\sim 0.06\%$ and significant improvements to the sensitivity are expected if the excitation and collection efficiency can be improved. This was calculated by dividing the NV center fluorescence power by the total laser power output (1000 mW). Published works have been able to achieve values as high as 8% [165], which would represent an improvement by a factor of 12 to the sensitivity of our fiber-coupled magnetometer, assuming a shot-noise limit scaling with the fluorescence. However, it has also been demonstrated that the sensitivity of the magnetometer appears to reach a limit as the sensitivity is capped at 120 pT/ $\sqrt{\text{Hz}}$. The sensitivity does not improve with the photon collection rate when approaching sensitivities as high as 120 pT/ $\sqrt{\text{Hz}}$ irrespective of the improvement to the photon collection rate. This suggests that even

with a better collection efficiency the magnetometer system is still limited by other factors. Some of the noise has been attributed to uncanceled laser and microwave noise. Furthermore, it is likely that there is environmental background magnetic noise that could also be a limiting factor. As some of the background magnetic fields can be orders of magnitude stronger than the magnetic field signals from the heart these signals would have to be suppressed to perform unshielded MCG. This cancellation is possible when using a magnetic gradiometer as this will be able to cancel out common-mode noise. Gradiometer systems have already been developed with other magnetometer systems and have been able to detect signals from the heart and the brain. Gradiometer systems have also been employed using the NV center in diamond in both a fiber-coupled and non-fiber coupled configuration [244]. If the noise that limits the sensitivity of the magnetometer is indeed due to either environmental noise or due to uncanceled laser noise it should be possible to reduce this noise through a gradiometer. Preliminary progress toward this is discussed in chapter 6.

Chapter 5

Imaging Damage in Steel Using a Diamond Magnetometer

Non-destructive methods of being able to inspect the quality of an object is highly useful for industrial applications due to being able to assess any damage to materials such as steel without needing to apply any further modification to the material under inspection [88]. This can save time and resources and as such having the ability to analyze materials through using non-destructive testing (NDT) is of vital importance to industry.

This chapter concerns the development and usage of a new NDT technique in which damage to a ferromagnetic material distorts an applied magnetic field. The fiber-coupled diamond magnetometer from the previous chapter was used to detect this distortion. To achieve a high spatial resolution, a small magnet was introduced very close to the diamond as explained below. The other NDT method that was investigated was the alternating field current method, this technique can be used to analyze any conductive material and works by applying low frequency currents to a conductive material. The aim was to develop a technique that would utilize the advantages of a diamond magnetometer, with a radiation-hard sensor head for use in the nuclear power generation industry.

5.1 Introduction

Globally corrosion in materials such as stainless steel is a huge problem which is responsible for economic loss estimated as being over \$100 billion per year. To mitigate such losses there are many NDTs used in industry with each method having particular advantages and disadvantages [254; 255; 256; 257; 258; 259; 260; 261; 262];

this section will briefly summarize the most commonly used methods in industry.

5.1.1 Visual Inspection

This method is technically the simplest as it involves using a human eye to look for any damage through optical means, all investigations are therefore performed using light in the visible range. This method has intrinsic issues as it is limited only to surface damage and involves the use of individuals who are error prone. To be utilized in an effective manner an individual would have to be trained and have significant experience. It is also not possible to send a person into many of the situations where NDT analysis is needed.

5.1.2 Magnetic Flux Leakage

There are several magnetic methods among which the most common is the magnetic flux leakage method. This method allows for the analysis of ferromagnetic materials through applying strong magnetic fields to saturate the material in question [88; 263; 264; 265; 266; 267; 268; 269; 270]. In the absence of any damage the magnetic flux mostly stays in the material. However, in the presence of damage such as a crack the flux leaks out of the material [88]. This leakage can be detected by a magnetometer which can allow for the identification of damage. However, the material under inspection must ideally be saturated which can require very strong magnetic fields; on the order of one Tesla which can be hard to achieve in practical settings. As the material requires saturation this can only be used to analyze ferromagnetic materials [88; 261; 262].

This technique is mostly used by the oil and gas industry to investigate damage in pipelines without the need to undergo costly excavations, typically a large array of sensors are combined and placed into a tool that travels in the pipeline; such a tool is called a pipeline inspection gauge [266; 267; 268]. The pipeline inspection gauge is designed to travel through a pipeline with the sensors placed on the outside so that it is close to the pipeline wall. Combined with accurate global positioning system measurements the damage can be detected and localized.

5.1.3 Ultrasonic Inspection

Ultrasonic testing involves the use ultrasonic waves which are sent through a material. Information is gained by measuring the reflections which come back to the ultrasound transducer due to damage and material interfaces. This can yield information about the materials properties and allow damage to be identified [271].

5.1.4 Eddy Current Testing

Eddy current imaging allows for the inspection of any conductive material and thus can be extended to non-magnetic materials such as aluminum [82]. A time-varying magnetic field is applied to a material and due to the law of magnetic induction any free electrons in the material will form eddy currents. The strength of the induced eddy current is highly dependent on the conductivity of the material and the strength of the time varying magnetic field. From this it is even possible to distinguish between different materials based upon their conductivity. In the vicinity of damage in the material the induced signal will be different, this is due to the differing conductivity; there will be a significant decrease in the amplitude of the induced signal and a change in the phase [82].

5.2 Magnetic Flux Distortion

The key method that allowed for the detection of damage in ferromagnetic materials presented here was the introduction of a small 1 mm^3 magnet at a distance of approximately 5 mm away from the microwave excitation loop where the diamond is located. As the NV center utilizes Zeeman shifts to perform magnetometry and the magnetic flux line of the magnet would be distorted upon coming near the vicinity of significant change in the magnetic permeability, the magnetic profile of the magnet will change which in turn will shift the resonant frequency of the NV center. Furthermore, the introduction of a small magnet creates a very inhomogeneous magnetic field upon the diamond which allowed the dynamic range of the magnetometry experiments to be extended. As was mentioned in chapter 2 the dynamic range was defined as the range over which the magnetometer can sense magnetic fields and for an NV center magnetometer will be defined as the extent of the linear region of the lock-in amplifier derivative signal. A larger linewidth corresponds to a greater range for the dynamic range. The inhomogeneous magnetic bias field meant that all NV centers will resonate at slightly different frequencies and thus the NV center resonance linewidth is larger and the spin contrast is reduced. This reduces the sensitivity of the magnetometer but allows the magnetometer to have a larger magnetic field sensing range. When using a single small bias field the field was too inhomogeneous and thus a second magnet was used to reduce the inhomogeneity at the diamond to allow the sensitivity to be enhanced, whilst still allowing magnetic flux to be injected into the material under inspection. The extent of broadening to the linewidth and the reduction in the sensitivity is quantified in later sections. For the magnetic flux distortion measurements taken, to further extend the dynamic

range the basis for all measurements was not at the zero crossing slope (steepest point of the LIA derivative signal) but at the furthest point away from the zero crossing slope that still remains within the linear region of the LIA output.

5.2.1 Dynamic Range

As the dynamic range is an important factor it merits further discussion. To ensure accurate measurements a high dynamic range is required to ensure that the large magnetic field fluctuations that occur when the magnet approaches damage in a ferromagnetic do not shift the frequency of an NV center such that the sensor is no longer resonant: sufficiently large magnet fields will induce shifts to the resonance frequency such that it is no longer possible to obtain any useful information regarding any changes in the magnetic material under inspection. This can be characterized as the dynamic range of the system and as was mentioned previously is the extent of the linear region of the lock-in amplifier derivative signal. It can be seen from equation 2.24 that a narrow linewidth will lead to a higher sensitivity but this in turn leads to a poor dynamic range. Having a sensor possess a high sensitivity is advantageous in providing a higher signal-to-noise ratio which in turn can allow the sensor to be further away from the material under investigation. Thus it is ideal to have a system with a high sensitivity and a high dynamic range; however as these directly contrast one another one would have to use a PID tracker that would track the NV resonance such that microwave frequency would always be adjusted whenever there is a change such that one is always magnetically sensitive [60]. This would allow one to use narrow NV resonance linewidths for high sensitivity whilst achieving a high dynamic range. For all measurements undertaken in this chapter concerning magnetic flux distortion a compromise was made between the sensitivity and the dynamic range. This compromise was achieved through the use of two magnets, the first was a small magnet placed near the diamond which introduced a highly inhomogeneous magnetic field upon the NV center ensemble; this magnet was used to inject flux into the ferromagnetic material under inspection. The second magnet was a larger magnet that was used to reduce the inhomogeneity of the magnet field on the NV center ensemble, this enhanced the sensitivity whilst still allowing a sufficient dynamic range. The magnets were configured such that the magnetic poles opposed one another with the diamond placed between them. The position of the second magnet was adjusted to optimize the trade-off between the sensitivity and the dynamic range. The degree of inhomogeneity is quantified in later sections.

5.3 Alternating Field Current Method

To extend the range of materials that can be investigated beyond ferromagnetic materials the induction of eddy currents in a conductive material was investigated; the alternating field current method is a subset of eddy current induction. The frequencies of excitation did not go beyond 150 Hz. As the induced signal is highly dependent on various material properties, specifically the electrical conductivity, if there is a loss of material the generated signal will change and distort around the structural irregularity. For the experiments undertaken in this work the signals were induced by using a pair of coils, each coil was arranged in a winding rectangular arrangement and these were placed on the edges of the sample along the direction of the 25 mm length of the damage. This led to the induction of eddy currents in the material under inspection which could be detected by the diamond magnetometer. Through this it was possible to reconstruct the profile of damage through measuring the magnetic fields induced in the material under inspection.

For AC signals the generated magnetic fields do not entirely penetrate into the interior of the material in question but have a penetration depth dependent on the frequency

$$\delta = \frac{1}{\sqrt{\pi f_{AC} \mu_r \sigma}}, \quad (5.1)$$

where δ is the penetration depth, f_{AC} is the frequency of the AC induced signals, μ_r is the magnetic permeability of the material and σ is the electrical conductivity of the material. If the frequency is increased the strength of the magnetic fields will be increased but the penetration depth will be reduced.

5.4 Experimental Details

The experimental methods and equipment are similar to those in section 4.3, see figure 5.1, the optics and the configuration of lenses in the sensor head are identical. The microwaves are also delivered by the Agilent microwave source (Agilent N5172B) and hyperfine excitation is also utilized through using a sinewave generator (RSPRO AFG21005). The diamond used in this system is mounted on a custom-made aluminum microwave antenna (C.I.F AAT10), the diameter of the excitation loop for this antenna was also 2 mm. To place a 1mm-cube magnet into the antenna a ~ 1 mm hole was drilled into the antenna at an angle of approximately 45° . This hole was placed 5 mm away from the center of the excitation loop. The 1mm-cube magnet that was inserted into a hole was a nickel-plated (Nd,Fe)B magnet (Supermagnete

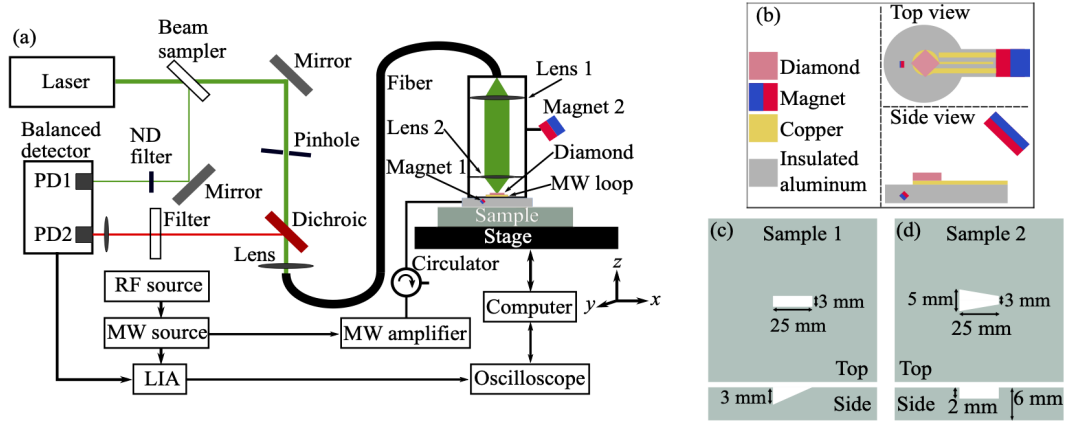


Figure 5.1: (a) A schematic of the experimental configuration, the neutral density (ND) filter, microwave (MW) and radio frequency (RF) sources, lock-in amplifier (LIA), and the two photodiodes (PDs) of the balanced detector are included. Magnet 1 is embedded into the aluminum (light grey rectangle) on which the microwave antenna is printed. (b) A schematic of the microwave antenna and the magnet configuration used to induce the Zeeman splitting (the blue and red colors are used to illustrate the differing magnetic poles). (c) and (d) are the 316 stainless steel plates (dimensions of 150 mm by 150 mm with a 6 mm thickness) used for these experiments: only a small area where the damage were introduced onto the plates are shown for clarity; the schematic dimensions are not to scale.

W-01-N). The second magnet had dimensions of 25 mm \times 25 mm \times 13 mm (Supermagnete Q-25-25-13-N) and was used to reduce the strength and inhomogeneity of the magnetic field of the 1mm-cube magnet that was closest to the diamond. Using only the single 1mm-cube magnet led to a highly inhomogeneous field which severely reduced the sensitivity of the magnetometer. The second larger magnet was placed further away (around ten cm away) and was used to mitigate the inhomogeneous magnetic field incident across the active sensing area of the diamond. The larger magnet was housed in a custom 3D-printed holder which was affixed to the sensor head. The custom holder enabled a 360° rotation of axes in two dimensions (those parallel to the x and y axes) and orientation control in the axis parallel to the z -axis allowing for arbitrary alignment of the magnetic field incident on the diamond. For completeness it is stated that other magnet combinations i.e. different magnet shape types and arrangements were also investigated. However, the results obtained from these configurations were far too inconsistent and thus in the end the configuration in figure 5.1 (b) was chosen.

The two test samples used are 316 stainless steel with different slot damage profiles, and the sample dimensions were 150 mm by 150 mm with a thickness

of 6 mm. 316 stainless steel is often described as non-magnetic but it is slightly ferromagnetic and is typically used by the nuclear industry. The two samples were sample 1 which contains a slot with a 3 mm width, a length of 25 mm and a gradient-depth from 0 to 3 mm along its length. In contrast, the other sample, sample 2, has a slot with a fixed depth of 3 mm along its length, a length of 25 mm, the width ranging from 3 to 5 mm along its length. The stainless steel samples themselves were mounted onto the bed of a scanning stage; the scanning stage allows the bed to move in two dimensions enabling two-dimensional scanning in the x and y axes. The sensor head is mounted onto the z -axis which allows different lift-off distances in the z -axis. The scanning stage itself was a 3D printer (Velleman K8200 3D printer kit) that was adapted to enable scanning; it was programmed using MATLAB. All data from the LIA output was sent to an oscilloscope (Tektronix DPO4104) which digitized the data.

It is possible to detect damage in ferromagnetic materials and map its profile as the NV center containing diamond can detect changes to the magnetic flux profile of the two magnets. When the magnetic properties of the material under study changes and comes near to the 1 mm cube magnet the magnetic flux profile of the two magnets will change. As the same magnets are used to induce Zeeman splitting on the NV center ensemble, any changes to a material can be mapped out. As the small magnet is the source of flux, the spatial resolution of imaging is directly correlated to the area that is magnetized. In addition, the spatial resolution is also determined by the volume of the diamond that is illuminated by the 532 nm laser. It is estimated that the beam waist of excitation is approximately 40 μm , with the excitation in the z -axis being 0.24 mm (the thickness of the diamond).

5.5 Diamond Properties

The diamond sample utilized in this work was a (100)-oriented HPHT sample supplied by Element Six; this sample was originally part of a larger diamond that

Diamond Defect Concentration					
Characterization Method	$[\text{N}_s^+]$	$[\text{N}_s^0]$	$[\text{NV}^-]$	$[\text{NV}^0]$	$[\text{NVH}^-]$
EPR	N/A	31 ppm	1.8 ppm	N/A	N/A
UV-Vis	N/A	N/A	4.3 ppm	0.4 ppm	N/A
FTIR	2.9 ppm	38 ppm	N/A	N/A	N/A

Table 5.1: The concentration of defects in the diamond sample used for steel scanning are listed.

was laser machined into 4 smaller pieces. The diamond sample dimension were $1.83 \text{ mm} \times 1.85 \text{ mm} \times 0.24 \text{ mm}$ and was chosen for this work due to its relatively low nitrogen concentration and the fact that it was not a ^{12}C -enriched diamond sample. The lack of ^{12}C -enrichment was so measurements could be made with with a larger dynamic range (larger NV resonance linewidth). To form NV centers whilst minimizing the presence of other unwanted defects the diamond was electron irradiated at room temperature with 2 MeV electrons at a dose of 10^{18} cm^{-2} in Japan by Shinobu Onoda. The sample was then annealed using a multistage process: 4 hours at $400 \text{ }^{\circ}\text{C}$, for 2 hours at $800 \text{ }^{\circ}\text{C}$ and 2 hours at $1200 \text{ }^{\circ}\text{C}$; at each step a 1 hour ramp was used between temperatures changes [223]. The diamond was then mechanically polished on all six sides to achieve an optical quality finish. The diamond was then cleaned to remove graphitic impurities under the following process: sulfuric acid (H_2SO_4) and potassium nitrate (KNO_3) solution for 60 min and then further cleaned for 20 minutes in H_2SO_4 . The concentrations of defects are given in table 5.1. These measurements were done with the aid of Dr. Ben Breeze at Warwick.

5.6 ODMR Spectrum Under Different Conditions

Figures 5.2(a) and 5.2(b) show ODMR spectra taken with and without a 316 stainless steel sample under the sensor head. Figures 5.2(c) and 5.2(d) show the ODMR spectra when the steel sample is under inspection with different lift-off distances; the lift-off distances were between a range of 1-4 mm and 1 mm increments were used. Figures 5.2(e) and 5.2(f) show the ODMR spectra when the sensor head was placed at different positions above the gradient-depth sample. To highlight the resonance shifts the outermost NVC resonance is shown in figures 5.2(b), (d) and (f), these correspond respectively to the dashed areas in figures 5.2(a), (c) and (e). As is expected, the NVC ODMR resonances shifted correspondingly to the magnetic flux profile changes over the NVC ensemble which were caused by changing magnetic properties near the sensor head.

5.7 Scan Data Profile

In figure 5.3, the 2D maps of the gradient-depth and gradient-width samples along with their cross-sectional profiles are shown. When considering only the extent of the LIA output percentage change differences in the profiles of the gradient-depth and gradient-width samples (see figure 5.3(b) and figure 5.3(e)), the differences in the depth are much clearer than the differences in the width. Lorentzian fits were

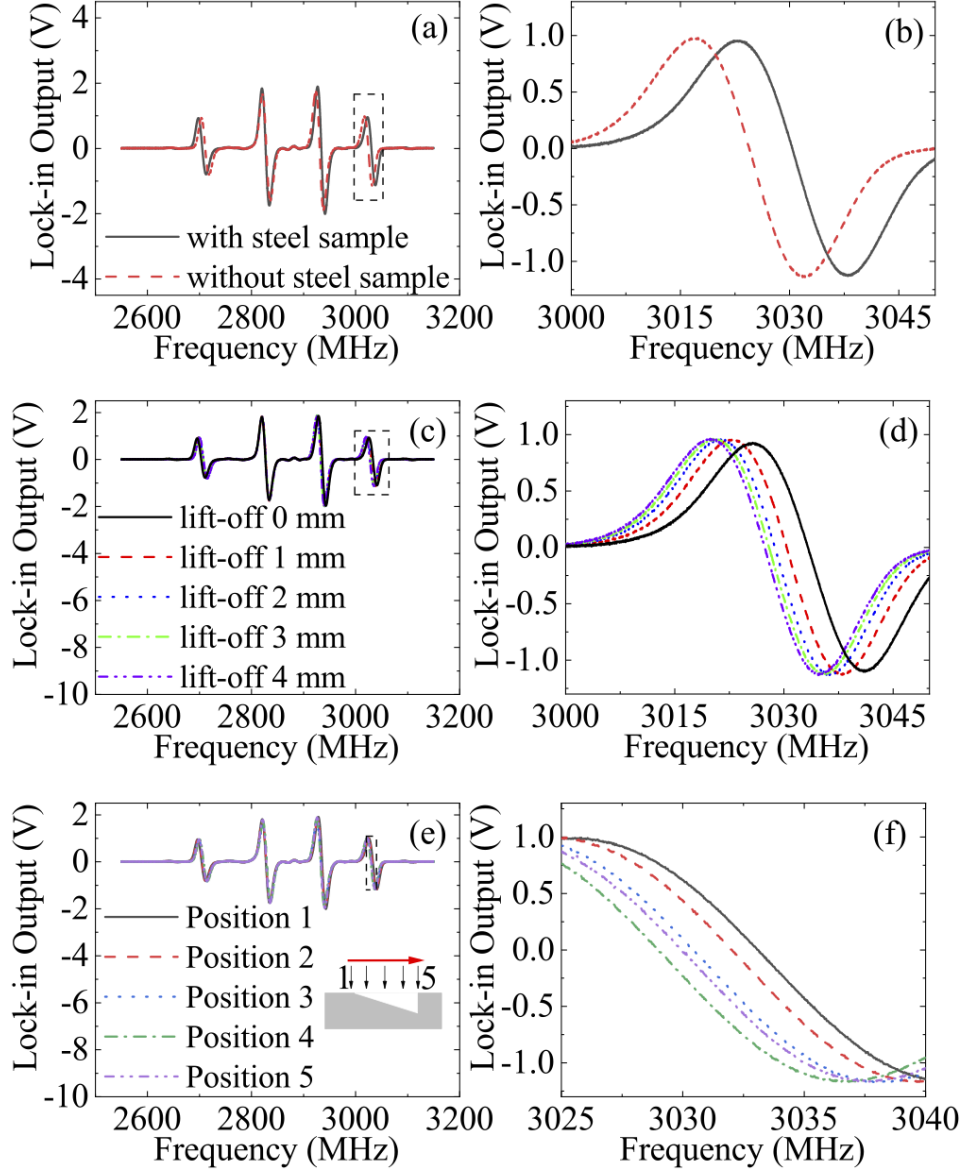


Figure 5.2: ODMR spectra under different conditions. (a) is taken with and without a 316 stainless steel sample. (c) are ODMR spectra with a lift-off from the stainless steel from a lift-off distance of 0 mm to 4 mm. (e) is for various positions along the length of the gradient-depth steel sample. (b), (d) and (f) correspond to the dashed regions in (a), (c) and (e) respectively, these are of the outermost right hand side NV center resonance.

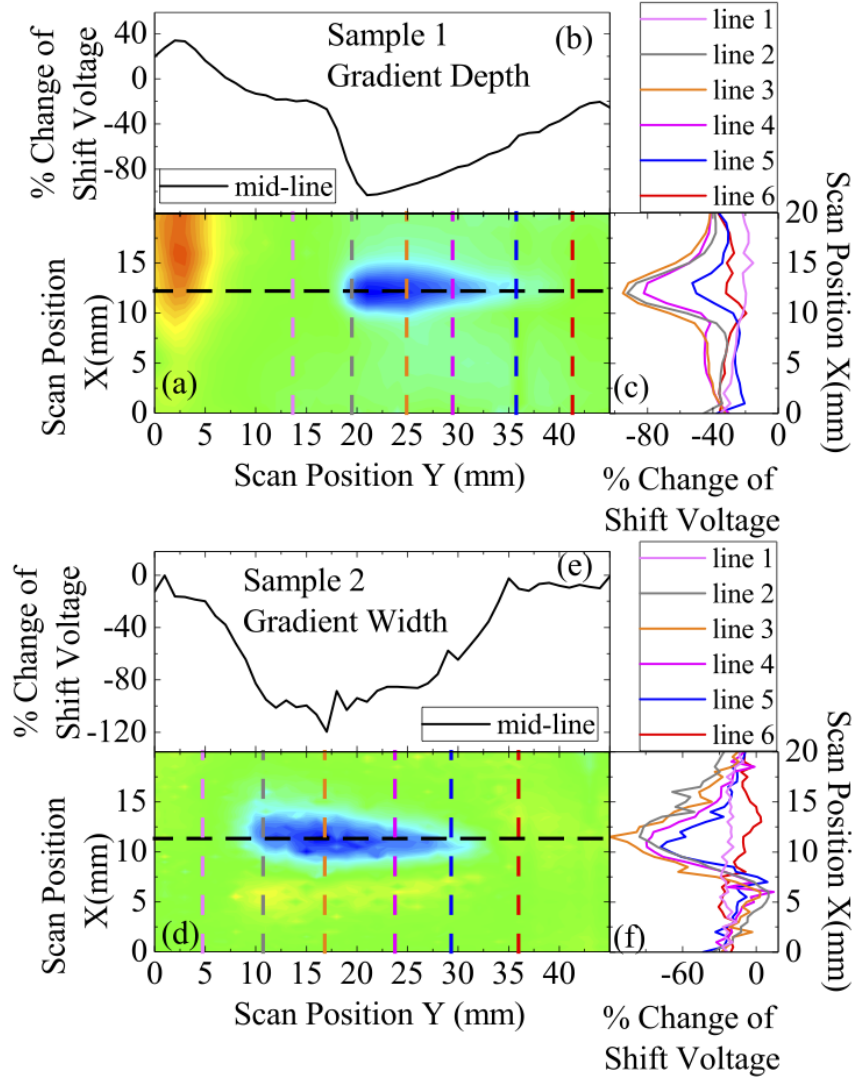


Figure 5.3: (a) and (d) are the 2D scans for the gradient-depth and gradient-width samples. (b) and (e) are the percentage changes that come out from the LIA output voltage for the black lines which are parallel to the y -axis, these correspond to the profiles for (a) and (d) respectively. The profiles in (c) and (f) are the LIA voltage output percentage changes, these correspond to the six lines which are parallel to the x -axis in (a) and (d); four of the six lines are taken along the damage area (lines 2-5), two are taken along areas where there is no damage (lines 1 and 6).

applied to highlight the differences even though the slot damage does not have this shape [272]. Though Lorentzian fits were used for the analysis of the cross-sectional profiles it was found that there was no difference obtained in the trends of the full width at half maximum or the amplitude if a Lorentzian or a Gaussian profile were used for the fits: for this reason only the Lorentzian profiles are shown.

It is expected for a sample where the depth changes but not the width that there will be a change to the magnitude of the LIA voltage output which will increase in proportion to the increase in the depth. However, as the width is unchanged it is expected that if one were to apply Lorentzian fits across the width of the damage there will not be a noticeable increase in the full width at half maximum (FWHM) yielded by the fits which should remain fairly constant. This is demonstrated by figure 5.3.

5.7.1 Magnetic Field Sensitivity

As was discussed in section 2.6, the sensitivity of an NV center magnetometer depends on the orientation of the applied bias magnetic field in relation to the NV center symmetry axis and upon the microwave delivery parameters, more specifically the microwave power, frequency modulation amplitude and modulation frequency. For this purpose the bias magnetic field was oriented along a $\langle 111 \rangle$ orientation. For all 316 stainless steel scanning measurements which involved the quantification of structural damage, the microwave parameters used were a microwave power of 10 W along with a frequency modulation amplitude of 4.5 MHz and a modulation frequency of 3.0307 kHz; the ODMR spectrum shown in figure 5.4(a) was taken using these parameters. The region highlighted in red at ~ 3 GHz is the region where all scanning measurements of the 316 stainless steel sample plates were performed. It should be noted that any value could have been chosen as the value for the microwave frequency provided it is along the linear region of the ODMR resonance. Indeed it is typical to use a value of 0 V: the zero crossing point as the basis for any measurements. However, to further extend the dynamic range a value of 0.6 V was chosen to make use of the larger dynamic range afforded by using the end of the NV resonance linear region rather than its central point. This was possible as all measurements made showed that the LIA voltage output would always shift in a single direction when mapping out the damage in 316 stainless steel: the voltage value would always change in a single direction which for these measurements was always a decrease. For this reason the reference frequency was chosen as the lowest value of the microwave frequency of the highlighted feature in figure 5.4(a). If a reference value of 0 V had been chosen instead, the dynamic range for any of the

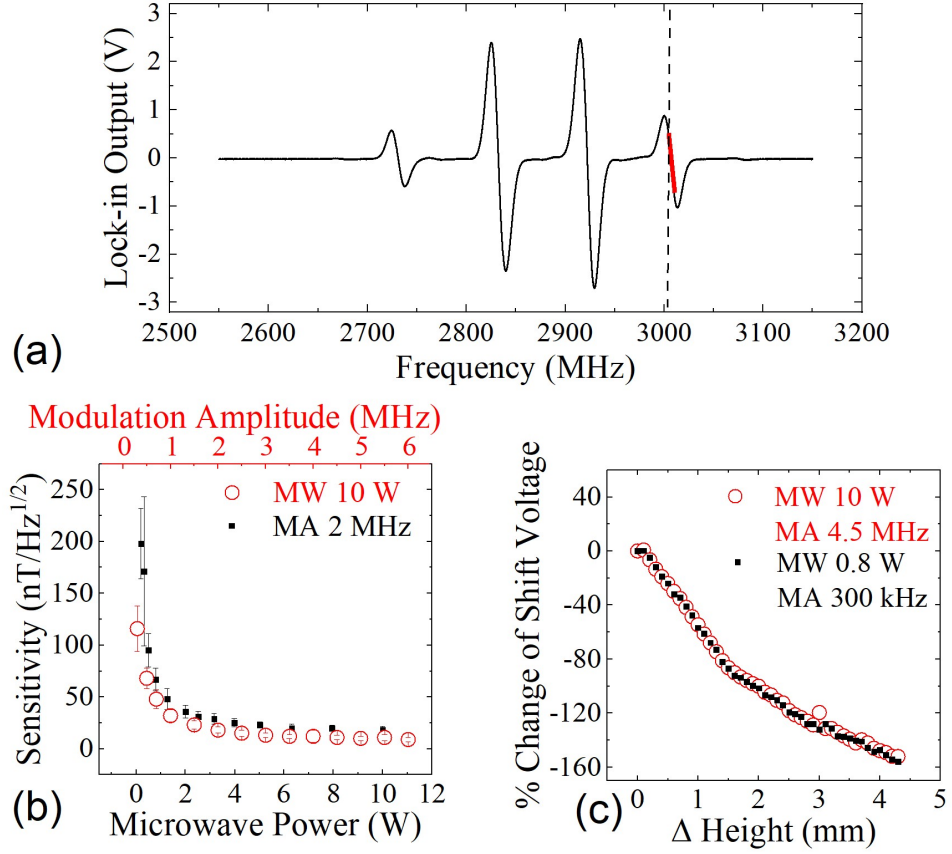


Figure 5.4: (a) The ODMR spectrum from the lock-in amplifier (LIA) output. The hyperfine splitting cannot be resolved as the magnetic field is highly inhomogeneous. (b) The dependence of the sensitivity on the input microwave power (black square) and the modulation amplitude (red circle), the abbreviations MW and MA are microwave and modulation amplitude respectively. (c) The changes to the LIA output voltage while monitoring a fixed microwave frequency when the lift-off distance between the sensor head and a damage-free 316 stainless steel sample is changed is shown. These measurements were taken under two different sensitivity conditions. The lowest sensitivity achieved for the microwave power of 0.8 W and a modulation amplitude of 300 kHz was chosen for the black circle, while microwave power of 10 W and a modulation amplitude of 4.5 MHz was chosen for the higher sensitivity situation. The lift-off from the aluminum to the steel is zero for $\Delta\text{Height} = 0$ mm.

mapping measurements made would be halved.

The experimental parameters used for all measurements were determined through varying the microwave power, between 0.2 W and 10 W, at a fixed frequency modulation amplitude and modulation frequency. In contrast, the optimum frequency modulation amplitude was found through varying it between 300 kHz and 6 MHz whilst fixing the microwave power and modulation frequency, see figure 5.4(b). In each parameter variation an ODMR spectrum was taken and linear fits applied to the outer (111) aligned resonance to determine the zero crossing slope; this was used to determine the sensitivity. The sensitivity was then established by taking 96 FFTs of the output voltage of the central point of the region highlighted in red and taking the mean value between 1-15 Hz; the errors associated with the sensitivity are the standard deviation of the 96 FFTs.

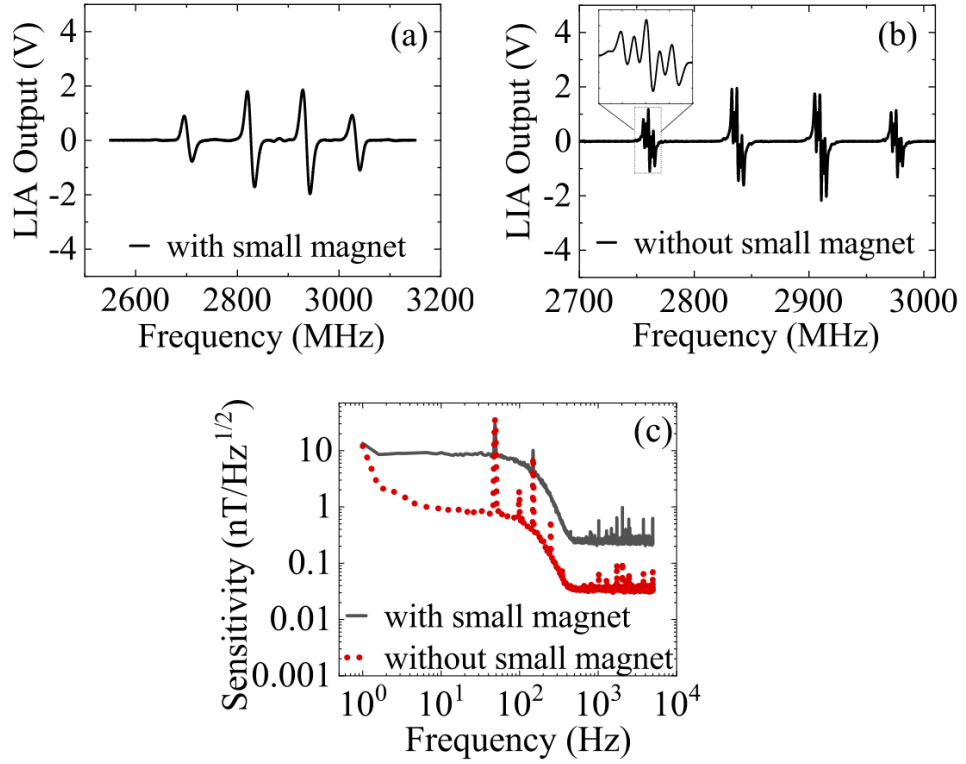


Figure 5.5: (a) ODMR spectrum using the Supermagnete W-01-N and Q-25-25-13-N magnets. (b) ODMR spectrum using only the Supermagnete Q-25-25-13-N. (c) Spectral density corresponding to the configurations in (a) and (b).

5.7.2 Inhomogeneous Field Sensitivity

The sensitivity of the magnetometer is provided for two cases, the two magnet configuration (using both the Supermagnete W-01-N and the Supermagnete Q-25-25-13-N) and a single magnet configuration (using only the Supermagnete Q-25-25-13-N). This was done to highlight the degradation to the sensitivity through using a highly inhomogeneous magnetic field. For these two cases, 160 FFTs were taken when monitoring the zero crossing of the ODMR resonance.

Figure 5.5(a) shows an ODMR derivative spectrum when using the dual magnet arrangement for the bias field configuration, while figure 5.5(b) shows the ODMR spectrum when using only the 25 mm \times 25 mm \times 13 mm magnet as the bias field arrangement. For figure 5.5(a) the microwave parameters used were a microwave power of 10 W, a frequency modulation amplitude of 4500 kHz and a modulation frequency of 3.0307 kHz. For figure 5.5(b) the microwave parameters were a microwave power of 0.2 W, a frequency modulation amplitude of 350 kHz and a modulation frequency of 3.0307 kHz.

ODMR spectra were also taken using the dual-magnet arrangement and single magnet arrangement, with and without the 1-mm-cube (Nd,Fe)B magnet, these spectra were taken in the absence of any microwave modulation to allow the broadening to the NV center linewidth to be quantified. For the dual magnet arrangement, corresponding to figure 5.5(a) the ODMR linewidth was 13.9 MHz. For the single magnet arrangement (using only the 25 mm \times 25 mm \times 13 mm magnet), the ODMR linewidth was 3.15 MHz, these values were determined through applying Lorentzian fits. For all ODMR spectra the step resolution was 20 kHz. As can be seen from figure 5.5(c) there is a reduction in the sensitivity by a factor of ~ 11 when the small 1 mm cube magnet is used. The sensitivity for the configuration corresponding to figure 5.5(a) is (9 ± 1) nT/ $\sqrt{\text{Hz}}$, whilst it is (0.8 ± 0.2) nT/ $\sqrt{\text{Hz}}$ for the configuration in figure 5.5(b). The highly inhomogeneous magnetic field across the active sensing volume (in the dual magnet arrangement) in the diamond led to a linewidth of 13.9 ± 0.1 MHz which gives an estimated dynamic range of 0.5 mT; this was calculated through using the NV center gyromagnetic ratio ($\gamma = 28$ Hz/nT).

5.7.3 Lift-off Vs. Height

To better understand the changes to the resonant frequency that are caused by changes to the magnetic permeability of the 316 stainless steel, variations to the LIA output were investigated by placing the sensor head directly above a blank piece (damage-free area) of 316 stainless steel and measuring the changes caused in the

LIA voltage output by lifting the sensor head between a range of 0 mm and 5 mm, in increments of 0.1 mm; this is shown in figure 5.4(c). The reference point to quantify the changes to the NV center ODMR resonance was chosen at a voltage of 0.6 V. This is the value that corresponds to the lowest frequency of the linear region of the NV center resonance, see figure 5.4(a).

It is clear from figure 5.4(c) that the relationship between the Zeeman-induced shift from the NV center is not linear with respect to the distance. It appears that there are two distinct regimes for the lift-off with a change in the profile occurring at ~ 1.5 mm. This profile is attributed to the dipolar field distribution that arises from the combination of two permanent magnets [273]. As expected this profile is independent of the sensitivity with the trend being near identical regardless of the parameters used. This independence is expected as provided the measurements are in the linear region of the ODMR feature, any differences should be entirely due to the bias magnets and their arrangement relative to the active area of sensing within the diamond. As such any distortions are directly due to the differences caused to the magnetic flux profile it is entirely possible to use this technique to map out the surface structure of a ferromagnetic materials.

5.8 Magnetic Mapping

The voltage change of the LIA output due to changes to the magnetic field sensor caused by the steel samples' surface structure are shown in figures 5.6(a) and (d). The step size resolution of the scans were 1 mm in the x and y directions. The % change of voltage shift in figures 5.6(a) and (d) are based on using the reference value of 0.6 V. The total scanning time to obtain the maps in figures 5.6(a) and (d) were approximately 66 minutes for a 20 mm by 45 mm scan, each point had a scan time of 2-3 seconds per point. It should be noted that the scan time per point can be reduced but several factors led to it being several seconds per point. One of the main reasons was that the motors of the stage are driven by currents supplied to the motors and can therefore induce a signal, as it was unknown when the motors would no longer provide a signal a minimum of 1 second was implemented before the data acquisition process began. The other reason was that the oscilloscope would take at a scan point and average for a given period of time and then export the data. There was also a limitation in how quickly the data could be exported from the oscilloscope to the computer and how quickly the computer could communicate back and forth with the stage. The damage is mapped out and is clearly visible as shown in figure 5.6(a) and 5.6(d). The lift-off distance between the surface of the sample and the sensor

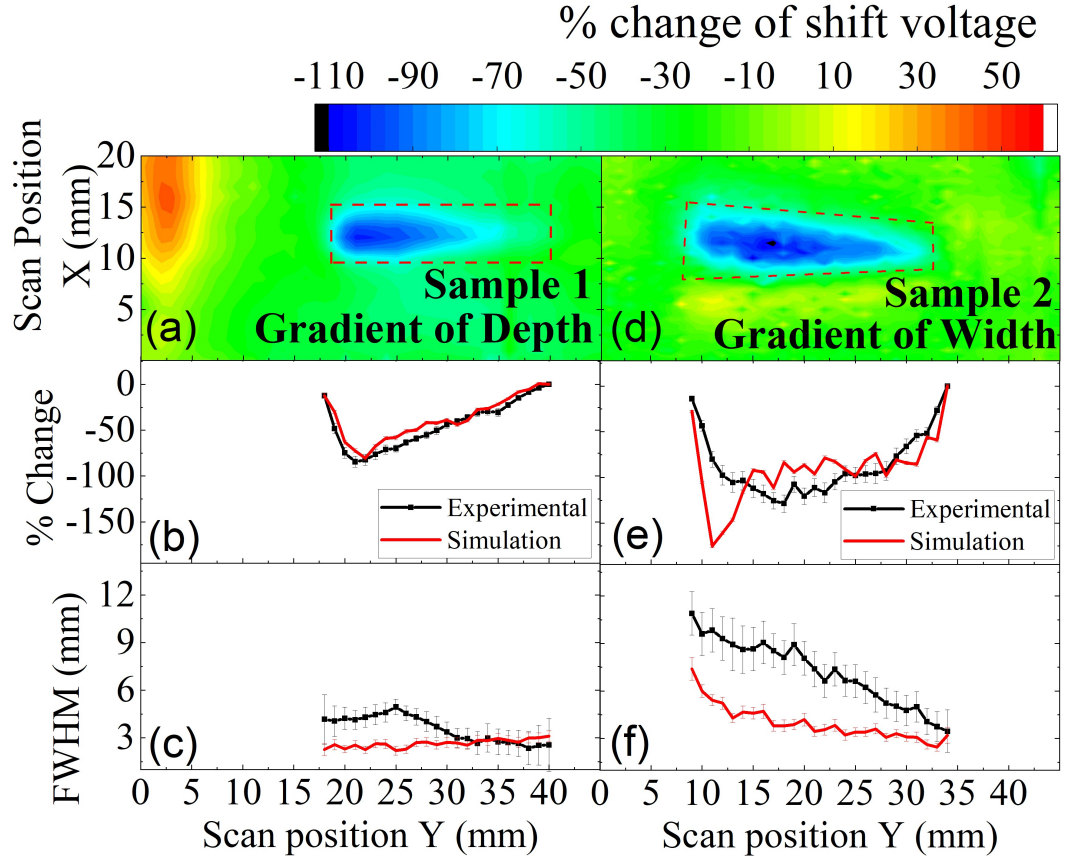


Figure 5.6: The 2D-scan results for the gradient-depth (sample 1) and gradient-width (sample 2) samples are shown in (a) and (d) respectively. The scan dimensions for (a) and (d) were 45 mm \times 20 mm. To quantify the damage, Lorentzian fits were applied to the cross sectional profile of (a) and (d). The amplitudes of the changes to the LIA voltage are shown in (b) and (e) respectively. The full width at half maximum (FWHM) of the cross section of both damage profiles imaged by the diamond magnetometer, (c) and (f), are shown for sample 1 and sample 2 respectively. COMSOL simulations were performed with the results shown in (b), (c), (e) and (f) for comparison.

head from the base of the antenna on the aluminum printed circuit board (PCB) was 0.2 mm for the scans in both figure 5.6(a) and 5.6(d). It is possible to quantify the differences in the depth and width through using the differences in the voltage and the calibration obtained by the lift-off process in figure 5.4(c). The artifact in the top left corner in figure 5.6(a), which represented an increase in the normalized voltage output is hypothesized to be due to the usage of a larger magnet which may be close enough to the edge of the stainless steel sample plate to interact with it. The two different damages in the ferromagnetic samples can be differentiated by the depth and width as shown in figure 5.6(a) and figure 5.6(d). The differences in the depth and the width can be quantified by assessing the profile of the cross sections from figures 5.6(a) and 5.6(d). This assessment was performed by applying Lorentzian fits across the width spanned by the damage in figures 5.6(a) and 5.6(d); this region is highlighted by the red boxed area. The profiles of the FWHM are as expected however the FWHM appears to increase and then decreases when for the gradient-depth slot when approaching toward the most rapid change in the damage, as shown in figure 5.6(c), while the FWHM for the gradient-width sample increases in an almost linear fashion in proportion to the width, see figure 5.6(f). The FWHM profile of the slot damage is most likely to due the approach of the magnets to the edge of the damage. Conversely, as expected the LIA voltage output increases in proportion to the increase of the depth of the damage as shown in figure 5.6(b). The rapid change to the shift in the voltage in the region of the scan position Y between the range 18 mm to 21 mm is attributed to the boundary of the damage edge where the depth change is maximum: a rapid change of 3 mm from damage to no damage. The step size resolution was 1 mm along the length of the damage as differences in the voltage corresponding to the damage profile can be observed it is believed that the spatial resolution is ~ 1 mm in x and y. In contrast, there is a shift in the LIA voltage output at the boundary edges on both sides of the edges of the damage for sample 2, figure 5.6(e) but as the scan approaches the center of the damage, at approximately 20 mm in the scan position in the Y axis the region around here is fairly consistent. There is noise in the COMSOL simulations however the reasons for this are unknown.

5.8.1 COMSOL simulations

To better understand the results of the maps obtained in figures 5.6(a) and 5.6(d), simulations using the commercial software COMSOL Multiphysics in the “Magnetic field, No current” mode were undertaken. The simulations of the damage in steel were three dimensional with the geometry of the samples matching the profiles of the

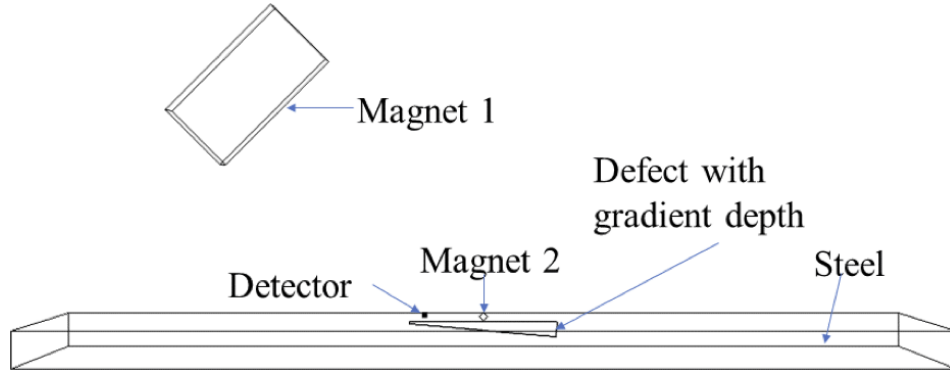


Figure 5.7: The COMSOL simulation of the experimental set-up: for simplicity the air space and mesh network have been ignored. The sample shown here is the gradient-depth sample. The detector in this case refers to the diamond.

gradient-depth and gradient-width samples, see figure 5.7. The magnet grades for the simulations were N45 and N42 for the 1 mm cube magnet and the larger magnet respectively; the relative magnetic field permeability for both magnets were set to 1.05. The 316 stainless steel relative permeability for simulations was set to 1.02. The results of the COMSOL simulations for the gradient-depth and gradient-width 316 stainless steel samples are shown in figures 5.8(a) and 5.8(b) respectively. The resolution step size for the scans were 0.25 mm along the x -axis and 1 mm along the y -axis. The COMSOL simulations of the experiment yield damage FWHM and magnitude profiles in agreement with the profiles obtained from the experiment. The fits to these damage were Lorentzian, these results are shown in figures 5.6(b), (c), (e), (f).

5.8.2 Damage Under Insulation

As steel corrosion under insulation is an important problem the stainless steel samples were covered with non-magnetic materials to demonstrate that it was still possible to map out damage as shown in figures 5.9(a)-5.9(d). For all maps the lift-off distance was 3.2 mm from the surface of the stainless steel. As the lift-off distance to the surface is larger the magnetic flux from the smaller magnet is incident over a larger area. This leads to a worse spatial resolution in the x and y directions, the plane parallel to the surface of the surface. In the z -axis the achievable spatial resolution was 0.1 mm, this was the limit of the step resolution in the z -axis. It is believed that the spatial resolution for the x -axis and y -axis is ~ 1 mm which is ultimately limited by the 1 mm size of the small magnet and the distance of the small magnet to the damage and from the diamond to the damage. It is possible that the

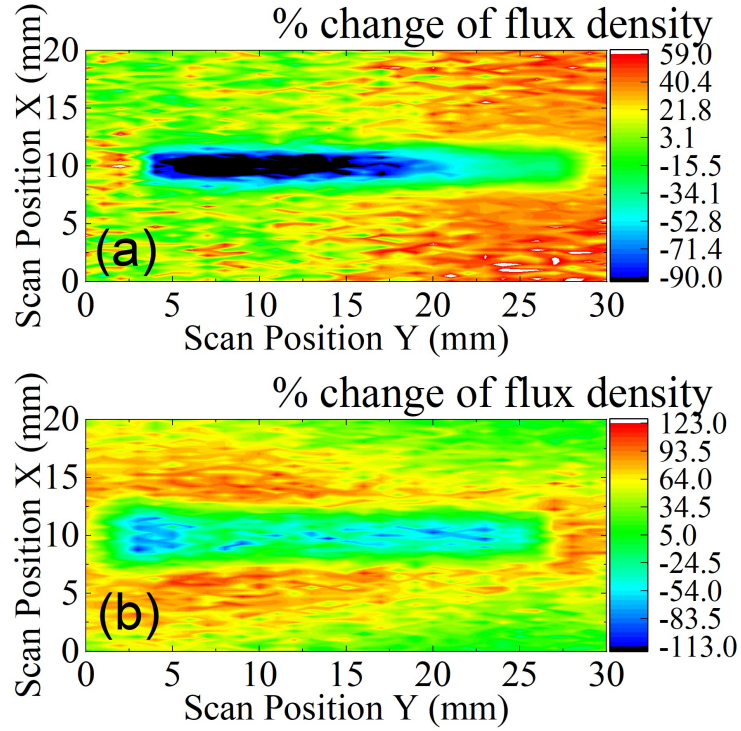


Figure 5.8: The simulation results of the 2D scans of the two 316 steel samples. The results of the scan for sample 1 (the gradient-depth) and sample 2 (the gradient-width) are (a) and (b) respectively.

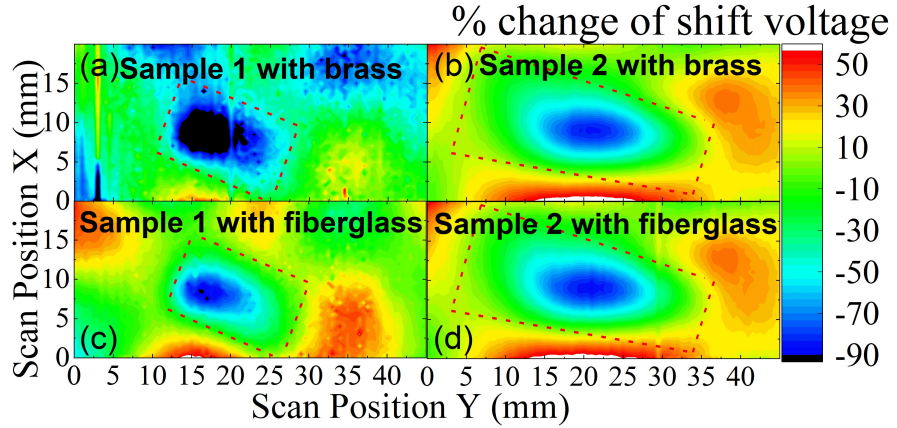


Figure 5.9: Two dimensional scans of the gradient-depth (sample 1) and gradient-width (sample 2) samples when covered with nonmagnetic materials. The scan dimensions were 45×20 mm. The dashed lines in the maps encapsulate the structural damage, (a) and (c) are from sample 1 while (b) and (d) are from sample 2. For (a) and (b) the stainless steel is covered with 1.5 mm of brass while for (c) and (d) the steel is covered with 2 mm of fiberglass.

minimum spatial resolution can be superior to 0.1 mm for the z -axis, this achievable resolution limit was set by the nominal resolution of the scanning stage in the z -axis; increments lower than 0.1 mm were not possible. It may be possible that the spatial resolution can be enhanced through using a smaller magnet, or to use a magnet that is shaped to have a sharp point facing the damage. Further improvements to the spatial resolution could also be possible by reducing the distance of the 1 mm cube magnet to the stainless steel samples and the diamond. There are far more spurious signals in these maps, when compared to the scans taken in figure 5.6. It is likely that as the smaller magnet is further away the magnitude of the detected signal is weaker and thus the contribution of the larger magnet and its interaction with the edges of the sample is larger.

5.9 Alternating Current

For these measurements, currents were applied through a pair of solenoid loops which were wrapped around the 316 stainless steel samples, see figure 5.10. A frequency of 80 Hz was used with the supplied voltage being 8 V. As is the case with the DC scans when scanning over the area of damage the percentage change in the LIA voltage output is mapped. For these scans the LIA reference voltage was 0.5 V, which occurred at ~ 3200 MHz in the ODMR spectrum; all scans were performed using this frequency. The microwave parameters used for these measurements were

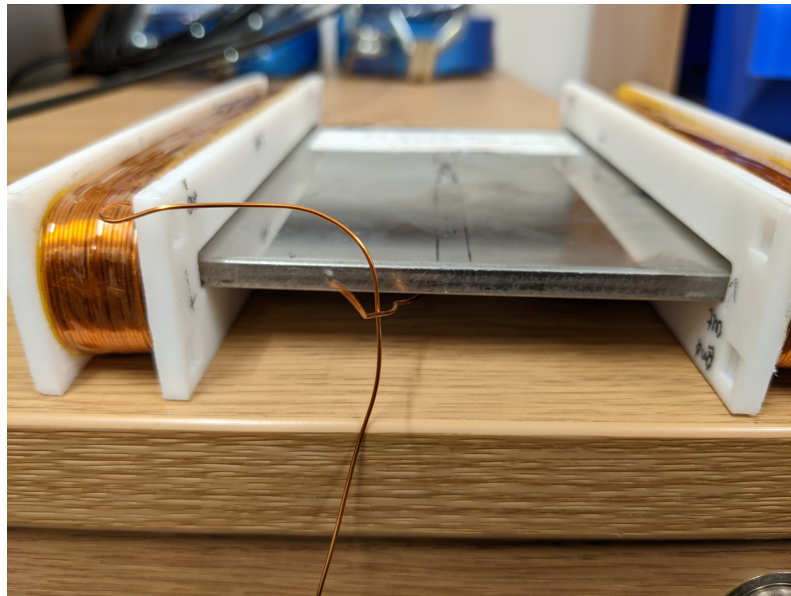


Figure 5.10: The placement of the two coils around a steel sample is shown.

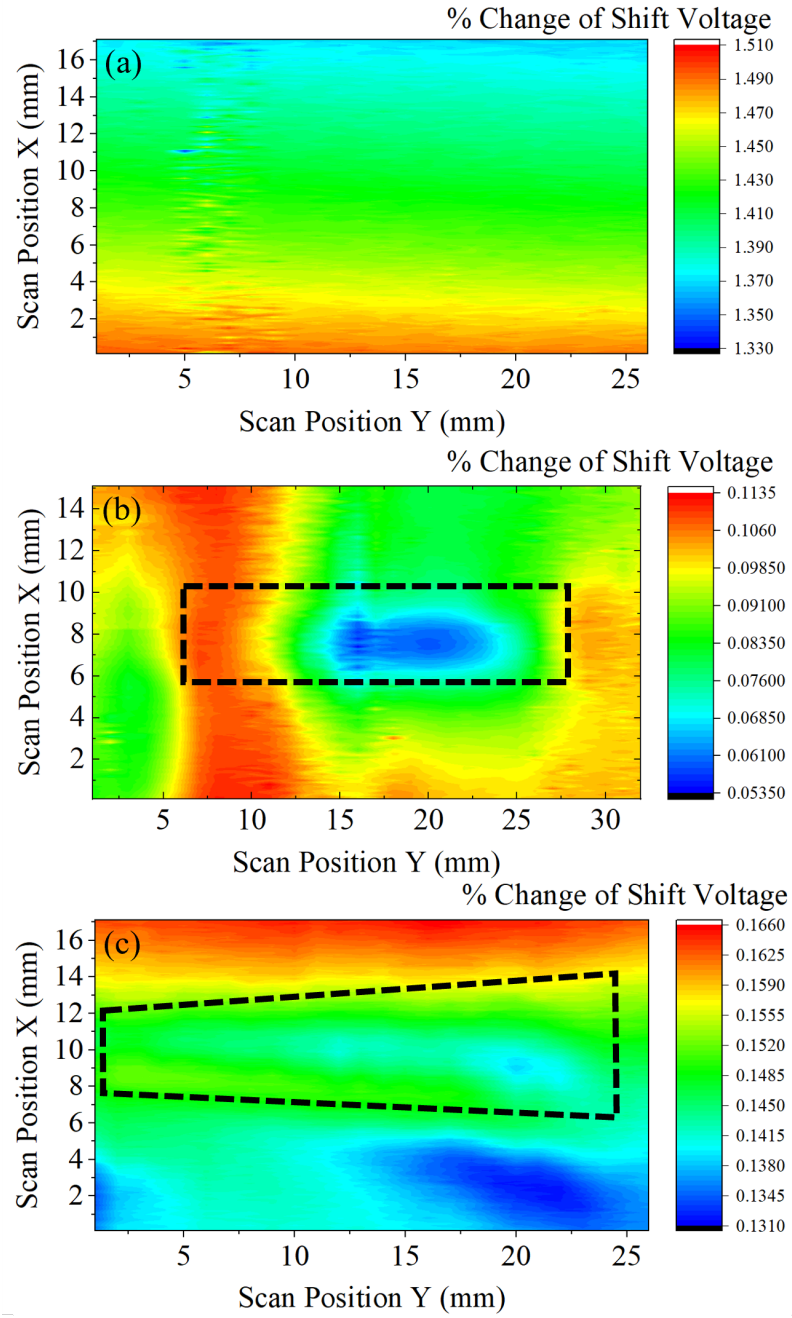


Figure 5.11: (a) The 2D scan results for (a) blank sample, (b) the gradient-depth and (c) the gradient-width samples. For all scans the step size was 0.1 mm in the x-axis while it was 1 mm in the y-axis. For (a) and (c) the scan parameters were 17.1 mm in the x-axis while it was 26 mm in the y-axis while for (b) the scan parameters were 15.1 mm in the x-axis while it was 32 mm in the y-axis. The damage slots are illustrated by the dashed boxes.

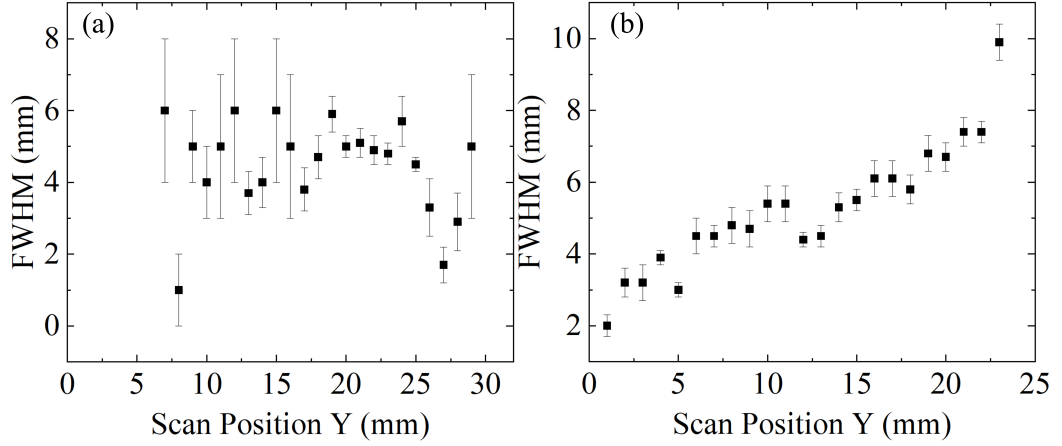


Figure 5.12: The full width at half-maximum (FWHM) of the (a) gradient-depth and (b) gradient-width samples.

a microwave power of 10 W, a frequency modulation amplitude of 4.5 MHz and the 3.0307 kHz modulation frequency. It is expected that near the vicinity of the damage the induced magnetic field signals will be reduced as the electric conductivity of the steel samples is larger than air and there is a loss of material. These changes will be reflected in the LIA voltage output. The step size for the scans were 0.1 mm in the y-axis and 1 mm in the x-axis.

Scans were taken over a 316 stainless steel sample that had no visible damage (see figure 5.11(a)); there are no significant shifts in the output of the LIA voltage though there is a clear linear trend in the direction of the x-axis. This confirms that the profiles of the two samples obtained in (b) and (c) are due to the damage placed in steel. Furthermore, there is a clear trend which causes a change in the voltage output. Though this output change is small, it is believed that this trend is due to the experimental configuration where the sensor itself approaches the vicinity of the AC excitation coils. In addition, the number of coils on each of the two sides are not identical and it is likely that the central point between the coils may not coincide with the center line of the damage profile. Figures 5.11(b) and (c) display the maps obtained for the gradient-depth and gradient-width samples respectively. For both samples the location of the damage is clearly visible with the obtained profiles, though the profile for the gradient-depth slot is much clearer in the maps obtained. As is the case with the DC measurements the profiles can be obtained by applying Lorentzian fits to the dashed regions, the results of these fits are shown in figure 5.12. These results agree with the expected results.

There are several artifacts in the scans and it is believed that these originate

due to the poor SNR. The magnetometer sensitivity was $(37 \pm 2) \text{ nT}/\sqrt{\text{Hz}}$ in the frequency range of 70-130 Hz with a photon shot-noise limit of $(0.7 \pm 0.1) \text{ nT}/\sqrt{\text{Hz}}$. In these measurements, changes to the induced 80 Hz magnetic field are measured, and as the sensitivity is poor it is hard to measure the changes to the induced signal. If the small 1-mm-cubed magnet was removed the sensitivity could be enhanced by at least an order of magnitude. This would significantly improve obtained results and could perhaps mitigate the effects of the artifacts obtained.

5.10 Conclusion and Future Goals

In this work a fiber-coupled magnetometer based on diamonds has been used to aid in the development of a technique that can image damage in ferromagnetic materials through the monitoring of the magnetic flux profile of a nearby pair of magnets. As the NV center detects magnet field changes through Zeeman induced shifts to the Zeeman splitting, an NV-center-containing diamond is the ideal magnetometer to use in conjunction with this technique. It is possible to use this configuration to differentiate between the width and depth of damage profiles in 316 stainless steel and this can be extended to determine damage in any ferromagnetic material for NDT purposes. Simulations were undertaken using COMSOL which allowed a better understanding of the magnetic flux perturbation method; the profiles of the experiments matched with those of the simulations. Significant benefits to the overall scanning are expected if a proportional–integral–derivative (PID) controller system could be implemented to track the NV center resonance, this would extend the dynamic range whilst preventing any loss in the sensitivity. Furthermore, it may be possible to improve the measurements by modifying the magnet configuration by using a (111)-oriented diamond and placing the 1 mm cube magnet directly underneath the diamond, and replacing the larger rectangular magnet with a ring magnet. The ring magnet could be oriented such that the direction of the magnetic field is along the (111) direction. This could be placed on a holder that is affixed onto the sensor head that could be adjusted in the z -axis which would allow an optimization of the sensitivity and the dynamic range.

In the case of the alternating current measurements it is certainly possible to improve the sensitivity through the removal of the 1 mm^3 magnet as the induced AC signal is typically not enough to shift the magnetometer off resonance, however if a PID tracker were implemented here it would provide a far greater benefit. Furthermore, the modification of the geometry of the excitation coils to a single one that surrounds sensor head could narrow the area of excitation and improve the results.

In the case of both methods developed/used in this chapter there are still issues that need to be overcome for these techniques to be employed in industry. For example an improvement in the spatial resolution. Techniques such as magnetic flux leakage are still superior as they have reached maturity whilst magnetic flux distortion requires more investigation to overcome some of the issues present. However, it is expected that further investigation will allow these limitations to be overcome.

Chapter 6

Development of a Magnetic Gradiometer Towards Performing Magnetocardiography

Among the leading cause of death globally are heart-related illnesses such as ischemic heart disease [274; 275; 276; 277; 278]. Current methods to identify heart-related illnesses include electrocardiography (ECG) which records the electrical activity of the heart. This activity arises from the depolarization and repolarization of the heart during each cardiac cycle [279]. Distortions to the “expected” ECG trace can reveal several cardiac abnormalities, however, due to the need to attach electrodes on the skin the electric signal from the heart can be distorted by the differing conductivity of human muscles and tissue resulting in errors in the identification of heart-related conditions [280]. Conversely, magnetocardiography (MCG) is a non-invasive technique that detects the magnetic fields produced by cardiac currents and has demonstrated to be superior in the identification of illnesses when compared to ECG [276; 281; 282; 87; 138] and can offer superior localization of said conditions [86]. An ECG or MCG trace has several features with strongest signal coming from a feature called the QRS complex, it is the central peak and a feature that is one of the three main signals present when taking an ECG or MCG measurement. The cardiac magnetic fields produced by the heart are typically in the range of 0.1 to 100 pT and occur in the frequency range of 0.1 to 100 Hz, the peak of the QRS wave is the largest (40–100 pT) whilst the smaller features of the MCG signal are 0.1–10 pT [253]. As these cardiac magnetic fields are several orders of magnitude weaker than surrounding ambient fields, historically, the only magnetometers which have been capable of performing MCG have been superconducting quantum inter-

ference devices (SQUIDs) [84]. These measurements have also typically been made in shielded rooms. However, SQUID magnetometer technology requires cryogenic cooling with liquid helium in addition to requiring magnetically shielded rooms (unless a gradiometer configuration is used) which has prevented widespread adoption of MCG in the healthcare industry [283]. Newer technologies that have arisen that offer comparable sensitivities to the SQUID magnetometers and do not require cryogenic cooling are atomic vapor cells [284] and induction coils which have been capable of mapping cardiac magnetic fields in an unshielded environment [285].

This chapter concerns the development of a magnetic gradiometer, a project which is ongoing, which employs two sensor heads. The gradiometer was developed in an attempt to make unshielded MCG measurements. As shown in previous chapters the sensitivity of the magnetometer employed is limited by various noise sources. It is believed that the use of a gradiometer would allow some of the noise sources that are common to both sensor heads to be alleviated and thus allowing signals that are much weaker than the environment to be detected. Though the objective of detecting the magnetic signal from a heart was not achieved, a gradiometer has been developed and this system was characterized. Signal processing techniques that could enhance the SNR have also been investigated. NV center based gradiometers have already been developed with an experiment that employs a Ramsey scheme to achieve a sensitivity of $2.6 - 6 \text{ pT}/\sqrt{\text{Hz}}$, this system was able to detect a minimum magnetic field of $0.3\text{--}0.7 \text{ pT}$ though the measurement took 73 s [286].

6.1 Gradiometer

As cardiac magnetic fields are orders of magnitude weaker than surrounding ambient magnetic fields, in order to perform unshielded measurements a gradiometer configuration could allow common mode noise rejection [287]. For this section the intention was the construction of a magnetic gradiometer based on two fiber-coupled diamond magnetometers. A 532 nm Laser Quantum 6 W Opus laser was used to excite the two NV center ensembles in all configurations, a higher power laser was chosen over the 2 W Laser Quantum Gem so that a greater amount of photons from the NV center would be incident on the photodiode. Different gradiometer configurations were considered to investigate the effectiveness for canceling noise all would involve having two diamond magnetometer sensor heads: 1) having two sensor heads whereby each replicate the configuration used in chapter 4 where a portion of the laser output is subtracted from the NV fluorescence signal using a balanced detector. The signal from each balanced detector would be sent into the LIA and the resultant

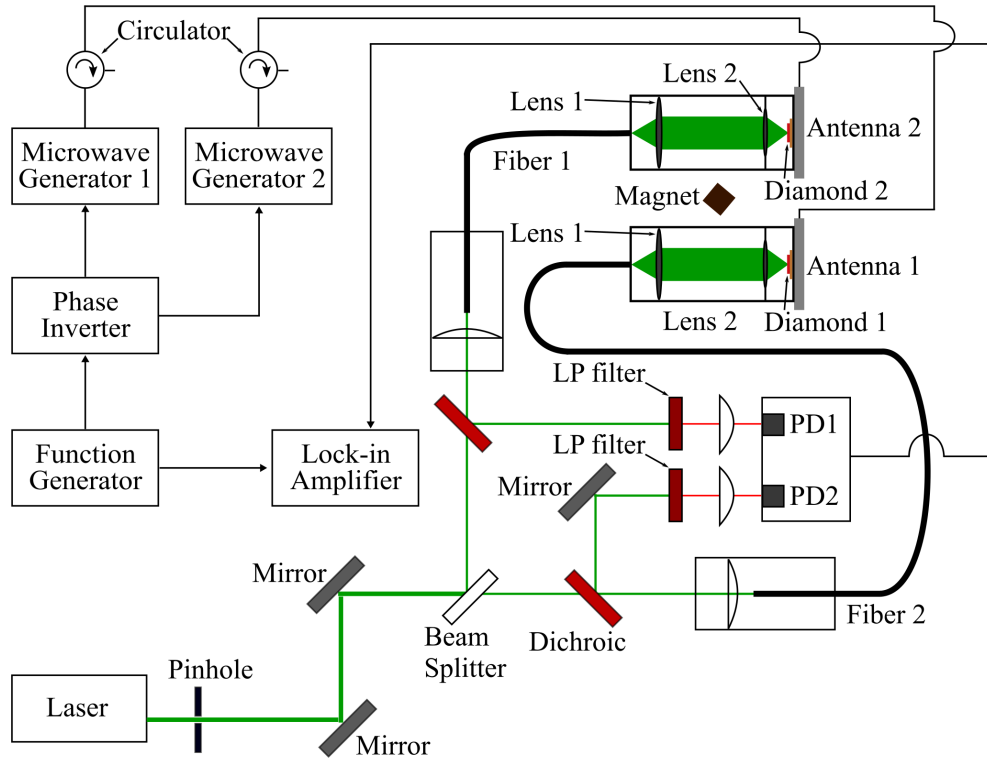


Figure 6.1: The experimental setup of the gradiometer when taking an approach of subtracting a magnetically sensitive nitrogen vacancy photoluminescence signal from another.

signals would be subtracted from one another. 2) Operating one sensor head in a magnetically sensitive mode (on resonance) whilst the other is not magnetically sensitive (off resonance - it is not necessary to supply microwaves to this sensor head); the red fluorescence signals would be subtracted from one another using a balanced detector (this would require only a single balanced detector); this would help assess laser noise. 3) Operating both sensor heads in a magnetically sensitive mode (on resonance) and subtracting the signals using a single balanced detector. For this chapter only data relating to both sensor heads being magnetically sensitive was obtained, the third configuration.

6.1.1 Red-Red Subtraction

In this configuration the method of subtraction was to subtract the fluorescence of one NV center sensor from another, see figure 6.1 i.e. both sensor heads would be magnetically sensitive. A pair of mirrors were used to direct the laser output to a 50:50 beam splitter (Thorlabs BSW41-532). One of the two beams is directed

to a dichroic filter (Thorlabs DMSP650) and then focused using an aspheric lens (Thorlabs C171TMD-A) into a 5 m long custom-ordered fiber (Thorlabs FG400AEA-Custom). The materials used for the fiber end connectors were customized. The sensor head arrangement used here is identical to that of chapter 3, however the lens closest to the fiber in the sensor head was replaced with a Thorlabs C171TMD-A, an A-coat rather than a B-coat as this led to a higher NV center photon collection rate out of the fiber.

6.1.2 Microwave System

The microwave antenna in this work was swapped out from an aluminum substrate to that of a silicon carbide (SiC) substrate. This was due to the superior thermal and microwave properties which allow for a higher sensitivity; it was believed that the SiC would be able to offer a superior performance when it came to the microwave delivery and would help minimize thermal induced fluctuations. For the side of the SiC that was used for the delivery of microwaves a 2 mm loop was deposited. The deposition involved three layers: titanium, silver and then gold; the respective thickness of each layer was 1.5 nm, 15 μm and 1.5 nm. The titanium was used to help the silver stick to the SiC. The silver was chosen for its excellent reflection of green and red light. The gold layer prevents the silver from oxidizing. The other side of the SiC quartered wafer was deposited with a thin layer of silver to prevent light leakage. The SiC itself was affixed onto an antenna holder made out of copper. This itself was connected to an aluminum holder; this aluminum holder was affixed to the SM1 holder. To deliver the microwaves to the SiC a second FR4 board was prepared with thin copper used to connect to the deposited tri-layer of the SiC, with thin copper wires soldered to connect the FR4 to the SiC. Due to damage to one of the SiC antennae, one of the SiC antennae had to be replaced with one of the custom-made aluminum microwave delivery antenna boards (C.I.F AAT10). Two microwave sources, both Keysight Agilents (N5172B and E8257D) were used to supply the microwaves to each antenna.

As the same modulation reference frequency would be used for both sensor heads a π -phase shift was used to generate two signals which had the same frequency modulation and modulation amplitude but were π out of phase with one another. This was due to that fact that a single balanced detector was used. To synchronize the microwave sources an external reference frequency was generated using an arbitrary function generator (RSPro AFG21005) and this output was directed into a phase inverter which produced the two outputs that were π out of phase. These two outputs were used as the reference of the modulation frequency for the two

microwave sources. To prevent any microwave back-reflection two microwave circulators (Pasternick PE83CR005) were employed and were placed just before the microwave antenna. Noise cancellation of the two NV photoluminescence signals were achieved by using a balanced detector (Thorlabs PDB450A). As the modulation phase is π radians out of phase the modulation frequency would be subtracted when the balanced detector would subtract the NV fluorescence signals from one another. A dual channel lock-in amplifier (Zurich HF2LI) is used to extract and separate the two signals from the balanced detector's output; as each signal was π radians out of phase they could be extracted even though they had the same modulation frequency and amplitude. It is expected that the noise from amplitude changes to the lasers output should be canceled out in addition to any noise that may arise from any changes to the frequency output of the laser.

6.2 Diamond Material Properties

The diamonds employed in this work are (100) ^{12}C -enriched (99.995% enrichment) samples provided by Element Six [288]. The diamond was initially of dimensions $2.97 \text{ mm} \times 2.93 \text{ mm} \times 0.93 \text{ mm}$ prior to being laser cut into nine equal pieces. Each of the smaller cube diamonds were mechanically polished so all six faces had an optical grade finish, each side was around $0.7\text{-}0.1 \text{ mm}$. A key requirement for a gradiometer which has two sensors is that each magnetic sensor should be as similar as possible. To that end the diamond used in this work was characterized to determine both defect concentration and sample homogeneity. Characterization of the sample to determine defect concentration was performed through UV-Vis spectroscopy, FTIR spectroscopy and EPR.

EPR studies were performed upon the sample using a Bruker EMX spectrometer equipped with a 90 dB microwave bridge and a Bruker SHQ cavity. It was found that the negatively charged NV center was $(3.9 \pm 0.3) \text{ ppm}$, the neutral substitutional nitrogen has a concentration of $(6.1 \pm 0.3) \text{ ppm}$ and there was $(2.2 \pm 0.2) \text{ ppm}$ of negatively charged hydrogen nitrogen vacancy. FTIR measurements were taken once the sample had been laser cut into nine pieces using a Perkin Elmer Spectrum GX FT-IR spectrometer, the concentrations are shown in table 6.1. For the gradiometer the two diamonds used were samples A and H. These two were chosen as they gave the same photoluminescence levels when the same laser power was directed toward them.

Diamond Defect Concentration			
Sample	$[N_s^0]$	$[N_s^+]$	$[N_3VH]$ 3107 cm^{-1}
A	5.2 ppm	2.4 ppm	1.0 ppm
B	6.1 ppm	2.4 ppm	1.1 ppm
C	3.6 ppm	1.5 ppm	1.1 ppm
D	5.2 ppm	2.3 ppm	1.1 ppm
E	5.3 ppm	2.8 ppm	1.0 ppm
F	5.6 ppm	1.4 ppm	1.3 ppm
G	6.8 ppm	-	1.0 ppm
H	5.5 ppm	1.2 ppm	0.95 ppm
I	5.0 ppm	1.9 ppm	1.1 ppm

Table 6.1: The concentration of defect in the diamond samples used in the gradiometer.

6.3 Signal Processing

As was mentioned in previous chapters the magnetic fields generated by the heart are significantly weaker than the background magnetic fields. For this reason if one wishes to perform unshielded measurements a variety of different signal processing techniques are employed to be able to enhance the SNR and extract the signal. In this section a variety of different techniques are investigated to determine which techniques are applicable.

6.3.1 Signal Averaging

A common method to enhance the SNR is the utilization of signal averaging in the time domain to enhance the signal relative to the noise present within the environment. This method is useful for the removal of random noise that is not related to the signal of interest. For MCG this involves averaging over multiple MCG traces; a trace is the entire duration of the cardiac magnetic field signal: the P wave, the QRS complex and the T wave. To successfully average multiple MCG traces, ECG measurements are taken concurrently whilst performing MCG measurements where the peak of the QRS complex is used as a marker; the location of the peaks of the QRS complex for both ECG and MCG should occur at the same time and thus the QRS peak in the ECG can be used as a trigger for averaging the MCG measurements with the oscilloscope. A custom-built three-lead ECG system was used to obtain ECG measurements. As the gradiometer was in the stage of being developed a sufficient sensitivity had not yet been reached and thus the averaging was tested out on ECG data instead of MCG data. ECG data was averaged to test the improvements to the SNR; it is assumed that any SNR improvements to the ECG signal would translate

to that of the MCG signal. 100 s worth of ECG data was taken and a script in Python was then written to analyze the data. The peak of the ECG QRS complex was identified for all cardiac cycles. This was the basis for the reference point, a slice of the data in the range of $-220 < t < 350$ ms around this reference point was taken for all identified peaks, see figure 6.2(a). The improvements to the SNR through averaging are expected to be, $\text{SNR} = \sqrt{n}$, where n is the number of cardiac cycles; for clarity only 17 ECG cardiac traces were averaged over rather than the full 100 s of the ECG data. For the trace in figure 6.2(b) it is expected that the improvement to the SNR would be ~ 4 . It should be noted that although random noise can be attenuated it is not possible to remove non-random noise; some noise signals may be correlated with the ECG trace and these signals would be enhanced when averaging. Thus averaging would only be used in the case where other signal processing methods have been used to remove noise that is periodic to the MCG trace or in cases where this type of noise is not present in the MCG trace to begin with.

6.3.2 Wavelet Denoising

A common method for denoising a signal is the wavelet transform. The wavelet transform is advantageous for ECG and MCG when compared to an FFT-based

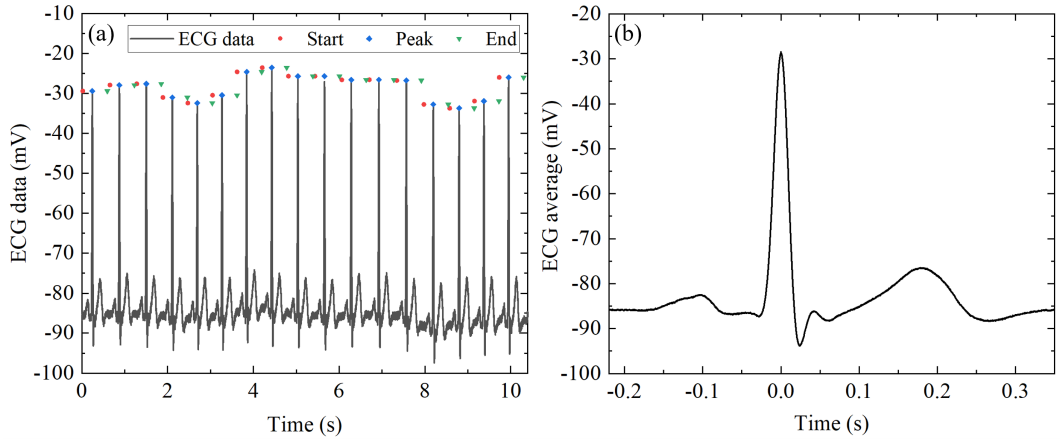


Figure 6.2: (a) A 10.4 second ECG trace is shown; although data was taken for 100 s for clarity only a portion is shown and used for averaging. There are a total of 17 cardiac traces present with the blue square marker indicating the peak of the QRS complex. The orange cross is the negative time (-220 ms from the QRS complex peak) while the green cross is the positive time (350 ms from the QRS complex peak). The sample rate was 5000 samples/s. (b) The ECG trace shown here is the average of 17 cardiac traces.

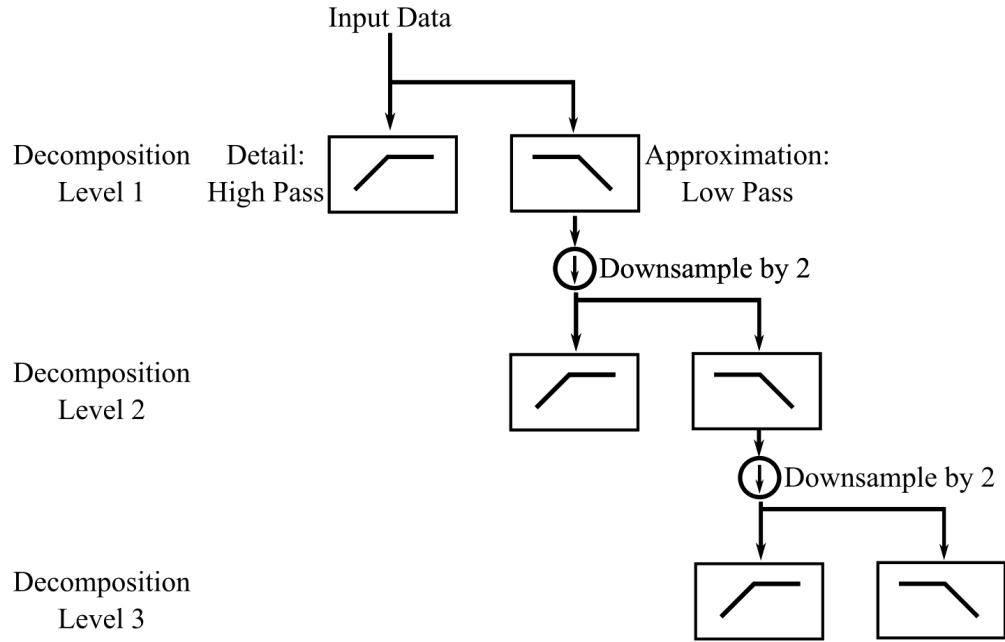


Figure 6.3: A 3 level decomposition of data. This process is the method of taking a discrete wavelet transform.

approach as it is better able to analyze signals that vary in time. The FFT has excellent capabilities in the frequency domain but is poor in the time domain; it can only process information that has been globally averaged, certain features that are localized in time are typically obscured. Conversely wavelet denoising has good temporal capabilities and is thus ideal for non-stationary signals [289].

There are two forms of wavelet denoising: continuous wavelet transform (CWT) and the discrete wavelet transform (DWT), however all modern processes use the DWT as it is more computationally efficient. The DWT passes one copy of the data through a high-pass filter, and one copy through low-pass filter; the output of this gives the detail and approximation coefficients. The detail and approximation coefficients are therefore respectively the high-pass (wavelet coefficients) and low-pass representations of the signal. The high-pass and low-pass filter coefficients are determined by the choice of the wavelet. There are many different families of wavelets, and it is typical to choose a wavelet whose morphology is closely matched to the signal of interest. If the wavelet is more closely matched to the signal of interest it will be easier to separate the noise and signal components [290; 291]; for optimum performance the filter will ideally be constructed by the user to provide the closest match possible; this is similar to when a matched filter is used. A multilayer decomposition is performed where the approximation coefficients produced by the

DWT process are used as the input convolution for the next decomposition level with the high-pass and low-pass filter producing the detail and approximation levels of the next layer. The cut-off frequency of each successive decomposition level is reduced by a factor of two; in effect this allows the sample number to be halved as per the Nyquist rule. The process for the DWT is depicted in figure 6.3. In the case of the wavelet transform, as the signal is typically coherent and concentrated it will be represented by a few high-magnitude components while noise which is typically incoherent will be spread out over many small-magnitude coefficients. It is possible to then remove/reduce these noise coefficients in the wavelet domain by applying an appropriate threshold. This threshold can be implemented in several ways but ultimately serves to remove the noise coefficients whilst preserving the high magnitude signal coefficients [292; 293; 290]. The modified approximation and detail coefficients are then taken, and an inverse DWT is performed to reconstruct the signal which has now been denoised.

The algorithm employed for denoising signals in this work was one that was developed by Dr. Srivastava's for the denoising of EPR signals and will be summarized; explicit details regarding the algorithm can be found in reference [290]. The process for Dr. Srivastava's wavelet denoising algorithm is to select a suitable wavelet and use this to decompose the input data (which contains both the signal and noise). This will decompose the data into a series of levels with the maximum decomposition number being determined by the length of the input signal, XX ; each decomposition layer will have an associated approximation and detail coefficient layer. The maximum number of levels, NN , is determined by the length of the input signal, $NN = \log_2(XX)$. The maximum useful level of decomposition is determined by both the length of the input signal and the wavelet filter length. There will come a point where there is no more useful information beyond a certain decomposition level even if the maximum decomposition level has not been reached. This will produce a total of kk decomposition levels with NN approximation and detail coefficient components. Though a total of NN decomposition levels are obtained only those from level 1 to level kk are required, where kk is less than or equal to NN . The sparsity is a measure of the distribution of noise relative to the signal for each detail component and is calculated to determine which detail component level, kk should be selected. The higher the sparsity the more the signal components are spread out i.e., the noise is no longer distinguishable from the signal. The noise coefficients for each detail component are estimated and an applicable noise threshold is calculated to remove the noise values whilst preserving the signal coefficients. This is applied for each detail level up to the kk^{th} level while for the approximation

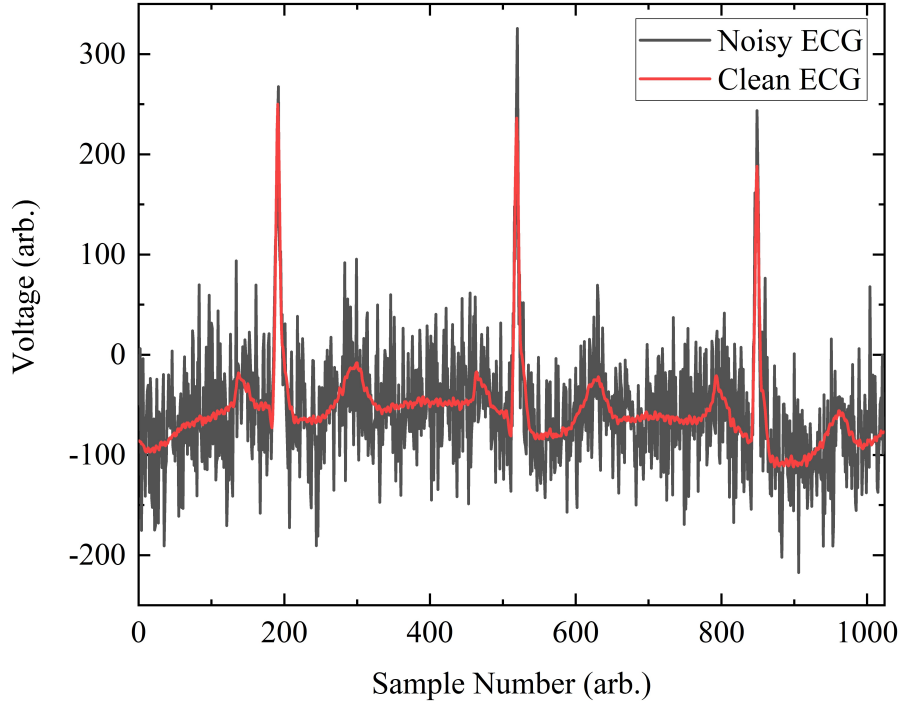


Figure 6.4: The data shown here is a synthetic ECG signal and one with random noise added with a mean of zero and a standard deviation of 45.

level it is applied only to the kk^{th} level. The inverse DWT is then taken using all the detail coefficients up to the kk^{th} level whilst only the kk^{th} approximation level is used. This will lead to a reconstruction of the signal of interest where the noise has been reduced.

To determine the effectiveness of this denoising method an ECG signal was used and noise in the form of random Gaussian noise and 50 Hz noise were added. These two types of noise were chosen as they are what is encountered when taking magnetometry measurements. 50 Hz mains noise is highly common so the effect of wavelet denoising in this case was of particular interest. For these tests as the morphology of the ECG and MCG signals are similar it is assumed that any effective noise cancellation that could denoise an ECG signal will also be effective in denoising an MCG signal. The ECG data used in this was one provided by the PyWavelets Python package [294]. This package was also used to implement the algorithm developed by Dr. Srivastava's [290]. The noisy signal was processed using the denoising algorithm and as the data length of the ECG signal was of length 1024, this produces a maximum of 8 decomposition levels, see figure. In each successive decomposition level, the number of samples are halved. For this level of noise, a

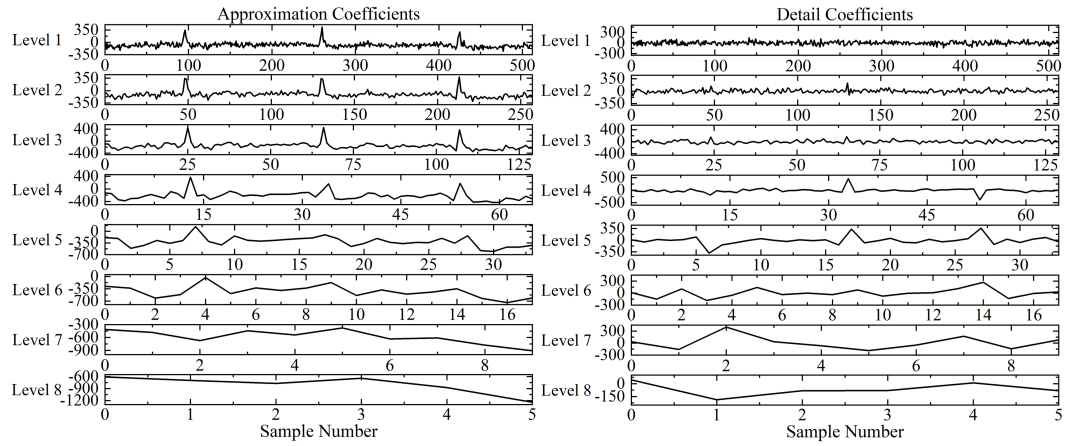


Figure 6.5: The approximation and detail coefficients of the noisy data are shown, due to the use of db2 as the choice of filter there are 8 levels of decomposition.

standard deviation of 45 was selected.

To test the effectiveness of the noise cancellation for random Gaussian noise, see figure 6.4 (the noise added for this had a standard deviation of 45) various standard deviations were used and the signal denoised. The approximation and detail coefficients produced when taking the DWT of the noisy signal is shown in figure 6.5. As can be seen from figure 6.6 it is possible to extract the profile of the ECG signal and remove a reasonable amount of the random noise though the original ECG signal was distorted, the significant distortion to the smaller features in particular is problematic. It is believed that as the levels of random noise added to the signal are much larger than the smaller features and thus significantly distort it making extraction difficult. In order to improve the effectiveness of wavelet denoising, a custom wavelet whose features more closely match the MCG profile may be needed. Wavelet denoising therefore should only be used in cases where the random noise is small and so it may be better to use this method once the data has been averaged to reduce the levels of random noise that could be present in an MCG trace.

The root mean-square error (RMSE) was calculated for various decomposition levels for each standard deviation value to determine the best decomposition level to achieve the most effective noise cancellation, these results are shown in table 6.2. As expected, the RMSE increases with the standard deviation of the noise added, with it being harder to detect certain features associated with the ECG signal when the noise level becomes higher. It was found that using the 5th decomposition level for taking the inverse DWT to reconstruct the original signal for any of the chosen standard deviation values resulted in a severe distortion to the ECG signal with the

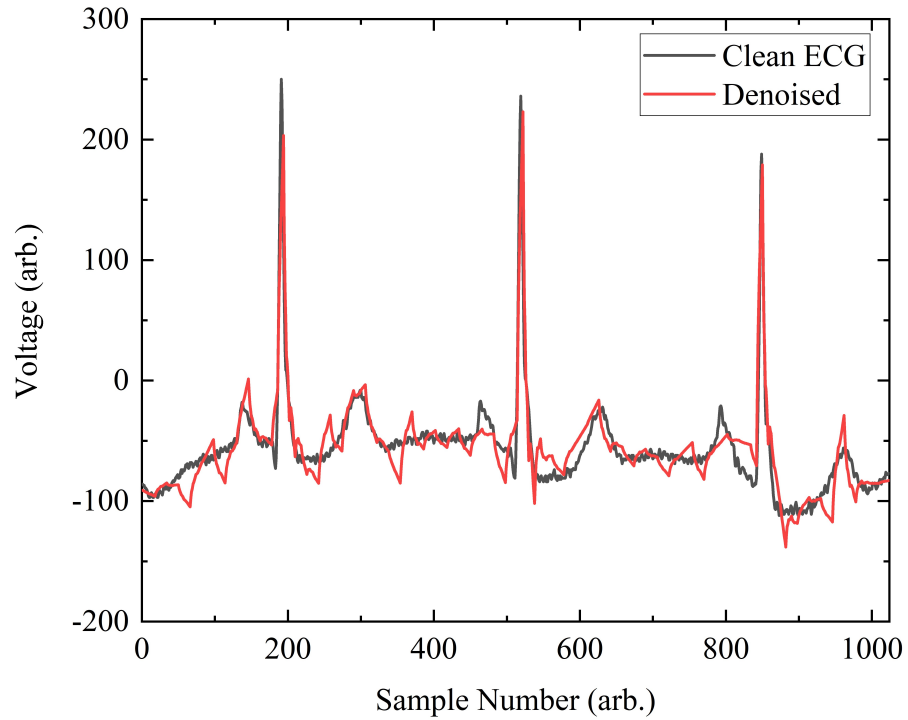


Figure 6.6: The original ECG signal is shown along with the denoised signal.

baseline of the entire signal now having mean of zero.

Two wavelets families were investigated, the Coiflets and Daubechies families and it was found from some of the investigations that the best wavelet choices from the RMSE values that were examined were the Coiflets 2 (coif2) and the Daubechies 2 (db2) wavelets. It was found between the two that the coif 2 wavelet was slightly

Random Noise Denoising		
Standard Deviation	Decomposition Level	Root-mean Square Error
10	2	0.20
15	2	0.28
20	4	0.34
25	4	0.34
30	3	0.41
35	3	0.44
40	4	0.46
45	4	0.52

Table 6.2: The root-mean square error (RMSE) of various standard deviations when applying random noise to a clean ECG signal and denoising it are shown. The decomposition level listed here is the ideal level that gives the best RMSE value.

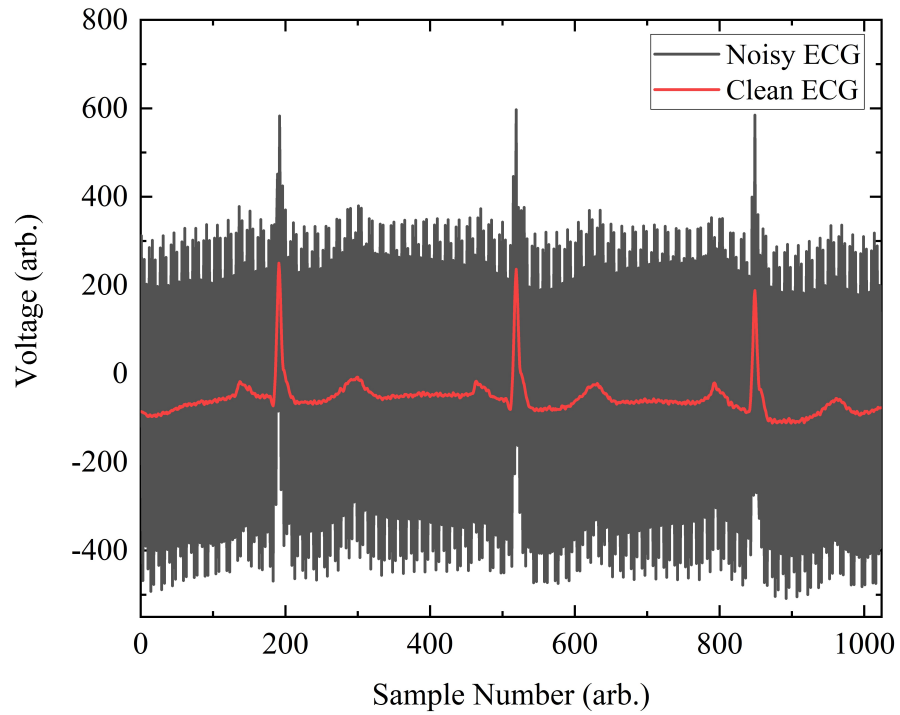


Figure 6.7: The data shown here is the original ECG signal and data to where 50 Hz noise has been artificially added to the signal; the magnitude of the 50 Hz is 400.

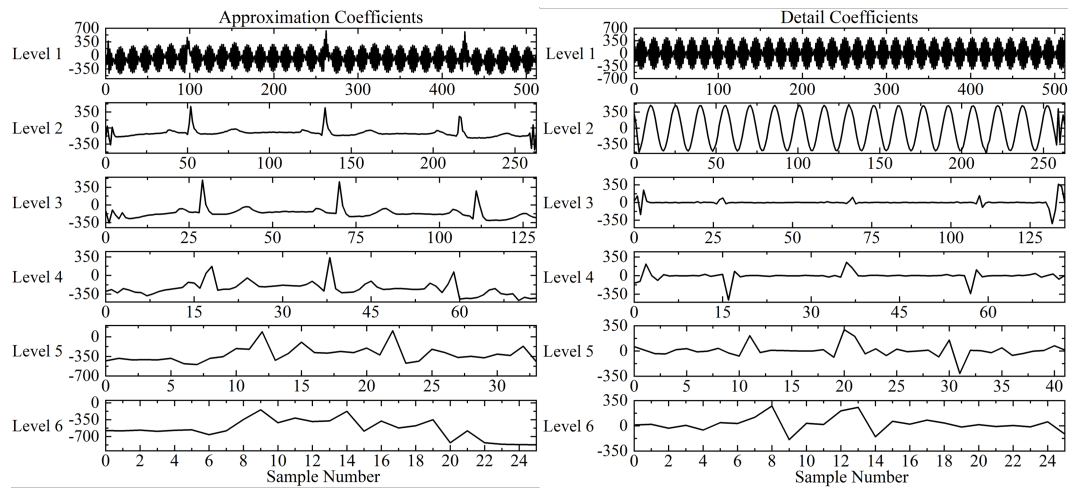


Figure 6.8: The approximation and detail coefficients of the data that has had 50 Hz added to the signal is shown. In this case the `coif2` wavelet was used to decompose the noisy signal leading to a total of six decomposition levels.

Mains Noise Denoising		
Magnitude of 50 Hz Noise	Decomposition Level	Root-mean Square Error
5	1	0.077
50	2	0.12
100	2	0.13
200	2	0.19
400	2	0.32
1000	4	0.75
2000	4	1.52

Table 6.3: The magnitude of the 50 Hz signal that is applied is listed along with the best decomposition level to achieve the lowest root-mean square error when comparing the denoised signal to the original ECG signal. The magnitude of 50 Hz is given as a value relative to the voltage.

superior in some instances of denoising but for the most part the db2 and coif2 wavelets were equivalent.

The other noise that was added to the ECG data was 50 Hz mains noise. For all magnetic measurements undertaken in the lab this noise is most prevalent. It is typically orders of magnitude larger than the expected MCG signal whose peak is typically around 40 pT; conversely the magnitude of the 50 Hz mains signal can be anywhere between tens of nanotesla to several hundred depending on the environment. Though a gradiometer should alleviate most of this to effectively remove all 50 Hz noise the sensitivity of each sensor in the gradiometer would have to be identical, which in practice is difficult to achieve. In the two-sensor gradiometer that was implemented the sensitivity of both sensor heads differed and so the 50 Hz mains noise was reduced but could not be removed completely. To investigate the effectiveness of noise cancellation similar to the random noise analysis various magnitudes of 50 Hz was added to the ECG signal. An example is shown in figure 6.7; the detail and approximation coefficients produced when taking the denoised and the RMSE was calculated, see table 6.3. In all instances of denoising it was found that it was possible to reconstruct the original ECG signal along with the smaller features around the ECG QRS peak (see figure 6.9) which was distorted when random noise was the main source of noise. The only distortion is the changes to the start and end of the denoised signal however this does not affect the reconstruction of the main features of the signal; in addition this only became significant at higher 50 Hz noise magnitudes.

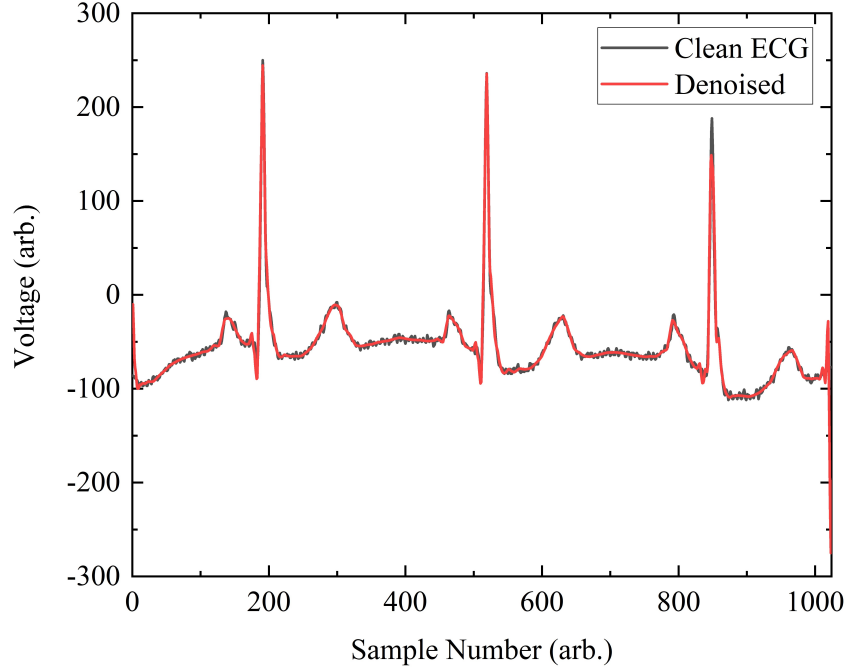


Figure 6.9: The original ECG signal with no noise is shown along with the denoised signal after the 50 Hz noise was removed (the magnitude of 50 Hz noise was 400).

6.3.3 Allan Variance

The non-overlapping Allan variance of a signal in the time domain is a useful measure of which differing noise sources dominate the performance of signal averaging over a given averaging time, τ . The Allan variance is given by

$$\sigma_x^2(\tau) = \frac{1}{2} \langle (x_{n+1} - x_n)^2 \rangle, \quad (6.1)$$

where x_{n+1} is the average value of a given cluster and x_n is the average of the preceding cluster. The Allan deviation, $\sigma_x(\tau)$, is defined as the square root of the Allan variance. The averaging time τ is varied from a single sample point up to half of the maximum time of the given time trace [165; 149]. The Allan deviation was computed for each magnetometer channel when on-resonance (magnetically sensitive) and off-resonance (magnetically insensitive) and the gradiometric output when on-resonance and is discussed in section 6.4.

6.3.4 Power Saturation

The laser power for these measurements were set at 500 mW, each sensor head had received half of this power. The full 6000 mW of was not used as the fan cooled heat

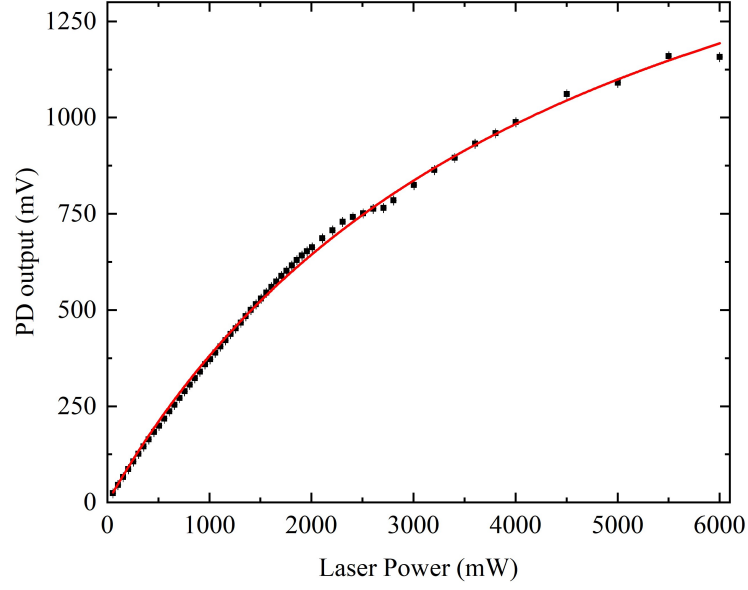


Figure 6.10: A power saturation curve of the gradiometer.

sink supplied by Laser Quantum was not sufficient in keeping the laser head cool. In addition, it was found that at full power the detectors of the balanced detectors would saturate well before the full power of the laser could be used, this would require the development of a custom balanced detector that could tolerate higher powers before reaching saturation. A power saturation measurement was taken see figure 6.10; as the photodiodes of the balanced detectors would saturate the power saturation measurements were taken using a biased photodiode (Thorlabs DET100A2), which was biased with a variable resistor set to 996Ω . For this measurement the 50:50 beam splitter was removed so the full power could be directed to a single sensor head, the diamond used for this measurement was the same as the diamond used for the results in section 4.1; the reason for this was the diamond used in the majority of the work in this chapter had just been cut into nine pieces and was in the process of being characterized. The data in figure 6.10 was fit according to equation 2.26, it was determined that P_{sat} is (4500 ± 100) mW and F_{∞} is (2080 ± 30) mV.

6.4 Results of Red-Red subtraction

The results of the subtraction are shown in figure 6.11a), the signal from each sensor head is shown and the results of subtracting the signals from the two. There is a clear reduction in the 50 Hz signal as shown by the reduction in the magnitude of the peak-to-peak. The sensitivity of each sensor head when only that sensor head

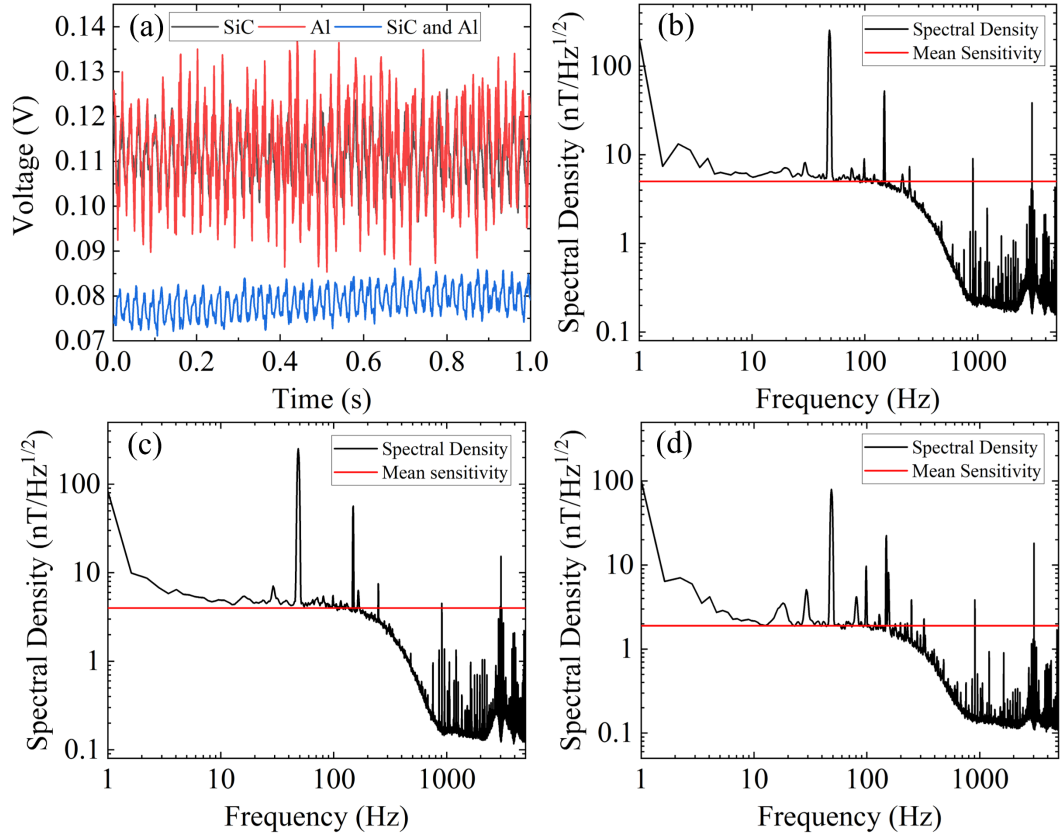


Figure 6.11: Data relating to the gradiometer sensitivity. (a) Voltage trace of the two sensor heads and the result of subtracting the two from one another. (b) The spectral density and sensitivity of the SiC sensor head. (c) The spectral density and sensitivity of the aluminum sensor head. (d) The spectral density and sensitivity when employing gradiometer subtraction, both sensor heads are magnetically sensitive. The bias magnetic was unaligned to any particular orientation for the results obtained.

is magnetically sensitive, for figure 6.11b) the SiC antenna was on-resonance while the Al sensor was off-resonance, the sensitivity of the magnetometer in this case was $(5 \pm 1) \text{ nT}/\sqrt{\text{Hz}}$. While for figure 6.11c) the SiC sensor head was off-resonance while the Al sensor head was on resonance, the sensitivity of the Al sensor head magnetometer was $(4 \pm 1) \text{ nT}/\sqrt{\text{Hz}}$. When both sensor heads are magnetically sensitive and the voltage signal of the Al sensor head is subtracted from that of the SiC sensor head the sensitivity of the gradiometer is $(1.9 \pm 0.6) \text{ nT}/\sqrt{\text{Hz}}$, see figure 6.11d). The magnitude of the 50 Hz mains signal for the SiC is 255 nT while for the Al the magnitude is 252 nT. For the subtracted signal the magnitude is 80 nT. Though there is a clear improvement in the sensitivity when employing gradiometric subtraction and there is a reduction in the 50 Hz mains noise it is possible that the cancellation of the 50 Hz is sub-optimal. It is believed that there are two possible causes that could explain this. The first is a possible phase shift in the π -phase, this may affect the subtraction of the two signals by the balanced detector. The other possible reason is the position of the sensor heads, the distance may be too far apart and thus there is a slight difference in the noise signals seen by each sensor head i.e. they may be too far apart so the noise they see is not as well correlated in time.

To determine which noise sources dominate over which averaging time an Allan deviation measurement was performed for the gradiometer: for each sensor head whilst one was magnetically sensitive whilst the other was magnetically insensitive and in subtraction mode when both sensor heads are magnetically sensitive, this data is shown in figure 6.12. The SiC antenna appears to offer a superior performance with the values of the Allan deviation over the majority of the time scales being lower than the aluminum antenna, it is believed that this is due to the superior thermal capability which reduces the drift due to temperature. If both sensor heads could use a SiC antenna it may be possible to improve the capabilities of the gradiometer. In addition as averaging over a long time scale is likely to be used to detect an MCG signal if thermal drift can be reduced it should be possible to obtain a higher quality MCG signal. The reasons for the initial increase in the value of the Allan deviation at low averaging times is unknown but this behavior is reproducible. The rest of the behavior is expected as the Allan deviation improves with the averaging time until averaging no longer helps and noise dominates.

6.5 Future Work

In this work a gradiometer has been developed. The system is still a work in progress with several advances needed before it is expected to be able to observe an unshielded

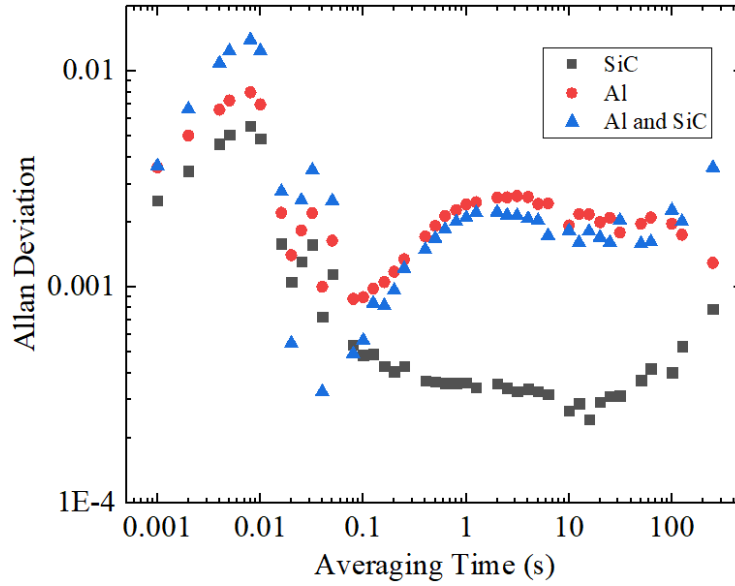


Figure 6.12: The Allan deviation for the gradiometer when either the SiC or aluminum sensor head is magnetically sensitive whilst the other is not and the other case is when subtraction mode is used whilst both magnetometer sensor heads are magnetically sensitive.

magnetic signal from the heart. A newer balanced detector is needed which can tolerate higher incident powers. In addition, the spacing of the current balanced detector is 20 mm and thus it was not possible to fully focus the entire photoluminescence from the aluminum sensor when employing a red-red subtraction scheme and thus a neutral density filter was needed to reduce the fluorescence on the SiC antenna signal to match the two signals. This reduction in fluorescence was over a factor of three, which provided a significant limitation to the system. The planned custom balanced detector will have the photodiode spacing set at 50 mm and so this issue can entirely be avoided. In addition, the photodiodes used will have a larger tolerance and thus will saturate at higher optical powers, several mW. This would allow one to make full use of the 6000 mW power output of the laser, currently only a twelfth of the total power is being used. Furthermore, the same bias magnetic field was used for both sensor heads and the magnet was unaligned to any orientation. If the magnet could be aligned to a (100) orientation the sensitivity would be improved. Another issue with the system was the heat sink used to cool the laser was not sufficient in keeping the laser cool enough, this was another reason that the laser could not operate at its full power. In addition, other gradiometer configurations will be explored to quantify which noise sources are most problematic. Currently the gradiometer subtracts one NV center ensemble fluorescence signal from another while both are

magnetically sensitive. However, it may be the case that having a setup where a portion of the laser is picked off and subtracted from the NV fluorescence for each sensor head could be superior. The output of the balanced detector in this case would be two magnetically sensitive signals that would be subtracted digitally. This system was setup but it was not possible to obtain data from it.

The signal processing techniques employed will certainly be useful however, it has not been possible to use them on any MCG data due to the current sensitivity of the gradiometer. It is expected that some of these techniques may need to be modified depending on the results obtained from the gradiometer.

Chapter 7

Conclusions

In this thesis the work undertaken was the advancement of the capabilities and sensitivity of a fiber-coupled diamond magnetometer. In Chapter 3, the sensitivity of this magnetometer was enhanced to reach a sensitivity of $(120 \pm 20) \text{ pT}/\sqrt{\text{Hz}}$ from 10-200 Hz. At the time of publication the sensitivity was $(310 \pm 20) \text{ pT}/\sqrt{\text{Hz}}$ between a frequency of 10-150 Hz which was the highest sensitivity achieved for a fiber-coupled diamond magnetometer. The objective of developing this magnetometer was for it to be highly mobile, such that it could be moved out of the lab and brought to various locations. The sensor head is particularly mobile and the sensor volume can be 2 mm from the object under study. Coupled to the high mobility it was desired to have a sensitivity that is comparable to the sensitivities of those achieved by experiments that are confined to the lab. The rest of the equipment is a $0.44 \text{ m} \times 0.55 \text{ m} \times 0.6 \text{ m}$ box on wheels which has been successfully operated outside of the lab. Much of this volume is empty space and further miniaturization is achievable, though making the optics more compact will prove challenging. The sensitivity can still be improved through the usage of a gradiometer and an improvement in the light collection. The conversion of green to red photons is calculated to be $\sim 0.06\%$ whilst other publications have reached up to $\sim 8\%$, which assuming a photon-shot-noise limited scaling would result in a 12-fold improvement to the sensitivity. It was found that the sensitivity of the magnetometer appears to be limited to reaching $120 \text{ pT}/\sqrt{\text{Hz}}$ with any increase in the NV fluorescence not resulting in a proportional increase in the sensitivity. It is suspected that the reason for this is background magnetic noise which limits the sensitivity. A gradiometer may help overcome this.

Once the fiber-coupled diamond magnetometer had been developed the magnetometer was modified to be able to image damage in steel for industrial applica-

tions. A technique was developed to use the magnetic flux profile of nearby magnets to detect damage in a ferromagnetic material, in this case 316 stainless steel. It was possible to image damage and differentiate between the width and depth. COMSOL simulations were undertaken and were in agreement with the experimental results. Further improvements to the design of the sensor head should allow for a better sensitivity and a superior spatial resolution. The magnetometer was also used for detecting low frequency eddy currents (less than a 100 Hz) that were induced in the stainless steel sample. It was possible to detect damage in the material and it expected that the technique could be applied for analysis to any conductive material. The radiation-hard nature of the sensor head should be useful for operation in conditions where other magnetometers cannot operate.

In chapter 6 the groundwork for the development of a fiber-coupled diamond gradiometer has been described. The gradiometer was in the early stages of construction with several improvements needed however it was still able to reach a sensitivity of $(1.9 \pm 0.6) \text{ nT}/\sqrt{\text{Hz}}$ in the frequency range of 10-200 Hz. Conversely, for each individual sensor head the sensitivity was $(5 \pm 1) \text{ nT}/\sqrt{\text{Hz}}$ and $(4 \pm 1) \text{ nT}/\sqrt{\text{Hz}}$. There was also a clear reduction in the 50 Hz mains noise. There were several factors that limited the sensitivity, the commercial balanced detectors used for the experiments saturate at 1 mW of incident optical power and thus the laser could not operate at its full power. The sensitivity can be improved significantly if a custom balanced detector is used that would allow the system to operate at its full power. Another limiting factor is the heat sink provided by Laser Quantum was not able to allow the laser to operate in a thermally stable regime. It is expected that the gradiometer can be significantly improved to reach the sensitivity needed to perform unshielded MCG once these issues have been overcome. Further work to improve the gradiometer is currently ongoing but it is expected that seeing an MCG signal should be possible once further improvements to the system are completed.

Bibliography

- [1] M. N. Yoder. Diamond in the USA. *Diam. Relat. Mater.*, 2(2-4):59–64, 1993.
- [2] N. Savvides and T. J. Bell. Hardness and elastic modulus of diamond and diamond-like carbon films. *Thin Solid Films*, 228(1-2):289–292, 1993.
- [3] A. M. Schrand, H. Huang, C. Carlson, J. J. Schlager, E. Osawa, S. M. Hussain, and L. Dai. Are diamond nanoparticles cytotoxic? *J. Phys. Chem. B*, 111(1):2–7, 2007.
- [4] N. Mohan, C. S. Chen, H. H. Hsieh, Y. C. Wu, and H. C. Chang. In vivo imaging and toxicity assessments of fluorescent nanodiamonds in *Caenorhabditis elegans*. *Nano Lett.*, 10(9):3692–3699, 2010.
- [5] R. Kaur and I. Badea. Nanodiamonds as novel nanomaterials for biomedical applications: Drug delivery and imaging systems. *Int. J. Nanomedicine*, 8:203–220, 2013.
- [6] R. Schirhagl, K. Chang, M. Loretz, and C. L. Degen. Nitrogen-Vacancy Centers in Diamond: Nanoscale Sensors for Physics and Biology. *Annu. Rev. Phys. Chem.*, 65(1):83–105, 2014.
- [7] S. R. Hemelaar, P. De Boer, M. Chipaux, W. Zuidema, T. Hamoh, F. P. Martinez, A. Nagl, J. P. Hoogenboom, B. N. G. Giepmans, and R. Schirhagl. Nanodiamonds as multi-purpose labels for microscopy. *Sci. Rep.*, 7(1):720, 2017.
- [8] J. Neburkova, J. Vavra, and P. Cigler. Coating nanodiamonds with biocompatible shells for applications in biology and medicine. *Curr. Opin. Solid State Mater. Sci.*, 21(1):43–53, 2017.
- [9] G. A. Slack. Thermal conductivity of pure and impure silicon, silicon carbide, and diamond. *J. Appl. Phys.*, 35(12):3460–3466, 1964.

- [10] L. Wei, P. K. Kuo, R. L. Thomas, T. R. Anthony, and W. F. Banholzer. Thermal conductivity of isotopically modified single crystal diamond. *Phys. Rev. Lett.*, 70(24):3764–3767, 1993.
- [11] A. Ward, D. A. Broido, D. A. Stewart, and G. Deinzer. Ab initio theory of the lattice thermal conductivity in diamond. *Phys. Rev. B*, 80(12):125203, 2009.
- [12] C. H. Xu, C. Z. Wang, C. T. Chan, and K. M. Ho. Theory of the thermal expansion of Si and diamond. *Phys. Rev. B*, 43(6):5024–5027, 1991.
- [13] S. Stoupin and Y. V. Shvyd’Ko. Ultraprecise studies of the thermal expansion coefficient of diamond using backscattering x-ray diffraction. *Phys. Rev. B*, 83(10):104102, 2011.
- [14] K. H. Bennemann. Covalent bonding in diamond. *Phys. Rev.*, 139:A482–A488, 1965.
- [15] C. Raynaud, D. Tournier, H. Morel, and D. Planson. Comparison of high voltage and high temperature performances of wide bandgap semiconductors for vertical power devices. *Diam. Relat. Mater.*, 19(1):1–6, 2010.
- [16] J. V. Macpherson. A practical guide to using boron doped diamond in electrochemical research. *Phys. Chem. Chem. Phys.*, 17(5):2935–2949, 2015.
- [17] F. Bachmair. Diamond sensors for future high energy experiments. *Nuclear Instruments and Methods in Physics Research Section A: Accelerators, Spectrometers, Detectors and Associated Equipment*, 831:370 – 377, 2016. Proceedings of the 10th International “Hiroshima” Symposium on the Development and Application of Semiconductor Tracking Detectors.
- [18] J. A. Savage, C. J. H. Wort, Charles S. J. Pickles, R. S. Sussmann, C. G. Sweeney, M. R. McClymont, J. R. Brandon, C. N. Dodge, and A. C. Beale. Properties of freestanding CVD diamond optical components. *Wind. Dome Technol. Mater. V*, 3060:144–159, 1997.
- [19] E. Woerner, C. Wild, W. Mueller-Sebert, and P. Koidl. CVD-diamond optical lenses. *Diam. Relat. Mater.*, 10(3-7):557–560, 2001.
- [20] B. Chandran, M. H. Gordon, and W. F. Schmidt. Comparison of cvd diamond to other substrate materials for thermal management. In *InterSociety Conference on Thermal Phenomena in Electronic Systems, I-THERM V*, pages 226–232, 1996.

- [21] A Gruber, A. Dräbenstedt, C Tietz, L Fleury, J Wrachtrup, and C Von Borczyskowski. Scanning confocal optical microscopy and magnetic resonance on single defect centers. *Science*, 276(5321):2012–2014, 1997.
- [22] I. Aharonovich and E. Neu. Diamond nanophotonics. *Advanced Optical Materials*, 2(10):911–928, 2014.
- [23] M. W. Doherty, N. B. Manson, P. Delaney, F. Jelezko, J. Wrachtrup, and L. C. L. Hollenberg. The nitrogen-vacancy colour centre in diamond. *Phys. Rep.*, 528(1):1–45, 2013.
- [24] C. Hepp, T. Müller, V. Waselowski, J. N. Becker, B. Pingault, H. Sternschulte, D. Steinmüller-Nethl, A. Gali, J R. Maze, M. Atatüre, and C. Becher. Electronic structure of the silicon vacancy color center in diamond. *Phys. Rev. Lett.*, 112(3):036405, 2014.
- [25] A. Sipahigil, K. D. Jahnke, L. J. Rogers, T. Teraji, J. Isoya, A. S. Zibrov, F. Jelezko, and M. D. Lukin. Indistinguishable photons from separated silicon-vacancy centers in diamond. *Phys. Rev. Lett.*, 113(11):113602, 2014.
- [26] U. F. S. D’Haenens-Johansson, A. M. Edmonds, B. L. Green, M. E. Newton, G. Davies, P. M. Martineau, R. U. A. Khan, and D. J. Twitchen. Optical properties of the neutral silicon split-vacancy center in diamond. *Phys. Rev. B*, 84(24):245208, 2011.
- [27] B. L. Green, S. Mottishaw, B. G. Breeze, A. M. Edmonds, U. F. S. D’Haenens-Johansson, M. W. Doherty, S. D. Williams, D. J. Twitchen, and M. E. Newton. Neutral Silicon-Vacancy Center in Diamond: Spin Polarization and Lifetimes. *Phys. Rev. Lett.*, 119(9):096402, 2017.
- [28] B. C. Rose, D. Huang, Z. H. Zhang, P. Stevenson, A. M. Tyryshkin, S. Sangtawesin, S. Srinivasan, L. Loudin, M. L. Markham, A. M. Edmonds, D. J. Twitchen, S A. Lyon, and N. P. De Leon. Observation of an environmentally insensitive solid-state spin defect in diamond. *Science*, 361(6397):60–63, 2018.
- [29] B. L. Green, M. W. Doherty, E. Nako, N. B. Manson, U. F. S. D’Haenens-Johansson, S. D. Williams, D. J. Twitchen, and M. E. Newton. Electronic structure of the neutral silicon-vacancy center in diamond. *Phys. Rev. B*, 99(16):161112, 2019.

- [30] J. Lenz and A. S. Edelstein. Magnetic sensors and their applications. *IEEE Sens. J.*, 6(3):631–649, 2006.
- [31] G. Chatzidrosos, A. Wickenbrock, L. Bougas, N. Leefer, T. Wu, K. Jensen, Y. Dumeige, and D. Budker. Miniature Cavity-Enhanced Diamond Magnetometer. *Phys. Rev. Appl.*, 8(4):044019, 2017.
- [32] V. K. Shah and R. T. Wakai. A compact, high performance atomic magnetometer for biomedical applications. *Phys. Med. Biol.*, 58(22):8153–8161, 2013.
- [33] P. Ripka and M. Janošek. Advances in magnetic field sensors. In *IEEE Sens. J.*, volume 10, pages 1108–1116, 2010.
- [34] M. Burghoff, H. Schleyerbach, D. Drung, L. Trahms, and H. Koch. A vector magnetometer module for biomagnetic application. *IEEE Trans. Appl. Supercond.*, 9(2 PART 3):4069–4072, 1999.
- [35] J. E. Lenz. A Review of Magnetic Sensors. *Proceedings of the IEEE*, 78(6):973–989, 1990.
- [36] A. Edelstein. Advances in Magnetometry. *J. Phys. Condens. Matter*, 19(16):165217, 2007.
- [37] I. K. Kominis, T. W. Kornack, J. C. Allred, and M. V. Romalis. A subfemtotesla multichannel atomic magnetometer. *Nature*, 422(6932):596–599, 2003.
- [38] H. B. Dang, A. C. Maloof, and M. V. Romalis. Ultrahigh sensitivity magnetic field and magnetization measurements with an atomic magnetometer. *Applied Physics Letters*, 97(15):151110, 2010.
- [39] W. C. Griffith, S. Knappe, and J. Kitching. Femtotesla atomic magnetometry in a microfabricated vapor cell. *Opt. Express*, 18(26):27167, 2010.
- [40] B. Grotz, M. V. Hauf, M. Dankerl, B. Naydenov, S. Pezzagna, J. Meijer, F. Jelezko, J. Wrachtrup, M. Stutzmann, F. Reinhard, and J. A. Garrido. Charge state manipulation of qubits in diamond. *Nat. Commun.*, 3, 2012.
- [41] C. Schreyvogel, V. Polyakov, S. Burk, H. Fedder, A. Denisenko, F. F. de Oliveira, R. Wunderlich, J. Meijer, V. Zuerbig, J. Wrachtrup, and C. E. Nebel. Active and fast charge-state switching of single NV centres in diamond by in-plane Al-Schottky junctions. *Beilstein J. Nanotechnol.*, 7(1):1727–1735, 2016.

- [42] C. Schreyvogel, V. Polyakov, R. Wunderlich, J. Meijer, and C. E. Nebel. Active charge state control of single NV centres in diamond by in-plane Al-Schottky junctions. *Sci. Rep.*, 5:12160, 2015.
- [43] T. Gaebel, M. Domhan, C. Wittmann, I. Popa, F. Jelezko, J. Rabeau, A. Greentree, S. Prawer, E. Trajkov, P. R. Hemmer, and J. Wrachtrup. Photochromism in single nitrogen-vacancy defect in diamond. *Appl. Phys. B Lasers Opt.*, 82(2 SPEC. ISS.):243–246, 2006.
- [44] N. B. Manson and J. P. Harrison. Photo-ionization of the nitrogen-vacancy center in diamond. *Diam. Relat. Mater.*, 14(10):1705–1710, 2005.
- [45] G. Waldherr, J. Beck, M. Steiner, P. Neumann, A. Gali, T. H. Frauenheim, F. Jelezko, and J. Wrachtrup. Dark states of single nitrogen-vacancy centers in diamond unraveled by single shot NMR. *Phys. Rev. Lett.*, 106(15), 2011.
- [46] L. Rondin, J. P. Tetienne, T. Hingant, J. F. Roch, P. Maletinsky, and V. Jacques. Magnetometry with nitrogen-vacancy defects in diamond. *Rep. Prog. Phys.*, 77(5), 2014.
- [47] M. V. Gurudev Dutt, L. Childress, L. Jiang, E. Togan, J. Maze, F. Jelezko, A. S. Zibrov, P. R. Hemmer, and M. D. Lukin. Quantum register based on individual electronic and nuclear spin qubits in diamond. *Science*, 316(5829):1312–1316, 2007.
- [48] L. Jiang, J. S. Hodges, J. R. Maze, P. Maurer, J. M. Taylor, D. G. Cory, P. R. Hemmer, R. L. Walsworth, A. Yacoby, A. S. Zibrov, and M. D. Lukin. Repetitive readout of a single electronic spin via quantum logic with nuclear spin ancillae. *Science*, 326(5950):267–272, 2009.
- [49] J. R. Weber, W. F. Koehl, J. B. Varley, A. Janotti, B. B. Buckley, C. G. Van De Walle, and D. D. Awschalom. Quantum computing with defects. *Proc. Natl. Acad. Sci. U. S. A.*, 107(19):8513–8518, 2010.
- [50] L. Childress and R. Hanson. Diamond NV centers for quantum computing and quantum networks. *MRS Bull.*, 38(2):134–138, 2013.
- [51] S. Yang, Y. Wang, D. D. B. Rao, T. H. Tran, A. S. Momenzadeh, M. Markham, D. J. Twitchen, P. Wang, W. Yang, R. Stöhr, P. Neumann, H. Kosaka, and J. Wrachtrup. High-fidelity transfer and storage of photon states in a single nuclear spin. *Nat. Photonics*, 10(8):507–511, 2016.

- [52] C. Kurtsiefer, S. Mayer, P. Zarda, and H. Weinfurter. Stable solid-state source of single photons. *Phys. Rev. Lett.*, 85(2):290–293, 2000.
- [53] P. L. Stanwix, L. M. Pham, J. R. Maze, D. Le Sage, T. K. Yeung, P. Cappellaro, P. R. Hemmer, A. Yacoby, M. D. Lukin, and R. L. Walsworth. Coherence of nitrogen-vacancy electronic spin ensembles in diamond. *Phys. Rev. B - Condens. Matter Mater. Phys.*, 82(20):201201, 2010.
- [54] G. Balasubramanian, P. Neumann, D. Twitchen, M. Markham, R. Kolesov, N. Mizuochi, J. Isoya, J. Achard, J. Beck, J. Tissler, V. Jacques, P. R. Hemmer, F. Jelezko, and J. Wrachtrup. Ultralong spin coherence time in isotopically engineered diamond. *Nat. Mater.*, 8(5):383–387, 2009.
- [55] G. De Lange, Z. H. Wang, D. Ristè, V. V. Dobrovitski, and R. Hanson. Universal dynamical decoupling of a single solid-state spin from a spin bath. *Science*, 330(6000):60–63, 2010.
- [56] C. A. Ryan, J. S. Hodges, and D. G. Cory. Robust decoupling techniques to extend quantum coherence in diamond. *Phys. Rev. Lett.*, 105(20), 2010.
- [57] B. Naydenov, F. Dolde, L. T. Hall, C. Shin, H. Fedder, L. C. L. Hollenberg, F. Jelezko, and J. Wrachtrup. Dynamical decoupling of a single-electron spin at room temperature. *Phys. Rev. B - Condens. Matter Mater. Phys.*, 83(8):81201, 2011.
- [58] N. Zhao, S. W. Ho, and R. B. Liu. Decoherence and dynamical decoupling control of nitrogen vacancy center electron spins in nuclear spin baths. *Phys. Rev. B - Condens. Matter Mater. Phys.*, 85(11):115303, 2012.
- [59] N. Bar-Gill, L. M. Pham, A. Jarmola, D. Budker, and R. L. Walsworth. Solid-state electronic spin coherence time approaching one second. *Nat. Commun.*, 4, 2013.
- [60] H. Clevenson, L. M. Pham, C. Teale, K. Johnson, D. Englund, and D. Braje. Robust high-dynamic-range vector magnetometry with nitrogen-vacancy centers in diamond. *Appl. Phys. Lett.*, 112(25):252406, 2018.
- [61] D. M. Toyli, D. J. Christle, A. Alkauskas, B. B. Buckley, C. G. Van de Walle, and D. D. Awschalom. Measurement and control of single nitrogen-vacancy center spins above 600 K. *Phys. Rev. X*, 2(3):031001, 2012.
- [62] B. M. Chernobrod and G. P. Berman. Spin microscope based on optically detected magnetic resonance. *Journal of Applied Physics*, 97(1):014903, 2005.

- [63] C. L. Degen. Scanning magnetic field microscope with a diamond single-spin sensor. *Appl. Phys. Lett.*, 92(24):243111, 2008.
- [64] J. M. Taylor, P. Cappellaro, L. Childress, L. Jiang, D. Budker, P. R. Hemmer, A. Yacoby, R. Walsworth, and M. D. Lukin. High-sensitivity diamond magnetometer with nanoscale resolution. *Nat. Phys.*, 4(10):810–816, 2008.
- [65] G. Balasubramanian, I. Y. Chan, R. Kolesov, M. Al-Hmoud, J. Tisler, C. Shin, C. Kim, A. Wojcik, P. R. Hemmer, A. Krueger, T. Hanke, A. Leitenstorfer, R. Bratschitsch, F. Jelezko, and J. Wrachtrup. Nanoscale imaging magnetometry with diamond spins under ambient conditions. *Nature*, 455(7213):648–651, 2008.
- [66] J. R. Maze, P. L. Stanwix, J. S. Hodges, S. Hong, J. M. Taylor, P. Cappellaro, L. Jiang, M. V. Gurudev Dutt, E. Togan, A. S. Zibrov, A. Yacoby, R. L. Walsworth, and M. D. Lukin. Nanoscale magnetic sensing with an individual electronic spin in diamond. *Nature*, 455(7213):644–647, 2008.
- [67] V. M. Acosta, E. Bauch, M. P. Ledbetter, C. Santori, K.-M C. Fu, P. E. Barclay, R. G. Beausoleil, H. Linget, J. F. Roch, F. Treussart, S. Chemerisov, W. Gawlik, and D. Budker. Diamonds with a high density of nitrogen-vacancy centers for magnetometry applications. *Phys. Rev. B - Condens. Matter Mater. Phys.*, 80(11), 2009.
- [68] B. J. Maertz, A. P. Wijnheijmer, G. D. Fuchs, M. E. Nowakowski, and D. D. Awschalom. Vector magnetic field microscopy using nitrogen vacancy centers in diamond. *Appl. Phys. Lett.*, 96(9):92504, 2010.
- [69] L. T. Hall, J. H. Cole, C. D. Hill, and L. C. L. Hollenberg. Sensing of Fluctuating Nanoscale Magnetic Fields Using Nitrogen-Vacancy Centers in Diamond. *Phys. Rev. Lett.*, 103(22), 2009.
- [70] L. T. Hall, D. A. Simpson, and L. C. L. Hollenberg. Nanoscale sensing and imaging in biology using the nitrogen-vacancy center in diamond. *MRS Bull.*, 38(2):162–167, 2013.
- [71] G. Balasubramanian, A. Lazarev, S. R. Arumugam, and D.-W. Duan. Nitrogen-Vacancy color center in diamond-emerging nanoscale applications in bioimaging and biosensing. *Curr. Opin. Chem. Biol.*, 20(1):69–77, 2014.
- [72] N. Mohan, Y. K. Tzeng, L. Yang, Y. Y. Chen, Y. Y. Hui, C. Y. Fang, and H. C. Chang. Sub-20-nm fluorescent nanodiamonds as photostable biolabels

- and fluorescence resonance energy transfer donors. *Adv. Mater.*, 22(7):843–847, 2010.
- [73] X. Q. Zhang, R. Lam, X. Xu, E. K. Chow, H. J. Kim, and D. Ho. Multimodal nanodiamond drug delivery carriers for selective targeting, imaging, and enhanced chemotherapeutic efficacy. *Adv. Mater.*, 23(41):4770–4775, 2011.
- [74] S. J. Yu, M. W. Kang, H. C. Chang, K. M. Chen, and Y. C. Yu. Bright fluorescent nanodiamonds: No photobleaching and low cytotoxicity. *J. Am. Chem. Soc.*, 127(50):17604–17605, 2005.
- [75] C. C. Fu, H. Y. Lee, K. Chen, T. S. Lim, H. Y. Wu, P. K. Lin, P. K. Wei, P. H. Tsao, H. C. Chang, and W. Fann. Characterization and application of single fluorescent nanodiamonds as cellular biomarkers. *Proc. Natl. Acad. Sci. U. S. A.*, 104(3):727–732, 2007.
- [76] D. R. Glenn, R. R. Fu, P. Kehayias, D. Le Sage, E. A. Lima, B. P. Weiss, and R. L. Walsworth. Micrometer-scale magnetic imaging of geological samples using a quantum diamond microscope. *Geochemistry, Geophys. Geosystems*, 18(8):3254–3267, 2017.
- [77] H. J. Mamin, M. Kim, M. H. Sherwood, C. T. Rettner, K. Ohno, D. D. Awschalom, and D. Rugar. Nanoscale nuclear magnetic resonance with a nitrogen-vacancy spin sensor. *Science*, 339(6119):557–560, 2013.
- [78] J. M. Boss, K. S. Cujia, J. Zopes, and C. L. Degen. Quantum sensing with arbitrary frequency resolution. *Science*, 356(6340):837–840, 2017.
- [79] S. Schmitt, Tuvia Gefen, Felix M. Stürner, T. Uden, G. Wolff, C. Müller, J. Scheuer, B. Naydenov, M. Markham, S. Pezzagna, J. Meijer, I. Schwarz, M. Plenio, A. Retzker, L. P. McGuinness, and F. Jelezko. Submillihertz magnetic spectroscopy performed with a nanoscale quantum sensor. *Science*, 356(6340):832–837, 2017.
- [80] D. R. Glenn, D. B. Bucher, J. Lee, M. D. Lukin, H. Park, and R. L. Walsworth. High-resolution magnetic resonance spectroscopy using a Solid-State spin sensor. *Nature*, 555(7696):351–354, 2018.
- [81] J. F. Barry, M. J. Turner, J. M. Schloss, D. R. Glenn, Y. Song, M. D. Lukin, H. Park, and R. L. Walsworth. Optical magnetic detection of single-neuron action potentials using quantum defects in diamond. *Proceedings of the National Academy of Sciences*, 113(49):14133–14138, 2016.

- [82] G. Chatzidrosos, A. Wickenbrock, L. Bougas, H. Zheng, O. Tretiak, Y. Yang, and D. Budker. Eddy-Current Imaging with Nitrogen-Vacancy Centers in Diamond. *Phys. Rev. Appl.*, 11(1):14060, 2019.
- [83] B. Hensen, H. Bernien, A. E. Dréau, A. Reiserer, N. Kalb, M. S. Blok, J. Ruitenbergh, R. F. L. Vermeulen, R. N. Schouten, C. Abellán, W. Amaya, V. Pruneri, M. W. Mitchell, M. Markham, D. J. Twitchen, D. Elkouss, S. Wehner, T. H. Taminiau, and R. Hanson. Loophole-free Bell inequality violation using electron spins separated by 1.3 kilometres. *Nature*, 526(7575):682–686, 2015.
- [84] H. Koch. Squid magnetocardiography: status and perspectives. *IEEE Transactions on Applied Superconductivity*, 11(1):49–59, 2001.
- [85] M. Buchner, K. Höfler, B. Henne, V. Ney, and A. Ney. Spin microscope based on optically detected magnetic resonance. *Journal of Applied Physics*, 124(161101), 2018.
- [86] R. Fenici, D. Brisinda, J. Nenonen, and P. Fenici. Phantom validation of multichannel magnetocardiography source localization. *Pacing and Clinical Electrophysiology*, 26(1p2):426–430, 2003.
- [87] R. Fenici, D. Brisinda, and A. M. Meloni. Clinical application of magnetocardiography. *Expert Rev. Mol. Diagn.*, 5(3):291–313, 2005.
- [88] Y. Shi, C. Zhang, R. Li, M. Cai, and G. Jia. Theory and application of magnetic flux leakage pipeline detection. *Sensors*, 15(12):31036–31055, 2015.
- [89] H. U. Auster, K. H. Glassmeier, W. Magnes, O. Aydogar, W. Baumjohann, D. Constantinescu, D. Fischer, K. H. Fornacon, E. Georgescu, P. Harvey, O. Hillenmaier, R. Kroth, M. Ludlam, Y. Narita, R. Nakamura, K. Okrafka, F. Plaschke, I. Richter, H. Schwarzl, B. Stoll, A. Valavanoglou, and M. Wiedemann. The THEMIS Fluxgate Magnetometer. *Space Sci. Rev.*, 141(235–264), 2008.
- [90] E. Boto, N. Holmes, J. Leggett, G. Roberts, V. Shah, S. S. Meyer, L. D. Muñoz, K. J. Mullinger, T. M. Tierney, S. Bestmann, G. R. Barnes, R. Bowtell, and M. J. Brookes. Moving magnetoencephalography towards real-world applications with a wearable system. *Nature*, 555:657–661, 2018.
- [91] J. H. N. Loubser and J A Van Wyk. Electron spin resonance in the study of diamond. *Reports Prog. Phys.*, 41(8):1201–1248, 1978.

- [92] T. Fukui, Y. Doi, T. Miyazaki, Y. Miyamoto, H. Kato, T. Matsumoto, T. Makino, S. Yamasaki, R. Morimoto, N. Tokuda, M. Hatano, Y. Sakagawa, H. Morishita, T. Tashima, S. Miwa, Y. Suzuki, and N. Mizuochi. Perfect selective alignment of nitrogen-vacancy centers in diamond. *Appl. Phys. Express*, 7(5):055201, 2014.
- [93] T. Miyazaki, Y. Miyamoto, T. Makino, H. Kato, S. Yamasaki, T. Fukui, Y. Doi, N. Tokuda, M. Hatano, and N. Mizuochi. Atomistic mechanism of perfect alignment of nitrogen-vacancy centers in diamond. *Appl. Phys. Lett.*, 105(26):261601, 2014.
- [94] H. Ishiwata, M. Nakajima, K. Tahara, H. Ozawa, T. Iwasaki, and M. Hatano. Perfectly aligned shallow ensemble nitrogen-vacancy centers in (111) diamond. *Appl. Phys. Lett.*, 111(4):043103, 2017.
- [95] A. M. Edmonds, U. F. S. D’Haenens-Johansson, R. J. Cruddace, M. E. Newton, K.-M M.C. Fu, C. Santori, R. G. Beausoleil, D. J. Twitchen, and M. L. Markham. Production of oriented nitrogen-vacancy color centers in synthetic diamond. *Phys. Rev. B - Condens. Matter Mater. Phys.*, 86(3):035201, 2012.
- [96] J. Michl, T. Teraji, S. Zaiser, I. Jakobi, G. Waldherr, F. Dolde, P. Neumann, M. W. Doherty, N. B. Manson, J. Isoya, and J. Wrachtrup. Perfect alignment and preferential orientation of nitrogen-vacancy centers during chemical vapor deposition diamond growth on (111) surfaces. *Appl. Phys. Lett.*, 104(10):102407, 2014.
- [97] M. Lesik, J. P. Tetienne, A. Tallaire, J. Achard, V. Mille, A. Gicquel, J. F. Roch, and V. Jacques. Perfect preferential orientation of nitrogen-vacancy defects in a synthetic diamond sample. *Appl. Phys. Lett.*, 104(11):113107, 2014.
- [98] L. M. Pham, N. Bar-Gill, D. Le Sage, C. Belthangady, A. Stacey, M. Markham, D. J. Twitchen, M. D. Lukin, and R. L. Walsworth. Enhanced metrology using preferential orientation of nitrogen-vacancy centers in diamond. *Phys. Rev. B - Condens. Matter Mater. Phys.*, 86(12):121202, 2012.
- [99] K. Tahara, H. Ozawa, T. Iwasaki, N. Mizuochi, and M. Hatano. Quantifying selective alignment of ensemble nitrogen-vacancy centers in (111) diamond. *Appl. Phys. Lett.*, 107(19):193110, 2015.

- [100] T. P. M. Alegre, C. Santori, G. Medeiros-Ribeiro, and R. G. Beusoleil. Polarization-selective excitation of nitrogen vacancy centers in diamond. *Phys. Rev. B - Condens. Matter Mater. Phys.*, 76(16), 2007.
- [101] S. Steinert, F. Dolde, P. Neumann, A. Aird, B. Naydenov, G. Balasubramanian, F. Jelezko, and J. Wrachtrup. High sensitivity magnetic imaging using an array of spins in diamond. *Rev. Sci. Instrum.*, 81(4):043705, 2010.
- [102] L. M. Pham, D. Le Sage, P. L. Stanwix, T. K. Yeung, D. Glenn, A. Trifonov, P. Cappellaro, P. R. Hemmer, M. D. Lukin, H. Park, A. Yacoby, and R. L. Walsworth. Magnetic field imaging with nitrogen-vacancy ensembles. *New J. Phys.*, 13(13pp):45021, 2011.
- [103] J. M. Schloss, J. F. Barry, M. J. Turner, and R. L. Walsworth. Simultaneous Broadband Vector Magnetometry Using Solid-State Spins. *Phys. Rev. Appl.*, 10(3):34044, 2018.
- [104] D. Rohner, J. Happacher, P. Reiser, M. A. Tschudin, A. Tallaire, J. Achard, B. J. Shields, and P. Maletinsky. (111)-oriented, single crystal diamond tips for nanoscale scanning probe imaging of out-of-plane magnetic fields. *Appl. Phys. Lett.*, 115(19):192401, 2019.
- [105] M. L. Goldman, A. Sipahigil, M. W. Doherty, N. Y. Yao, S. D. Bennett, M. Markham, D. J. Twitchen, N. B. Manson, A. Kubanek, and M. D. Lukin. Phonon-induced population dynamics and intersystem crossing in nitrogen-vacancy centers. *Phys. Rev. Lett.*, 114(14), 2015.
- [106] N. Aslam, G. Waldherr, P. Neumann, F. Jelezko, and J. Wrachtrup. Photo-induced ionization dynamics of the nitrogen vacancy defect in diamond investigated by single-shot charge state detection. *New J. Phys.*, 15(1):013064, 2013.
- [107] L. Robledo, H. Bernien, T. V. D. Sar, and R. Hanson. Spin dynamics in the optical cycle of single nitrogen-vacancy centres in diamond. *New J. Phys.*, 13:025013, 2011.
- [108] J. R. Rabeau, P. Reichart, G. Tamanyan, D. N. Jamieson, S. Prawer, F. Jelezko, T. Gaebel, I. Popa, M. Domhan, and J. Wrachtrup. Implantation of labelled single nitrogen vacancy centers in diamond using ^{15}N . *Appl. Phys. Lett.*, 88(2):1–3, 2006.

- [109] D. Rugar, H. J. Mamin, M. H. Sherwood, M. Kim, C. T. Rettner, K. Ohno, and D. D. Awschalom. Proton magnetic resonance imaging using a nitrogen-vacancy spin sensor. *Nat. Nanotechnol.*, 10(2):120–124, 2015.
- [110] A. Gali, T. Simon, and J. E. Lowther. Anab initiostudy of local vibration modes of the nitrogen-vacancy center in diamond. *New Journal of Physics*, 13(2):025016, 2011.
- [111] V. M. Acosta, E. Bauch, A. Jarmola, L. J. Zipp, M. P. Ledbetter, and D. Budker. Broadband magnetometry by infrared-absorption detection of nitrogen-vacancy ensembles in diamond. *Appl. Phys. Lett.*, 97(17):174104, 2010.
- [112] K. Jensen, N. Leefer, A. Jarmola, Y. Dumeige, V. M. Acosta, P. Kehayias, B. Patton, and D. Budker. Cavity-enhanced room-temperature magnetometry using absorption by nitrogen-vacancy centers in diamond. *Phys. Rev. Lett.*, 112(16), 2014.
- [113] Y. Dumeige, M. Chipaux, V. Jacques, F. Treussart, J. F. Roch, T. Debuisschert, V. M. Acosta, A. Jarmola, K. Jensen, P. Kehayias, and D. Budker. Magnetometry with nitrogen-vacancy ensembles in diamond based on infrared absorption in a doubly resonant optical cavity. *Phys. Rev. B - Condens. Matter Mater. Phys.*, 87(15):155202, 2013.
- [114] P. Kehayias, M. W. Doherty, D. English, R. Fischer, A. Jarmola, K. Jensen, N. Leefer, P. Hemmer, N. B. Manson, and D. Budker. Infrared absorption band and vibronic structure of the nitrogen-vacancy center in diamond. *Phys. Rev. B - Condens. Matter Mater. Phys.*, 88(16):165202, 2013.
- [115] V. M. Acosta, A. Jarmola, L. J. Zipp, M. P. Ledbetter, E. Bauch, and D. Budker. Broadband magnetometry by infrared-absorption detection of diamond NV centers and associated temperature dependence. *Adv. Photonics Quantum Comput. Mem. Commun. IV*, 7948:79480W, 2011.
- [116] V. M. Acosta, A. Jarmola, E. Bauch, and D. Budker. Optical properties of the nitrogen-vacancy singlet levels in diamond. *Phys. Rev. B - Condens. Matter Mater. Phys.*, 82(20), 2010.
- [117] J. Harrison, M. J. Sellars, and N. B. Manson. Measurement of the optically induced spin polarisation of N-V centres in diamond. *Diam. Relat. Mater.*, 15(4-8):586–588, 2006.

- [118] F. Jelezko, T. Gaebel, I. Popa, A. Gruber, and J. Wrachtrup. Observation of Coherent Oscillations in a Single Electron Spin. *Phys. Rev. Lett.*, 92(7):076401, 2004.
- [119] B. J. Shields, Q. P. Unterreithmeier, N. P. De Leon, H. Park, and M. D. Lukin. Efficient Readout of a Single Spin State in Diamond via Spin-to-Charge Conversion. *Phys. Rev. Lett.*, 114(13):136402, 2015.
- [120] A. Batalov, C. Zierl, T. Gaebel, P. Neumann, I. Y. Chan, G. Balasubramanian, P. R. Hemmer, F. Jelezko, and J. Wrachtrup. Temporal coherence of photons emitted by single nitrogen-vacancy defect centers in diamond using optical rabi-oscillations. *Phys. Rev. Lett.*, 100(7):077401, 2008.
- [121] A. Schweiger and G. Jeschke. *Principles of Pulse Electron Paramagnetic Resonance*. Oxford University Press, 2001.
- [122] J. A. Weil and J. R. Bolton. *Basic Principles of Paramagnetic Resonance*, chapter 1, pages 1–35. John Wiley & Sons, Ltd, 2007.
- [123] M. Mostafanejad. Basics of the spin Hamiltonian formalism. *Int. J. Quantum Chem.*, 114(22):1495–1512, 2014.
- [124] M. M. Roessler and E. Salvadori. Principles and applications of EPR spectroscopy in the chemical sciences. *Chem. Soc. Rev.*, 47(8):2534–2553, 2018.
- [125] D. Goldfarb and S. Stoll. *EPR Spectroscopy: Fundamentals and Methods*. eMagRes Books. Wiley, 2018.
- [126] G. D. Fuchs, V. V. Dobrovitski, R. Hanson, A. Batra, C. D. Weis, T. Schenkel, and D. D. Awschalom. Excited-state spectroscopy using single spin manipulation in diamond. *Phys. Rev. Lett.*, 101:117601, 2008.
- [127] P. Neumann, I. Jakobi, F. Dolde, C. Burk, R. Reuter, G. Waldherr, J. Honert, T. Wolf, A. Brunner, J. H. Shim, D. Suter, H. Sumiya, J. Isoya, and J. Wrachtrup. High-precision nanoscale temperature sensing using single defects in diamond. *Nano Lett.*, 13(6):2738–2742, 2013.
- [128] G. Kucsko, P. C. Maurer, N. Y. Yao, M. Kubo, H. J. Noh, P. K. Lo, H. Park, and M. D. Lukin. Nanometre-scale thermometry in a living cell. *Nature*, 500(7460):54–58, 2013.

- [129] V. M. Acosta, E. Bauch, M. P. Ledbetter, A. Waxman, L. S. Bouchard, and D. Budker. Temperature dependence of the nitrogen-vacancy magnetic resonance in diamond. *Phys. Rev. Lett.*, 104(7):070801, 2010.
- [130] M. W. Doherty, V. M. Acosta, A. Jarmola, M. S. J. Barson, N. B. Manson, D. Budker, and L. C. L. Hollenberg. Temperature shifts of the resonances of the NV-center in diamond. *Phys. Rev. B - Condens. Matter Mater. Phys.*, 90(4):041201, 2014.
- [131] K. Jensen, V. M. Acosta, A. Jarmola, and D. Budker. Light narrowing of magnetic resonances in ensembles of nitrogen-vacancy centers in diamond. *Phys. Rev. B - Condens. Matter Mater. Phys.*, 87(1):014115, 2013.
- [132] A. Dréau, M. Lesik, L. Rondin, P. Spinicelli, O. Arcizet, J. F. Roch, and V. Jacques. Avoiding power broadening in optically detected magnetic resonance of single NV defects for enhanced dc magnetic field sensitivity. *Phys. Rev. B - Condens. Matter Mater. Phys.*, 84(19):195204, 2011.
- [133] J. F. Barry, J. M. Schloss, E. Bauch, M. J. Turner, C. A. Hart, L. M. Pham, and R. L. Walsworth. Sensitivity optimization for nv-diamond magnetometry. *Rev. Mod. Phys.*, 92:015004, 2020.
- [134] D. Le Sage, L. M. Pham, N. Bar-Gill, C. Belthangady, M. D. Lukin, A. Yacoby, and R. L. Walsworth. Efficient photon detection from color centers in a diamond optical waveguide. *Phys. Rev. B - Condens. Matter Mater. Phys.*, 85(12), 2012.
- [135] J. P. Hadden, J. P. Harrison, A. C. Stanley-Clarke, L. Marseglia, Y. L. D. Ho, B. R. Patton, J. L. O'Brien, and J. G. Rarity. Strongly enhanced photon collection from diamond defect centers under microfabricated integrated solid immersion lenses. *Appl. Phys. Lett.*, 97(24):241901, 2010.
- [136] S. Castelletto, J. P. Harrison, L. Marseglia, A. C. Stanley-Clarke, B. C. Gibson, B. A. Fairchild, J. P. Hadden, Y. L.D. Ho, M. P. Hiscocks, K. Ganesan, S. T. Huntington, F. Ladouceur, A. D. Greentree, S. Prawer, J. L. O'Brien, and J. G. Rarity. Diamond-based structures to collect and guide light. *New J. Phys.*, 13(025020), 2011.
- [137] A. W. Schell, T. Neumer, Q. Shi, J. Kaschke, J. Fischer, M. Wegener, and O. Benson. Laser-written parabolic micro-antennas for efficient photon collection. *Appl. Phys. Lett.*, 105(23):231117, 2014.

- [138] L. Li, E. H. Chen, J. Zheng, S. L. Mouradian, F. Dolde, T. Schröder, S. Karaveli, M. L. Markham, D. J. Twitchen, and D. Englund. Efficient photon collection from a nitrogen vacancy center in a circular bullseye grating. *Nano Lett.*, 15(3):1493–1497, 2015.
- [139] N. H. Wan, B. J. Shields, D. Kim, S. Mouradian, B. Lienhard, M. Walsh, H. Bakhru, T. Schröder, and D. Englund. Efficient Extraction of Light from a Nitrogen-Vacancy Center in a Diamond Parabolic Reflector. *Nano Lett.*, 18(5):2787–2793, 2018.
- [140] Z. Ma, S. Zhang, Y. Fu, H. Yuan, Y. Shi, J. Gao, L. Qin, J. Tang, J. Liu, and Y. Li. Magnetometry for precision measurement using frequency-modulation microwave combined efficient photon-collection technique on an ensemble of nitrogen-vacancy centers in diamond. *Opt. Express*, 26(1):382, 2018.
- [141] S. Zhang, Z. Ma, L. Qin, Y. Fu, Y. Shi, J. Liu, and Y. J. Li. Fluorescence detection using optical waveguide collection device with high efficiency on assembly of nitrogen vacancy centers in diamond. *Appl. Phys. Express*, 11(1):013007, 2018.
- [142] D. Duan, V. K. Kavatamane, S. R. Arumugam, G. Rahane, Y. K. Tzeng, H. C. Chang, H. Sumiya, S. Onoda, J. Isoya, and G. Balasubramanian. Enhancing fluorescence excitation and collection from the nitrogen-vacancy center in diamond through a micro-concave mirror. *Appl. Phys. Lett.*, 113(4):41107, 2018.
- [143] D. Duan, G. X. Du, V. K. Kavatamane, S. Arumugam, Y.-K Tzeng, H.-C. Chang, and G. Balasubramanian. Efficient nitrogen-vacancy centers’ fluorescence excitation and collection from micrometer-sized diamond by a tapered optical fiber in endoscope-type configuration. *Opt. Express*, 27(5):6734, 2019.
- [144] Dwen Duan, Vinaya Kumar Kavatamane, Ranjini Arumugam, Yan-Kai Tzeng, Huan-Cheng Chang, and Gopalakrishnan Balasubramanian. Tapered ultra-high numerical aperture optical fiber tip for nitrogen vacancy ensembles based endoscope in a fluidic environment. *Appl. Phys. Lett.*, 116:113701, 2020.
- [145] L. Xu, H. Yuan, N. Zhang, J. Zhang, G. Bian, P. Fan, M. Li, C. Zhang, Y. Zhai, and J. Fang. High-efficiency fluorescence collection for NV - center ensembles in diamond. *Opt. Express*, 27(8):10787, 2019.
- [146] L. Qin, S. Fu, Y. and Zhang, J. Zhao, J. Gao, H. Yuan, Z. Ma, Y. Shi, and J. Liu. Near-field microwave radiation function on spin assembly of nitrogen

- vacancy centers in diamond with copper wire and ring microstrip antennas. *Jpn. J. Appl. Phys.*, 57(7), 2018.
- [147] Y. Chen, H. Guo, W. Li, D. Wu, Q. Zhu, B. Zhao, L. Wang, Y. Zhang, R. Zhao, W. Liu, F. Du, J. Tang, and J. Liu. Large-area, tridimensional uniform microwave antenna for quantum sensing based on nitrogen-vacancy centers in diamond. *Appl. Phys. Express*, 11(12):123001, 2018.
 - [148] E. R. Eisenach, J. F. Barry, L. M. Pham, R. G. Rojas, D. R. Englund, and D. A. Braje. Broadband loop gap resonator for nitrogen vacancy centers in diamond. *Rev. Sci. Instrum.*, 89(9):094705, 2018.
 - [149] S. Ahmadi, H. A. R. El-Ella, J. O. B. Hansen, A. Huck, and U. L. Andersen. Pump-Enhanced Continuous-Wave Magnetometry Using Nitrogen-Vacancy Ensembles. *Phys. Rev. Appl.*, 8(3):034001, 2017.
 - [150] E. Bauch, C. A. Hart, J. M. Schloss, M. J. Turner, J. F. Barry, P. Kehayias, S. Singh, and R. L. Walsworth. Ultralong Dephasing Times in Solid-State Spin Ensembles via Quantum Control. *Phys. Rev. X*, 8(3):031025, 2018.
 - [151] I. Fescenko, A. Jarmola, I. Savukov, P. Kehayias, J. Smits, J. Damron, N. Ristoff, N. Mosavian, and V. M. Acosta. Diamond magnetometer enhanced by ferrite flux concentrators. *Phys. Rev. Research*, 2:023394, 2020.
 - [152] Y. Fu, Z. Ma, J. Zhao, H. Yuan, S. Zhang, Y. Shi, X. Zhang, and J. Liu. Optimization of solid atomic magnetometer with frequency modulation method on ensembles of nitrogen vacancy color centers in diamond. *Laser Phys.*, 28(12), 2018.
 - [153] N. Mizuochi, P. Neumann, F. Rempp, J. Beck, V. Jacques, P. Siyushev, K. Nakamura, D. J. Twitchen, H. Watanabe, S. Yamasaki, F. Jelezko, and J. Wrachtrup. Coherence of single spins coupled to a nuclear spin bath of varying density. *Phys. Rev. B - Condens. Matter Mater. Phys.*, 80(4), 2009.
 - [154] J. A. van Wyk, E. C. Reynhardt, G. L. High, and I. Kiflawi. The dependences of ESR line widths and spin - spin relaxation times of single nitrogen defects on the concentration of nitrogen defects in diamond. *Journal of Physics D: Applied Physics*, 30(12):1790–1793, 1997.
 - [155] S. Felton, A. M. Edmonds, M. E. Newton, P. M. Martineau, D. Fisher, D. J. Twitchen, and J. M. Baker. Hyperfine interaction in the ground state of the

- negatively charged nitrogen vacancy center in diamond. *Phys. Rev. B - Condens. Matter Mater. Phys.*, 79(7):075203, 2009.
- [156] K. Fang, V. M. Acosta, C. Santori, Z. Huang, K. M. Itoh, H. Watanabe, S. Shikata, and R. G. Beusoleil. High-sensitivity magnetometry based on quantum beats in diamond nitrogen-vacancy centers. *Phys. Rev. Lett.*, 110(13):130802, 2013.
 - [157] H. J. Mamin, M. H. Sherwood, M. Kim, C. T. Rettner, K. Ohno, D. D. Awschalom, and D. Rugar. Multipulse double-quantum magnetometry with near-surface nitrogen-vacancy centers. *Phys. Rev. Lett.*, 113(3):030803, 2014.
 - [158] H. S. Knowles, D. M. Kara, and M. Atatüre. Observing bulk diamond spin coherence in high-purity nanodiamonds. *Nat. Mater.*, 13(1):21–25, 2014.
 - [159] T. L. Wee, Y. K. Tzeng, C. C. Han, H. C. Chang, W. Fann, J. H. Hsu, K. Ming Chen, and E. C. Yu. Two-photon excited fluorescence of nitrogen-vacancy centers in proton-irradiated type Ib diamond. *J. Phys. Chem. A*, 111(38):9379–9386, 2007.
 - [160] C. K. Lin, Y. H. Wang, H. C. Chang, M. Hayashi, and S. H. Lin. One- and two-photon absorption properties of diamond nitrogen-vacancy defect centers: A theoretical study. *J. Chem. Phys.*, 129(12):124714, 2008.
 - [161] T. Plakhotnik and H. Aman. NV-centers in nanodiamonds: How good they are. *Diam. Relat. Mater.*, 82:87–95, 2018.
 - [162] B. Lü and B. Li. Study of the correspondence between flat-topped multi-Gaussian beams and super-Gaussian beams. *J. Opt. A Pure Appl. Opt.*, 4(5):509–513, 2002.
 - [163] T. Y. Cherezova, S. S. Chesnokov, L. N. Kaptsov, and A. V. Kudryashov. Super-Gaussian laser intensity output formation by means of adaptive optics. *Opt. Commun.*, 155(1-3):99–106, 1998.
 - [164] K. Bayat, J. Choy, M. Farrokh Baroughi, S. Meesala, and M. Loncar. Efficient, uniform, and large area microwave magnetic coupling to NV centers in diamond using double split-ring resonators. *Nano Lett.*, 14(3):1208–1213, 2014.
 - [165] T. Wolf, P. Neumann, K. Nakamura, H. Sumiya, T. Ohshima, J. Isoya, and J. Wrachtrup. Subpicotesla diamond magnetometry. *Phys. Rev. X*, 5(4):041001, 2015.

- [166] A. Tallaire, J. Achard, François Silva, O. Brinza, and A. Gicquel. Growth of large size diamond single crystals by plasma assisted chemical vapour deposition: Recent achievements and remaining challenges. *Comptes Rendus Phys.*, 14(2-3):169–184, 2013.
- [167] J. Achard, V. Jacques, and A. Tallaire. CVD diamond single crystals with NV centres: a review of material synthesis and technology for quantum sensing applications. *Journal of Physics D: Applied Physics*, 2020.
- [168] H. M. Strong and R. E. Hanneman. Crystallization of diamond and graphite. *The Journal of Chemical Physics*, 46(9):3668–3676, 1967.
- [169] C. S. Kennedy and G. C. Kennedy. The equilibrium boundary between graphite and diamond. *J. Geophys. Res.*, 81(14):2467–2470, 1976.
- [170] F. P. Bundy. Pressure-temperature phase diagram of elemental carbon. *Phys. A Stat. Mech. its Appl.*, 156(1):169–178, 1989.
- [171] F. P. Bundy, W. A. Bassett, M. S. Weathers, R. J. Hemley, H. K. Mao, and A. F. Goncharov. The pressure-temperature phase and transformation diagram for carbon; updated through 1994. *Carbon N. Y.*, 34(2):141–153, 1996.
- [172] X. Wang, S. Scandolo, and R. Car. Carbon phase diagram from ab initio molecular dynamics. *Phys. Rev. Lett.*, 95(18):185701, 2005.
- [173] Yuri N. Palyanov, Igor N. Kupriyanov, Alexander F. Khokhryakov, and Victor G. Ralchenko. 17 - crystal growth of diamond. In Peter Rudolph, editor, *Handbook of Crystal Growth (Second Edition)*, Handbook of Crystal Growth, pages 671 – 713. Elsevier, Boston, second edition edition, 2015.
- [174] K Nassau and J. Nassau. The history and present status of synthetic diamond. *J. Cryst. Growth*, 46(2):157–172, 1979.
- [175] H. M. Strong. Catalytic Effects in the Transformation of Graphite to Diamond. *J. Chem. Phys.*, 39(8):2057–2062, 1963.
- [176] R. S. Balmer, J. R. Brandon, S. L. Clewes, H. K. Dhillon, J. M. Dodson, I. Friel, P. N. Inglis, T. D. Madgwick, M. L. Markham, T. P. Mollart, N. Perkins, G. A. Scarsbrook, D. J. Twitchen, A. J. Whitehead, J. J. Wilman, and S. M. Woolard. Chemical vapour deposition synthetic diamond: Materials, technology and applications. *J. Phys. Condens. Matter*, 21(36):364221, 2009.

- [177] J. C. Angus. Diamond synthesis by chemical vapor deposition: The early years. *Diam. Relat. Mater.*, 49:77–86, 2014.
- [178] F. P. Bundy, H. T. Hall, H. M. Strong, and R. H. Wentorfjun. Man-Made Diamonds. *Nature*, 176(4471):51–55, 1955.
- [179] P. W. Bridgman. An Experimental Contribution to the Problem of Diamond Synthesis. *J. Chem. Phys.*, 15(2):92–98, 1947.
- [180] F. P. Bundy. Melting of graphite at very high pressure. *J. Chem. Phys.*, 38(3):618–630, 1963.
- [181] H. P. Bovenkerk, F. P. Bundy, H. T. Hall, H. M. Strong, and R. H. Wentorf. Preparation of Diamond. *Nature*, 184(4693):1094–1098, 1959.
- [182] H. T. Hall. Ultra-high-pressure, high-temperature apparatus: The "belt". *Rev. Sci. Instrum.*, 31(2):125–131, 1960.
- [183] F. P. Bundy. Direct conversion of graphite to diamond in static pressure apparatus. *Science*, 137(3535):1057–1058, 1962.
- [184] F. P. Bundy. Direct conversion of graphite to diamond in static pressure apparatus. *J. Chem. Phys.*, 38(3):631–643, 1963.
- [185] H. Kanda, M. Akaishi, and S. Yamaoka. New catalysts for diamond growth under high pressure and high temperature. *Appl. Phys. Lett.*, 65(6):784–786, 1994.
- [186] Y. N. Palyanov, Y. M. Borzdov, I. N. Kupriyanov, Y. V. Bataleva, and A. F. Khokhryakov. Diamond crystallization from a tin-carbon system at HPHT conditions. *Diam. Relat. Mater.*, 58:40–45, 2015.
- [187] Y. N. Palyanov, I. N. Kupriyanov, A. F. Khokhryakov, and Y. M. Borzdov. High-pressure crystallization and properties of diamond from magnesium-based catalysts. *CrystEngComm*, 19(31):4459–4475, 2017.
- [188] O. G. Epanchintsev, A. S. Zubchenko, A. E. Korneyev, and V. A. Simonov. Highly-efficient shock-wave diamond synthesis from fullerenes. *J. Phys. Chem. Solids*, 58(11):1785–1788, 1997.
- [189] R. H. Wentorf. Some studies of diamond growth rates. *J. Phys. Chem.*, 75(12):1833–1837, 1971.

- [190] H. Sumiya and S. Satoh. High-pressure synthesis of high-purity diamond crystal. *Diam. Relat. Mater.*, 5(11):1359–1365, 1996.
- [191] H. Sumiya, N. Toda, Y. Nishibayashi, and S. Satoh. Crystalline perfection of high purity synthetic diamond crystal. *J. Cryst. Growth*, 178(4):485–494, 1997.
- [192] H. Kanda, M. Akaishi, and S. Yamaoka. Synthesis of diamond with the highest nitrogen concentration. *Diam. Relat. Mater.*, 8(8-9):1441–1443, 1999.
- [193] Y. Zhang, C. Zang, H. Ma, Z. Liang, L. Zhou, S. Li, and X. Jia. HPHT synthesis of large single crystal diamond doped with high nitrogen concentration. *Diam. Relat. Mater.*, 17(2):209–211, 2008.
- [194] M. N. R. Ashfold, J. P. Goss, B. L. Green, P. W. May, M. E. Newton, and C. V. Peaker. Nitrogen in Diamond. *Chem. Rev.*, 2020.
- [195] X. Liu, X. Jia, C. Fang, and H. A. Ma. Diamond crystallization and growth in N-H enriched environment under HPHT conditions. *CrystEngComm*, 18(43):8506–8515, 2016.
- [196] S. S. Li, X. P. Jia, C. Y. Zang, Y. Tian, Y. F. Zhang, H. Y. Xiao, G. F. Huang, L. Q. Ma, Y. Li, X. L. Li, and H. A. Ma. Effects of Al and Ti/Cu on synthesis of type-IIa diamond crystals in Ni70Mn25Co5-C system at HPHT. *Chinese Phys. Lett.*, 25(10):3801–3804, 2008.
- [197] R. C. Burns, J. O. Hansen, R. A. Spits, M. Sibanda, C. M. Welbourn, and D. L. Welch. Growth of high purity large synthetic diamond crystals. *Diam. Relat. Mater.*, 8(8-9):1433–1437, 1999.
- [198] H. Sumiya, K. Harano, and K. Tamasaku. HPHT synthesis and crystalline quality of large high-quality (001) and (111) diamond crystals. *Diam. Relat. Mater.*, 58:221–225, 2015.
- [199] H. Zheng, J. Xu, G. Z. Iwata, T. Lenz, J. Michl, B. Yavkin, K. Nakamura, H. Sumiya, T. Ohshima, J. Isoya, J. Wrachtrup, A. Wickenbrock, and D. Budker. Zero-Field Magnetometry Based on Nitrogen-Vacancy Ensembles in Diamond. *Phys. Rev. Appl.*, 11(6):064068, 2019.
- [200] J. E. Butler, Y. A. Mankelevich, A. Cheesman, Jie Ma, and M. N. R. Ashfold. Understanding the chemical vapor deposition of diamond: Recent progress. *J. Phys. Condens. Matter*, 21(36):364201, 2009.

- [201] P. K. Bachmann, D. Leers, and H. Lydtin. Towards a general concept of diamond chemical vapour deposition. *Diam. Relat. Mater.*, 1(1):1–12, 1991.
- [202] M. Chandran, S. Michaelson, C. Saguy, and A. Hoffman. Fabrication of a nanometer thick nitrogen delta doped layer at the sub-surface region of (100) diamond. *Appl. Phys. Lett.*, 109(22):221602, 2016.
- [203] J. Achard, A. Tallaire, R. Sussmann, F. Silva, and A. Gicquel. The control of growth parameters in the synthesis of high-quality single crystalline diamond by CVD. *J. Cryst. Growth*, 284(3):396–405, 2005.
- [204] S. Nad, Y. Gu, and J. Asmussen. Determining the microwave coupling and operational efficiencies of a microwave plasma assisted chemical vapor deposition reactor under high pressure diamond synthesis operating conditions. *Rev. Sci. Instrum.*, 86(7):074701, 2015.
- [205] T. Teraji. High-quality and high-purity homoepitaxial diamond (100) film growth under high oxygen concentration condition. *J. Appl. Phys.*, 118(11):115304, 2015.
- [206] T. Teraji, T. Yamamoto, K. Watanabe, Y. Koide, J. Isoya, S. Onoda, T. Ohshima, L. J. Rogers, F. Jelezko, P. Neumann, J. Wrachtrup, and S. Koizumi. Homoepitaxial diamond film growth: High purity, high crystalline quality, isotopic enrichment, and single color center formation. *Phys. Status Solidi*, 212(11):2365–2384, 2015.
- [207] A. Argoitia, J. Angus, J. Ma, L. Wang, P. Pirouz, and W. R. L. Lambrecht. Heteroepitaxy of diamond on c-BN: Growth mechanisms and defect characterization. *J. Mater. Res.*, 9(7):1849–1865, 1994.
- [208] T. Suzuki and A. Argoitia. Current status of heteroepitaxy of CVD diamond. *Phys. Status Solidi*, 154(1):239–254, 1996.
- [209] M. Schreck, F. Hörmann, H. Roll, J. K. N. Lindner, and B. Stritzker. Diamond nucleation on iridium buffer layers and subsequent textured growth: A route for the realization of single-crystal diamond films. *Appl. Phys. Lett.*, 78(2):192–194, 2001.
- [210] M. J. Verstraete and J. C. Charlier. Why is iridium the best substrate for single crystal diamond growth? *Appl. Phys. Lett.*, 86(19):1917, 2005.

- [211] M. Fischer, S. Gsell, M. Schreck, R. Brescia, and B. Stritzker. Preparation of 4-inch Ir/YSZ/Si(001) substrates for the large-area deposition of single-crystal diamond. *Diam. Relat. Mater.*, 17(7-10):1035–1038, 2008.
- [212] O. A. Williams. Nanocrystalline diamond. *Diam. Relat. Mater.*, 20(5-6):621–640, 2011.
- [213] A. Chayahara, Y. Mokuno, Y. Horino, Y. Takasu, H. Kato, H. Yoshikawa, and N. Fujimori. The effect of nitrogen addition during high-rate homoepitaxial growth of diamond by microwave plasma CVD. *Diam. Relat. Mater.*, 13(11-12):1954–1958, 2004.
- [214] Y. C. Chen, P. S. Salter, S. Knauer, L. Weng, A. C. Frangeskou, C. J. Stephen, S. N. Ishmael, P. R. Dolan, S. Johnson, B. L. Green, G. W. Morley, M. E. Newton, J. G. Rarity, M. J. Booth, and J. M. Smith. Laser writing of coherent colour centres in diamond. *Nat. Photonics*, 11(2):77–80, 2017.
- [215] Y.-C. Chen, B. Griffiths, L. Weng, S. S. Nicley, S. N. Ishmael, Y. Lekhai, S. Johnson, C. J. Stephen, B. L. Green, G. W. Morley, M. E. Newton, M. J. Booth, P. S. Salter, and J. M. Smith. Laser writing of individual nitrogen-vacancy defects in diamond with near-unity yield. *Optica*, 6(5):662, 2019.
- [216] C. A. McLellan, B. A. Myers, S. Kraemer, K. Ohno, D. D. Awschalom, and A. C. Bleszynski Jayich. Patterned Formation of Highly Coherent Nitrogen-Vacancy Centers Using a Focused Electron Irradiation Technique. *Nano Lett.*, 16(4):2450–2454, 2016.
- [217] J. O. Orwa, C. Santori, K. M. C. Fu, B. Gibson, D. Simpson, I. Aharonovich, A. Stacey, A. Cimmino, P. Balog, M. Markham, D. Twitchen, A. D. Greentree, R. G. Beausoleil, and S. Prawer. Engineering of nitrogen-vacancy color centers in high purity diamond by ion implantation and annealing. *J. Appl. Phys.*, 109(8):083530, 2011.
- [218] J. Koike, D. M. Parkin, and T. E. Mitchell. Displacement threshold energy for type IIa diamond. *Appl. Phys. Lett.*, 60(12):1450–1452, 1992.
- [219] E. Kim, V. M. Acosta, E. Bauch, D. Budker, and P. R. Hemmer. Electron spin resonance shift and linewidth broadening of nitrogen-vacancy centers in diamond as a function of electron irradiation dose. *Appl. Phys. Lett.*, 101(8):082410, 2012.

- [220] S. Lawson, G. Davies, A. T. Collins, and A. Mainwood. Migration energy of the neutral vacancy in diamond. *J. Phys. Condens. Matter*, 4(9):L125—L131, 1992.
- [221] A. T. Collins and I. Kiflawi. The annealing of radiation damage in type Ia diamond. *Journal of Physics: Condensed Matter*, 21(36):364209, 2009.
- [222] P. Deák, B. Aradi, M. Kaviani, T. Frauenheim, and A. Gali. Formation of NV centers in diamond: A theoretical study based on calculated transitions and migration of nitrogen and vacancy related defects. *Phys. Rev. B*, 89(7):075203, 2014.
- [223] Y. Chu, N. P. De Leon, B. J. Shields, B. Hausmann, R. Evans, E. Togan, M. J. Burek, M. Markham, A. Stacey, A. S. Zibrov, A. Yacoby, D. J. Twitchen, M. Loncar, H. Park, P. Maletinsky, and M. D. Lukin. Coherent optical transitions in implanted nitrogen vacancy centers. *Nano Lett.*, 14(4):1982–1986, 2014.
- [224] M. Capelli, A.H. Heffernan, T. Ohshima, H. Abe, J. Jeske, A. Hope, A.D. Greentree, P. Reineck, and B.C. Gibson. Increased nitrogen-vacancy centre creation yield in diamond through electron beam irradiation at high temperature. *Carbon*, 143:714 – 719, 2019.
- [225] N. Fujimori, H. Nakahata, and T. Imai. Properties of Boron-Doped Epitaxial Diamond Films. *Japanese Journal of Applied Physics*, 29(Part 1, No. 5):824–827, 1990.
- [226] R. J. Zhang, S. T. Lee, and Y. W. Lam. Characterization of heavily boron-doped diamond films. *Diamond and Related Materials*, 5(11):1288 – 1294, 1996.
- [227] R. Robertson, J. J. Fox, and A. E. Martin. TWO TYPES OF DIAMOND. *Philosophical Transactions of the Royal Society of London*, 232:463–535, 1934.
- [228] R. Robertson, J. J. Fox, and A. E. Martin. Further Work on Two Types of Diamond. *Proceedings of the Royal Society of London. Series A, Mathematical and Physical Sciences*, 157(892):579–593, 1936.
- [229] J. M. King, T. M. Moses, J. E. Shigley, C. M. Welbourn, S. C. Lawson, and M. Cooper. Characterizing natural-color type IIb blue diamonds. *Gems and Gemology*, 34(4):246–268, 1998.

- [230] C. Breeding and J. Shigley. The "type" classification system of diamonds and its importance in gemology. *Gems and Gemology*, 45(2):96–111, 2009.
- [231] H. B. Dyer, F. A. Raal, L. Du Preez, and J. H. N. Loubser. Optical absorption features associated with paramagnetic nitrogen in diamond. *The Philosophical Magazine: A Journal of Theoretical Experimental and Applied Physics*, 11(112):763–774, 1965.
- [232] F. De Weerdts and J. Van Royen. Defects in coloured natural diamonds. *Diamond and Related Materials*, 10(3):474 – 479, 2001. 11th European Conference on Diamond, Diamond-like Materials, Carbon Nanotubes, Nitrides and Silicon Carbide.
- [233] J. Walker. Optical absorption and luminescence in diamond. *Reports on Progress in Physics*, 42(10):1605–1659, 1979.
- [234] M. Fox. *Optical properties of solids, 2nd Edition*. Oxford University Press Inc., 2007.
- [235] J. M. Hollas. *Modern Spectroscopy, 4th Edition*. John Wiley & Sons Ltd, 2004.
- [236] R. S. Krishnan. Raman Spectrum of Diamond. *Nature*, 155(3928):171, 1945.
- [237] N. Ferrer and J. M. Nogués-Carulla. Characterisation study of cut gem diamond by ir spectroscopy. *Diamond and Related Materials*, 5(6):598 – 602, 1996. Proceedings of the 6th European Conference on Diamond, Diamond-like and Related Materials Part 2.
- [238] P. Thongnopkun and S. Ekgsit. Ftir spectra of faceted diamonds and diamond simulants. *Diamond and Related Materials*, 14(10):1592 – 1599, 2005.
- [239] G. R. Eaton, S. S. Eaton, D. P. Barr, and T. R. Weber. *Quantitative EPR*. Springer-Verlag Wien, 2010.
- [240] X. Liu, J. Cui, F. Sun, X. Song, F. Feng, J. Wang, W. Zhu, L. Lou, and G. Wang. Fiber-integrated diamond-based magnetometer. *Appl. Phys. Lett.*, 103(14):143105, 2013.
- [241] I. V. Fedotov, L. V. Doronina-Amitonova, D. A. Sidorov-Biryukov, N. A. Safronov, A. O. Levchenko, S. A. Zibrov, S. M. Blakley, H. Perez, A. V. Akinov, A. B. Fedotov, P. Hemmer, K. Sakoda, V. L. Velichansky, M. O. Scully, and A. M. Zheltikov. Fiber-optic magnetometry with randomly oriented spins. *Opt. Lett.*, 39(23):6755, 2014.

- [242] D. Duan, G. X. Du, V. K. Kavatamane, S. Arumugam, Y.-K. Tzeng, H-C Chang, and G. Balasubramanian. Efficient nitrogen-vacancy centers' fluorescence excitation and collection from micrometer-sized diamond by a tapered optical fiber in endoscope-type configuration. *Opt. Express*, 27(5):6734–6745, 2019.
- [243] I. V. Fedotov, L. V. Doronina-Amitonova, D. A. Sidorov-Biryukov, N. A. Safronov, S. Blakley, A. O. Levchenko, S. A. Zibrov, A. B. Fedotov, S. Ya. Kilin, and M. O. Scully. Fiber-optic magnetic-field imaging. *Opt. Lett.*, 39(24):6954, 2014.
- [244] S. M. Blakley, I. V. Fedotov, L. V. Amitonova, E. E. Serebryannikov, H. Perez, S. Y. A. Kilin, and A. M. Zheltikov. Fiber-optic vectorial magnetic-field gradiometry by a spatiotemporal differential optical detection of magnetic resonance in nitrogen – vacancy centers in diamond. *Opt. Lett.*, 41(9):2057, 2016.
- [245] S. M. Blakley, I. V. Fedotov, S. Ya Kilin, and A. M. Zheltikov. Room-temperature magnetic gradiometry with fiber-coupled nitrogen-vacancy centers in diamond. *Opt. Lett.*, 40(16):3727, 2015.
- [246] F. M. Stürner, A. Brenneis, J. Kassel, U. Wostradowski, R. Rölver, T. Fuchs, K. Nakamura, H. Sumiya, S. Onoda, J. Isoya, and F. Jelezko. Compact integrated magnetometer based on nitrogen-vacancy centres in diamond. *Diam. Relat. Mater.*, 93:59 – 65, 2019.
- [247] A. K. Dmitriev and A. K. Vershovskii. Concept of a microscale vector magnetic field sensor based on nitrogen-vacancy centers in diamond. *J. Opt. Soc. Am. B*, 33(3):B1–B4, 2016.
- [248] A. Frangeskou, G. Morley, B. Green, B. Breeze, M. Dale, and R. Patel. Defect centre-based sensor, 2020. WO 2020/157497 A1.
- [249] F. M. Stürner, A. Brenneis, T. Buck, J. Kassel, R. Rölver, T. Fuchs, A. Savitsky, D. Suter, J. Grimm, S. Hengesbach, M. Förtsch, K. Nakamura, H. Sumiya, S. Onoda, J. Isoya, and F. Jelezko. Integrated and portable magnetometer based on nitrogen-vacancy ensembles in diamond. *Adv. Quantum Technol.*, 4(4):2000111, 2021.
- [250] S.-C. Zhang, H.-B. Lin, Y. Dong, B. Du, X.-D. Gao, C. Yu, Z.-H. Feng, X.-D. Chen, G.-C. Guo, and F.-W. Sun. A high-sensitivity fiber-coupled diamond magnetometer with surface coating. *arXiv preprint arXiv:2102.12233*, 2021.

- [251] H. A. R. El-Ella, S. Ahmadi, A. M. Wojciechowski, A. Huck, and U. L. Anderson. Optimised frequency modulation for continuous-wave optical magnetic resonance sensing using nitrogen-vacancy ensembles. *Opt. Express*, 25(13):14809, 2017.
- [252] R. S. Schoenfeld and W. Harneit. Real time magnetic field sensing and imaging using a single spin in diamond. *Phys. Rev. Lett.*, 106:030802, 2011.
- [253] K. Sternickel and A. I. Braginski. Biomagnetism using SQUIDs: status and perspectives. *Superconductor Science and Technology*, 19(3):S160–S171, 2006.
- [254] P. Cawley. Non-destructive testing - current capabilities and future directions. *Proc. Inst. Mech. Eng*, 215(4):213–223, 2001.
- [255] Z. D. Wang, Y. Gu, and Y. S. Wang. A review of three magnetic NDT technologies. *J. Magn. Magn. Mater*, 324(4):382 – 388, 2012.
- [256] S. Gholizadeh. A review of non-destructive testing methods of composite materials. *Procedia Structural Integrity*, 1:50 – 57, 2016.
- [257] M. Papaelias, C. Roberts, and C. L. Davis. A review on non-destructive evaluation of rails: State-of-the-art and future development. *Proc. Inst. Mech. Eng*, 222(4):367–384, 2008.
- [258] S. K. Dwivedi, M. Vishwakarma, and A. Soni. Advances and Researches on Non Destructive Testing: A Review. *Materials Today: Proceedings*, 5(2, Part 1):3690 – 3698, 2018. 7th International Conference of Materials Processing and Characterization, March 17-19, 2017.
- [259] D. C. Jiles. Review of magnetic methods for nondestructive evaluation. *NDT International*, 21(5):311 – 319, 1988.
- [260] D. C. Jiles. Review of magnetic methods for nondestructive evaluation (part 2). *NDT International*, 23(2):83 – 92, 1990.
- [261] C. Mandache and L. Clapham. A model for magnetic flux leakage signal predictions. *Journal of Physics D: Applied Physics*, 36(20):2427–2431, 2003.
- [262] M. Afzal and S. Udpa. Advanced signal processing of magnetic flux leakage data obtained from seamless gas pipeline. *NDT & E International*, 35(7):449 – 457, 2002.

- [263] K. S. Ryu, D. L. Atherton, and L. Clapham. Effect of pit geometry and bulk stress on near- and far-side calculated MFL signals*. *Journal of Physics D: Applied Physics*, 35(21):2693–2697, 2002.
- [264] Y. Li, J. Wilson, and G. Y. Tian. Experiment and simulation study of 3D magnetic field sensing for magnetic flux leakage defect characterisation. *NDT & E International*, 40(2):179 – 184, 2007.
- [265] H. Zuoying, Q. Peiwen, and C. Liang. 3D FEM analysis in magnetic flux leakage method. *NDT & E International*, 39(1):61 – 66, 2006.
- [266] Y. Lijian, L. Gang, Z. Guoguang, and G. Songwei. Sensor development and application on the oil-gas pipeline magnetic flux leakage detection. In *2009 9th International Conference on Electronic Measurement Instruments*, pages 2–876–2–878, 2009.
- [267] A. Joshi, L. Udpa, S. Udpa, and A. Tamburrino. Adaptive wavelets for characterizing magnetic flux leakage signals from pipeline inspection. *IEEE Transactions on Magnetics*, 42(10):3168–3170, 2006.
- [268] M. R. Kandroodi, F. Shirani, B. N. Araabi, M. N. Ahmadabadi, and M. M. Bassiri. Defect detection and width estimation in natural gas pipelines using MFL signals. In *2013 9th Asian Control Conference (ASCC)*, pages 1–6, 2013.
- [269] M. R. Kandroodi, B. N. Araabi, M. N. Ahmadabadi, F. Shirani, and M. M. Bassiri. Detection of natural gas pipeline defects using magnetic flux leakage measurements. In *2013 21st Iranian Conference on Electrical Engineering*, pages 1–6, 2013.
- [270] M. Rostami Kandroodi, B. Nadjar Araabi, M. Mansoob Bassiri, and M. Nili Ahmadabadi. Estimation of depth and length of defects from magnetic flux leakage measurements: Verification with simulations, experiments, and pigging data. *IEEE Transactions on Magnetics*, 53(3):1–10, 2017.
- [271] L. Kang, A. Feeney, and S. Dixon. The High Frequency Flexural Ultrasonic Transducer for Transmitting and Receiving Ultrasound in Air. *IEEE Sensors Journal*, 20(14):7653–7660, 2020.
- [272] G. Chatzidrosos, A. Wickenbrock, L. Bougas, H. Zheng, O. Tretiak, Y. Yang, and D. Budker. Eddy-current imaging with nitrogen-vacancy centers in diamond. *Phys. Rev. Applied*, 11:014060, 2019.

- [273] A. J. Petruska and J. J. Abbott. Optimal permanent-magnet geometries for dipole field approximation. *IEEE Transactions on Magnetics*, 49(2):811–819, 2013.
- [274] A. E. Moran, M. H. Forouzanfar, G. A. Roth, G. A. Mensah, M. Ezzati, C. J. L. Murray, and M. Naghavi. Temporal trends in ischemic heart disease mortality in 21 world regions, 1980 to 2010. *Circulation*, 129(14):1483–1492, 2014.
- [275] G. A. Roth, G. Nguyen, M. H. Forouzanfar, A. H. Mokdad, M. Naghavi, and C. J. L. Murray. Estimates of global and regional premature cardiovascular mortality in 2025. *Circulation*, 132(13):1270–1282, 2015.
- [276] S. Watanabe and S. Yamada. Magnetocardiography in early detection of electromagnetic abnormality in ischemic heart disease. *Journal of Arrhythmia*, 24(1):4–17, 2008.
- [277] A. J. Camm, R. Henderson, D. Brisinda, R. Body, R. G. Charles, B. Varcoe, and R. Fenici. Clinical utility of magnetocardiography in cardiology for the detection of myocardial ischemia. *Journal of Electrocardiology*, 57:10 – 17, 2019.
- [278] J. A. Finegold, P. Asaria, and D. P. Francis. Mortality from ischaemic heart disease by country, region, and age: Statistics from world health organisation and united nations. *International Journal of Cardiology*, 168(2):934 – 945, 2013.
- [279] M. Aoki, Y. Okamoto, T. Musha, and K. Harumi. Three-dimensional simulation of the ventricular depolarization and repolarization processes and body surface potentials: Normal heart and bundle branch block. *IEEE Transactions on Biomedical Engineering*, BME-34(6):454–462, 1987.
- [280] D. Pewsner, P. Jüni, M. Egger, M. Battaglia, J. Sundström, and L. M. Bachmann. Accuracy of electrocardiography in diagnosis of left ventricular hypertrophy in arterial hypertension: systematic review. *BMJ*, 335(7622):711, 2007.
- [281] F. E. Smith, P. Langley, P. V. Leeuwen, B. Hailer, L. Trahms, U. Steinhoff, J. P. Bourke, and A. Murray. Comparison of magnetocardiography and electrocardiography: a study of automatic measurement of dispersion of ventricular repolarization. *EP Europace*, 8(10):887–893, 2006.
- [282] H. K. Lim, H. Kwon, N. Chung, Y.-G. Ko, J.-M. Kim, I.-S. Kim, and Y.-K. Park. Usefulness of magnetocardiogram to detect unstable angina pectoris and

- non-st elevation myocardial infarction. *The American Journal of Cardiology*, 103(4):448 – 454, 2009.
- [283] M. W. Dale and G. W. Morley. Medical applications of diamond magnetometry: commercial viability, 2017.
- [284] R. Wyllie, M. Kauer, R. T. Wakai, and T. G. Walker. Optical magnetometer array for fetal magnetocardiography. *Optics letters*, 37(12):2247–2249, 2012.
- [285] J. W. Mooney, S. Ghasemi-Roudsari, E. Reade Banham, C. Symonds, N. Pawlowski, and B. T. H. Varcoe. A portable diagnostic device for cardiac magnetic field mapping. *Biomedical Physics & Engineering Express*, 3(1):015008, 2017.
- [286] C. Zhang, F. Shagieva, M. Widmann, M. Kübler, V. Vorobyov, P. Kapitanova, E. Nenasheva, R. Corkill, O. Rhrle, K. Nakamura, H. Sumiya, S. Onoda, J. Isoya, and J. Wrachtrup. Diamond Magnetometry and Gradiometry Towards Subpicotesla dc Field Measurement. *Physical Review Applied*, 15(6), 2021.
- [287] I. A. Sulai, Z. J. DeLand, M. D. Bulatowicz, C. P. Wahl, R. T. Wakai, and T. G. Walker. Characterizing atomic magnetic gradiometers for fetal magnetocardiography. *Review of Scientific Instruments*, 90(8):085003, 2019.
- [288] A. M. Edmonds, C. A. Hart, M. J. Turner, P.-O. Colard, J. M. Schloss, K. Olsson, R. Trubko, M. L. Markham, A. Rathmill, B. Horne-Smith, W. Lew, A. Manickam, S. Bruce, P. G. Kaup, J. C. Russo, M. J. DiMario, J. T. South, J. T. Hansen, D. J. Twitchen, and R. L. Walsworth. Generation of nitrogen-vacancy ensembles in diamond for quantum sensors: Optimization and scalability of CVD processes, 2020.
- [289] G. Baldazzi, G. Solinas, J. D. Valle, M. Barbaro, S. Micera, L. Raffo, and D. Pani. Systematic analysis of wavelet denoising methods for neural signal processing. *Journal of Neural Engineering*, 17(6):066016, 2020.
- [290] M. Srivastava, C. L. Anderson, and J. H. Freed. A new wavelet denoising method for selecting decomposition levels and noise thresholds. *IEEE Access*, 4:3862–3877, 2016.
- [291] P. S. Addison. Wavelet transforms and the ECG: a review. *Physiological Measurement*, 26(5):R155–R199, 2005.

- [292] H.-Y. Gao. Wavelet shrinkage denoising using the non-negative garrote. *Journal of Computational and Graphical Statistics*, 7(4):469–488, 1998.
- [293] F. Chang, W. Hong, T. Zhang, J. Jing, and X. Liu. Research on Wavelet Denoising for Pulse Signal Based on Improved Wavelet Thresholding. In *2010 First International Conference on Pervasive Computing, Signal Processing and Applications*, pages 564–567, 2010.
- [294] G. R. Lee, R. Gommers, F. Waselewski, K. Wohlfahrt, and A. O’Leary. Py-Wavelets: A Python package for wavelet analysis. *Journal of Open Source Software*, 4(36):1237, 2019.